8-2012

Semiconductor Nanocrystals: From Quantum Dots to Quantum Disks

Zheng Li
University of Arkansas, Fayetteville

SEMICONDUCTOR NANOCRYSTALS: FROM QUANTUM DOTS TO QUANTUM DISKS

SEMICONDUCTOR NANOCRYSTALS: FROM QUANTUM DOTS TO QUANTUM DISKS

A dissertation submitted in partial fulfillment
of the requirements for the degree of
Doctor of Philosophy in Chemistry

By

Zheng Li
Hunan University
Bachelor of Science in Chemistry, 2003
Fudan University
Master of Science in Inorganic Chemistry, 2007

August 2012
University of Arkansas

ABSTRACT

The bottom-up colloidal synthesis opened up the possibility of finely tuning and tailoring the semiconductor nanocrystals. Numerous recipes were developed for the preparation of colloidal semiconductor nanocrystals, especially the traditional quantum dots. However, due to the lack of thorough understanding to those systems, the synthesis chemistry is still on the empirical level. CdS quantum dots synthesis in non-coordinating solvent were taken as a model system to investigate its molecular mechanism and formation process, ODE was identified as the reducing agent for the preparation of CdS nanocrystals, non-injection and low-temperature synthesis methods developed. In this model system, we not only proved it's possible to systematically study the formation procedure of semiconductor nanocrystals, the insight learned during the research but also enhanced our understanding to this delicate system and promoted the development of synthetic chemistry. Although quantum dots could be routinely prepared in the lab with mature recipes, the colloidal semiconductor quantum well type materials are still hard to fathom. CdSe quantum disks structure was thoroughly analyzed with polar axes as the growth direction along the thickness direction, with both basal planes ended with Cd atom layer, which was coordinated with carboxylate ligands. Besides, four different thickness CdS quantum disks were prepared, its size-dependent lattice dilation, extremely sharp band-edge emission, and two-order of magnitude faster photoluminescence decay compared to quantum dots was investigated.

This dissertation is approved for
Recommendation to the
Graduate Council

Dissertation Director:

_____
Dr. Xiaogang Peng

Dissertation Committee:

_____
Dr. Bill Durham

_____
Dr. Z. Ryan Tian

_____
Dr. James F. Hinton

DISSERTATION DUPLICATION RELEASE

I hereby authorize the University of Arkansas Libraries to duplicate this dissertation when needed for research and/or scholarship.

Agreed _____
Zheng Li

Refused _____
Zheng Li

ACKNOWLEDGEMENTS

First, I would like to thank my family for the long-time, selfless support and encouragement throughout the tough and rough times. It would definitely unbelievable for me to go through such a long way without this, and I really appreciate the time and experience spent together with you guys.

Academically, I'd like to thank my Ph. D. advisor, Dr. Xiaogang Peng, from whom I learned that life is endless, and everyone should and could always excel than yesterday, this life attitude is really precious and rewarding to my future, not limited to the graduate school. Special thanks to Dr. James Hinton, your NMR course are really enlightening and knowledgeable, without your generous office hour, I don't think I could ever get it right for the quantitative NMR analysis. I'd like to thank Dr. Bill Durham for taking care of all kinds of businesses for me when Dr. Peng was absent during my senior years. Thanks also go to Dr. Ryan Tian and Dr. Peter Pulay for being so supportive during my whole graduate school, offering many opportunities for my Ph. D. training. I would like to take this opportunity to thank Dr. Gregory Salamo for supporting my final years during the graduate school, it was my honor to be able to collaborate with your group members and I got the opportunity to experience the different thinking logic between chemists and physicists. I'd like to thank Dr. Jingyi Chen for your kindness and support, it was really fun and easy-going to work together with you and your group members. Besides, I'd like to thank Dr. Colin Heyes for your help on the spectroscopic topics.

To the past and present Peng group members, I enjoyed working with every one of you. Special thanks to Renguo, Fei, Hank, Danny, Ross, it was interesting to work together with you guys in the lab and play cards during the weekends. I'd like to thank Jason, Susan, Grace,

Richard, and Mike for your help and answering many routine questions. You guys were always helpful and fun to be around.

Last but not least, every day I have is more than I deserved.

DEDICATION

"I have not yet lost a feeling of wonder, and of delight, that this delicate motion should reside in all the things around us, revealing itself only to him who looks for it. I remember, in the winter of our first experiments, just seven years ago, looking on snow with new eyes. There the snow lay around my doorstep - great heaps of protons quietly precessing in the earth's magnetic field. To see the world for a moment as something rich and strange is the private reward of many a discovery."

--Nobel lecture (11th December, 1952) Edward Mills Purcell

TABLE OF CONTENTS

ACKNOWLEDGEMENTS .....

DEDICATION .....

TABLE OF CONTENTS .....

LIST OF PUBLICATIONS .....

LIST OF ABBREVIATIONS .....

Chapter 1 Introduction 1

1.1 Historic moments and why nano? 1

1.2 Colloidal semiconductor nanocrystals 2

1.2.1 Boundary condition and quantum confinement 4

1.2.2 Optical characterization 9

1.3 Spectroscopic identification and common artifacts 16

1.3.1 Nuclear magnetic resonance (NMR) 17

1.3.2 Photoluminescence (PL) and Photoluminescence excitation (PLE) 19

1.3.3 Energy-dispersive X-ray spectroscopy (EDX) 20

1.4 Dissertation Objective and Overview 24

1.5 References 25

Chapter 2 Correlation of CdS Nanocrystal Formation with Elemental Sulfur Activation and Its Implication in Synthetic Development 34

2.1 Introduction 35

2.2 Experimental 37

2.3 Results and Discussions 43

2.4 Conclusions 67

2.5 References 68

Chapter 3 Size/Shape-Controlled Synthesis of Colloidal CdSe Quantum Disks: Ligand and Temperature Effects 74

3.1 Introduction 75

3.2 Experimental 78

3.3 Results and Discussions 81

3.4 Conclusions 107

3.5 References 109

Chapter 4 Thickness-Pure and Colloidal-Stable CdS Quantum Disks with Tunable Thickness: Synthesis and Properties 115

4.1 Introduction 115

4.2 Experimental 118

4.3 Results and Discussions 122

4.4 Conclusions 144

4.5 References 145

Chapter 5 Conclusion 151

Appendices 152

LIST OF PUBLICATIONS

Li, Z.; Ji, Y.; Xie, R.; Grisham, S. Y.; Peng, X. Correlation of CdS Nanocrystal Formation with Elemental Sulfur Activation and Its Implication in Synthetic Development. *Journal of the American Chemical Society* **2011**, *133*, 17248-17256.

Li, Z.; Peng, X. Size/Shape-Controlled Synthesis of Colloidal CdSe Quantum Disks: Ligand and Temperature Effects. *Journal of the American Chemical Society* **2011**, *133*, 6578-6586.

Li, Z.; Qin, H.; Guzun, D.; Benamara, M.; Salamo, G.; Peng, X. Uniform Thickness and Colloidal-Stable CdS Quantum Disks with Tunable Thickness: Synthesis and Properties. *Nano Research* **2012**, in press.

LIST OF ABBREVIATIONS

DFT	Density Functional Theory
STM	Scanning Tunnelling Microscope
IBM	International Business Machines Corporation
AFM	Atomic Force Microscopy
KPFM	Kelvin Probe Force Microscopy
LED	Light Emitting Diode
HOMO	Highest Occupied Molecular Orbital
LUMO	Lowest Unoccupied Molecular Orbital
VB	Valence Band
CB	Conduction Band
ev	electron volt
3d	three-dimensional
2d	two-dimensional
1d	one-dimensional
0d	zero-dimensional
PL	Photoluminescence
ns	nanosecond
ps	picosecond
QY	Quantum Yield
NMR	Nuclear Magnetic Resonance
PLE	Photoluminescence Excitation
EDX	Energy-Dispersive X-ray spectroscopy

XRF	X-Ray Fluorescence
ESEM	Environmental Scanning Electron Microscope
SEM	Scanning Electron Microscope
ODE	1-octadecene
UV-Vis	Ultraviolet-Visible
S	Sulfur
Se	Selenium
Te	Tellurium
Pb	Lead
Cd	Cadmium
TEM	Transmission Electron Microscopy
HRTEM	High-Resolution Transmission Electron Microscopy
FTIR	Fourier Transform Infrared Spectroscopy
GC-MS	Gas Chromatography-Mass Spectroscopy
Ac	Acetate
Bu	Butanoate
Oc	Octanoate
HMQC	Heteronuclear Multiple Quantum Correlation
EI-MS	Electron Ionization-Mass Spectrum
fwhm	full-width-at-half-maximum
TBP	Tri-n-butylphosphine
XRD	X-Ray powder Diffraction
XPS	X-ray Photoelectron Spectroscopy

$CdSt_2$	Cadmium Stearate
rpm	revolutions per minute
b. p.	boiling point
m. p.	melting point
mmol	milimole
TRPL	Time-Resolved Photoluminescence
FFT	Fast Fourier Transform
MBE	Molecular Beam Epitaxy
hh	heavy hole
lh	light hole
CdTe	Cadmium Telluride
CdSe	Cadmium Selenide
CdS	Cadmium Sulfide
CdO	Cadmium Oxide
ZnTe	Zinc Telluride
ZnSe	Zinc Selenide
ZnS	Zinc Sulfide
ZnO	Zinc Oxide
InSb	Indium Antimonide
H_2S	Hydrogen Sulfide
Ar	Argon
MeOH	Methanol
EtOH	Ethanol

$CHCl_3$	Chloroform
$CDCl_3$	Deuterated Chloroform
NOE	Nuclear Overhauser Effect
mL	milliliter
KBr	Potassium Bromide
KOH	Potassium Hydroxide
HCl	Hydrochloric Acid
$AgNO_3$	Silver Nitrate
Ag_2S	Silver Sulfide
µL	microliter
g	gram
l	liter
wt	weight
M	Molar
DI	De-Ionized
ppm	part per million
MHz	megahertz
JCPDS	Joint Committee on Powder Diffraction Standards
mm	millimeter
nm	nanometer

Chapter 1 Introduction

"There's Plenty of Room at the Bottom"

--Richard Feynman, Pasadena, 29 December 1959

1.1 Historic moments and why nano?

Richard Feynman envisioned the birth of the nanotechnology more than sixty years ago at the annual meeting of the American Physical Society. It was not until 1990, with the help of

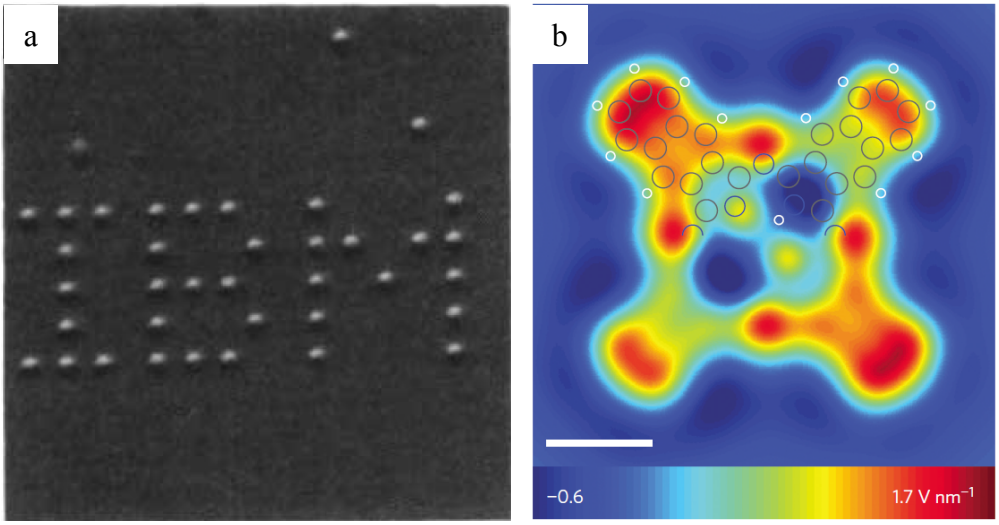

Figure 1-1. STM image of xenon atoms on nickel (110) surface, each letter is 5 nanometer (nm) from top to bottom (a); density functional theory (DFT)-calculated z-component of the electric field above a free naphthalocyanine molecule at a distance 0.3 nm from the molecular plane. Scale bars: 0.5 nm. The DFT-calculated atomic positions are overlaid in the upper halves of the image. Carbon, hydrogen and nitrogen atoms are grey, white and blue, respectively (b).

scanning tunnelling microscope (STM), as shown in Figure 1-1a, the IBM research scientists at

San Jose spelled the "IBM" with 35 xenon atoms on nickel surface, [1] demonstrating the possibility of manipulating atoms with atomic precision. [2, 3] Recently, with the combination of STM, atomic force microscopy (AFM), and kelvin probe force microscopy (KPFM), IBM Research scientists at Zurich imaged the charge distribution in a single molecule (Figure 1-1b), [4, 5] and opened up the possibility of observing the bonding formation/dissociation process, viz. the electron redistribution, which is the fundamental process during the chemical reactions.

The temptation of miniature down to the nanoscale originates from the fundamentally electronic, optical, magnetic property change compared with corresponding bulk materials, [6] which was due to the increase of surface area, and quantum confinement of electron, leading to potential application in catalysis, [7-9] drug delivery, [10-12] biological labeling, [13-17] solar cells, [18-20] light emitting diodes (LED), [21-24] etc. One of the most famous applications of nanotechnology lies at the advancement of integrated circuits. The prestigious Moore's Law predicted that "the number of transistors that can be placed inexpensively on an integrated circuit doubles approximately every two years." [25-27] It would be definitely hard to imagine this without the development on the nanotechnology.

1.2 Colloidal semiconductor nanocrystals

Similar to the highest occupied molecular orbital (HOMO) and lowest unoccupied molecular orbital (LUMO) frontier orbitals theory in the molecules, corresponding energy levels are called as valence band (VB) and conduction band (CB) in solid state physics. The energy difference between CB and VB are called as the bandgap. Generally, higher than 3.0 electron volt (ev) are considered as insulator, smaller than 0.5 ev are defined as metal, and bandgap between 0.5 and

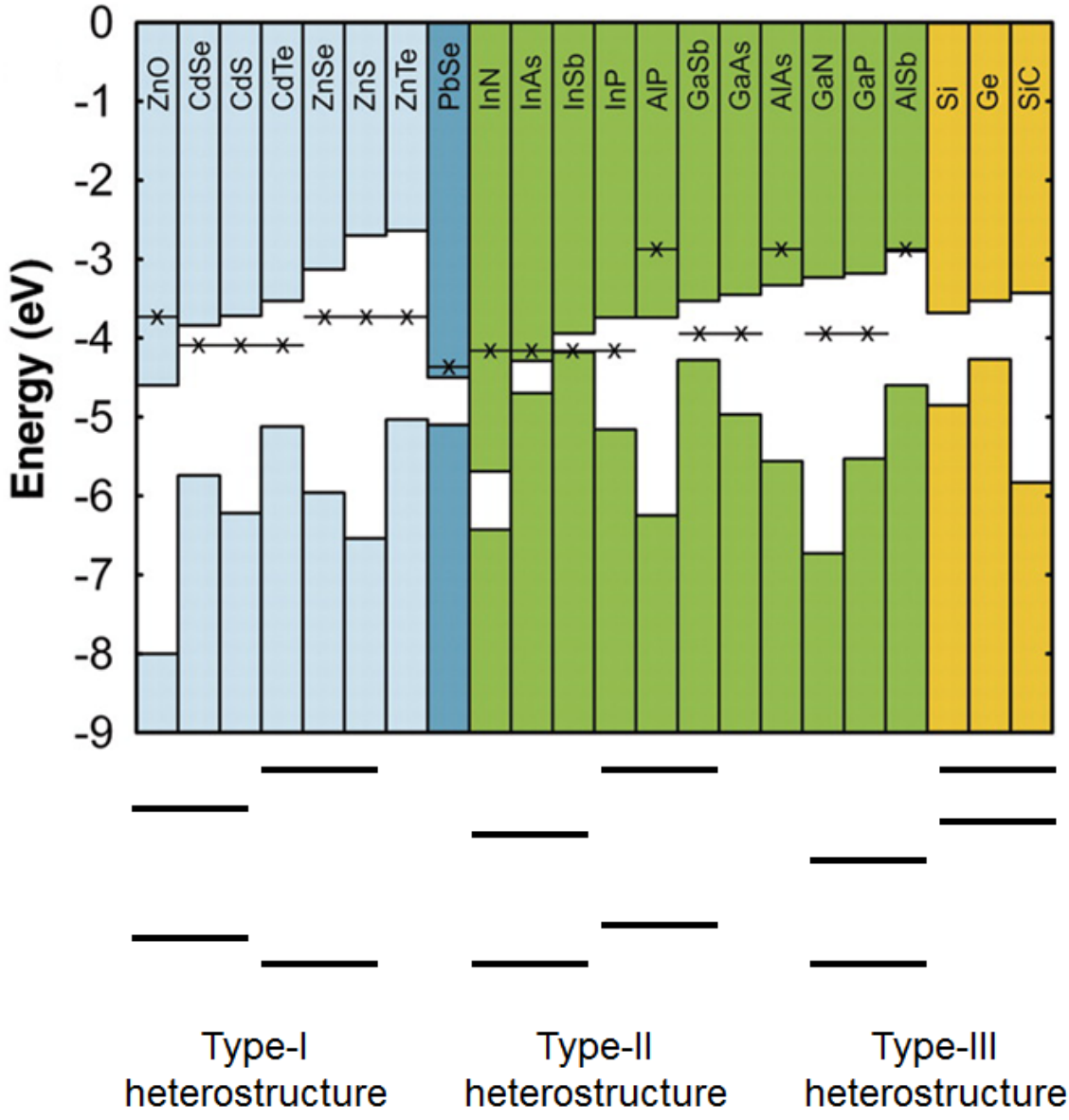

Figure 1-2. Top: The energy of semiconductor electronic band edges relative to the vacuum level. The space between the bars represents the band gap between valence and conduction bands. Reduction potentials of most cations are marked with ×'s. From left to right, semiconductor groups are II-VI (pale blue), IV-VI (blue), III-V (green), and IV (gold). Bottom: Three type of semiconductor heterostructures band-edge alignment.

3.0 ev are sorted into semiconductor. For the electron transition from VB edge to CB edge, there are two basic requirements: energy and momentum conservation. If the electron at the maximum

energy of VB has the same crystal momentum as the hole at the minimum energy of CB, the electron could be excited directly by photon, and corresponding semiconductor are called as direct semiconductor; if the electron at the maximum energy of VB has a different crystal momentum as the hole at the minimum energy of CB, the electron could only be excited indirectly by the photon, the assistance of phonon would be required, and corresponding semiconductor are called as indirect semiconductor. Common II-VI and III-V semiconductor such as cadmium/zinc chalcogenide, indium phosphide/arsenide are direct semiconductors; diamond, silicon, germanium, silicon carbide, boron nitride, and gallium phosphide are indirect semiconductors. [28]

Combining two different semiconductor materials could engineer the band-edge offset, making semiconductor heterostructures with novel properties not accessible from either of the components. [29] As shown in Figure 1-2 are the band edge positions of some common semiconductor materials, [30, 31] depending upon the band edge alignment, if the VB and CB of one component are enclosed in another component's VB and CB, such as CdSe and ZnS, this is the straddling type-I heterostructure; for the components with staggered VB and CB band-edge offset, such as CdSe and ZnTe, this is the type-II heterostructure; and if one component's VB minimum is higher than the CB maximum of another component, such as InSb and ZnO, this is the broken type-III heterostructure. In the following chapter, more discussions are concentrated on the effect of decreasing semiconductor size from bulk to nanometer scale.

1.2.1 Boundary condition and quantum confinement

Colloidal semiconductor nanocrystals are nanometer sized fragments of corresponding bulk crystals synthesized in solution. It lies between the discrete molecular component and corresponding bulk materials, also called as "artificial atoms". [32-37] The property change from bulk to nanometer size for semiconductor originates from two sides, the increase of surface atom ratio, [38] and the quantum confinement felt by the electrons. [39]

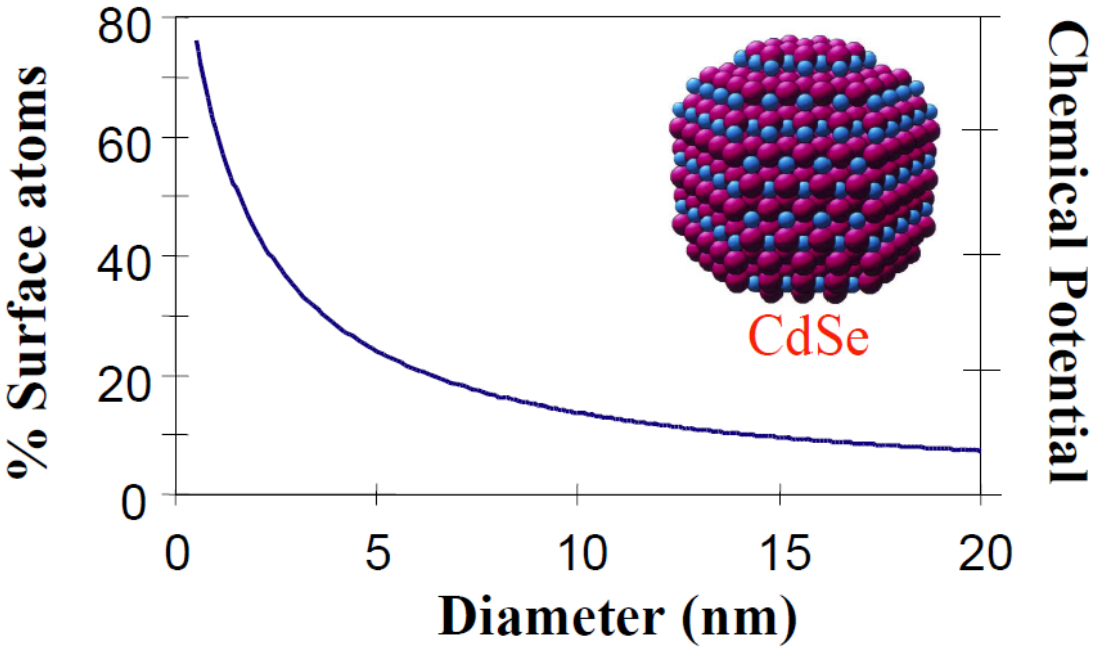

Figure 1-3. Size-dependence of the surface atom ratio and the relative chemical potential of CdSe nanocrystals, assuming a spherical shape.

Taken CdSe nanocrystals as an example, and assuming a spherical shape, simple model calculation in Figure 1-3 shows that the decrease of nanocrystals size leads to fast increase of surface atom ratio, and the increase of relative chemical potential. [38] This indicate that we should treat semiconductor nanocrystals distinctly from corresponding bulk, since the bulk materials only have negligible surface atoms.

The quantum confinement of semiconductor nanocrystals was observed by pioneering work of Efros and Ekimov, [40, 41] Brus, [39, 42] and Henglein. [43] Classic quantum chemistry calculation of particle in a box model gave following results: [44]

$$E_n = \frac{h^2}{8m} \cdot \frac{n^2}{L^2} \tag{1-1}$$

Where E is the particle energy with quantum number n, h is the Planck constant, m is the particle mass, and L is the box size. Based on equation 1-1, one can deduce that the smaller the box, the higher the particle energy. The particle in a box model for equation 1-1 defined the particle in the vacuum, in order to better quantify the energy change for semiconductor nanocrystals, effective mass approximation model was proposed as following:

$$E = E_g + \frac{n^2h^2}{8d^2}\left(\frac{1}{m_e} + \frac{1}{m_h}\right) - \frac{1.8e^2}{4\pi\varepsilon_0\varepsilon d} \tag{1-2}$$

Where E_g is bulk semiconductor bandgap, n is interband transition number, d is nanocrystals size, m_e is electron effective mass, m_h is hole effective mass, e is elementary charge of the electron, ε_0 is the permittivity of free space, and ε is the dielectric constant of the solid. The middle term on the right side of equation 1-2 is the quantum confinement on electron and hole, and the third term on the right is the coulombic attraction between electron and hole. Since the increase of energy from quantum confinement are inversely proportional to the square of particle size, the decrease of energy from coulombic interaction are inversely proportional to the particle size, this led to the general trend that the decrease of particle size will induce higher energy.

In order to conveniently define the boundary condition at which size certain semiconductor nanocrystals will show quantum confinement, following ideas were introduced:

a. Exciton was introduced as the hydrogen-like electron excited to the CB with the hole created at the VB, with coulombic attraction between electron and hole.

b. Similar to hydrogen Bohr radius, which is the highest possibility of the distance between hydrogen electron and proton, exciton Bohr radius was introduced for every semiconductor nanocrystals based on following equation: [45]

$$a_B = \varepsilon \frac{m}{m^*} a_0 \tag{1-3}$$

Where a_B is exciton Bohr radius, ε is the dielectric constant of the material, m* is the mass of the particle, m is the rest mass of the electron, and a_0 is the Bohr radius of the hydrogen atom. For the exciton mass, it can be calculated as following:

$$\frac{1}{m^*} = \frac{1}{m_e} + \frac{1}{m_h} \tag{1-3a}$$

c. When the nanocrystals radius is smaller than the exciton Bohr radius, the semiconductor nanocrystals gradually show the quantum confinement effects.

Based on equation 1-3, we could deduce that the larger the semiconductor dielectric constant, and the smaller the exciton effective mass, the larger the corresponding exciton Bohr radius.

According to the k•p theory, a larger semiconductor bandgap is correlated with a larger exciton effective mass, which would generally lead to a smaller exciton Bohr radius as shown in Figure 1-4. [46]

The classic classification for quantum confinement based on dimension is as following: [47]

Bulk three-dimensional (3d) without quantum confinement, its density of states change as a function of energy is

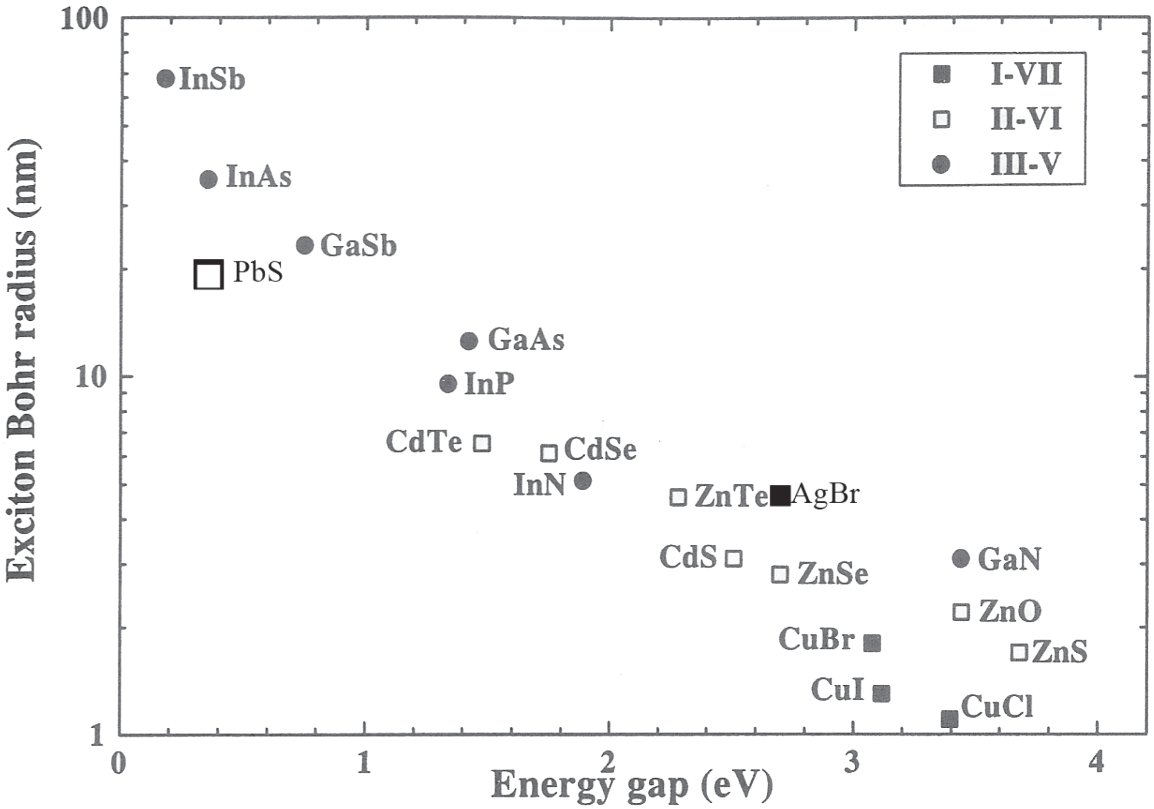

Figure 1-4. The exciton Bohr radius as a function of the energy gap in several I-VII, II-VI, and III-V semiconductor materials.

$$D_{3d}(E) \propto \sqrt{E} \qquad (1\text{-}4a)$$

Where $D_{3d}(E)$ is the density of states for 3d materials;

Two-dimensional (2d) quantum well type materials with one-dimensional quantum confinement along thickness direction, its density of states change as a function of energy is

$$D_{2d}(E) \propto 1 \qquad (1\text{-}4b)$$

Where $D_{2d}(E)$ is the density of states for 2d materials;

One-dimensional (1d) quantum rod type materials with two-dimensional quantum confinement along radial direction, its density of states change as a function of energy is

$D_{1d}(E) \propto 1/\sqrt{E}$ (1-4c)

Where $D_{1d}(E)$ is the density of states for 1d materials;

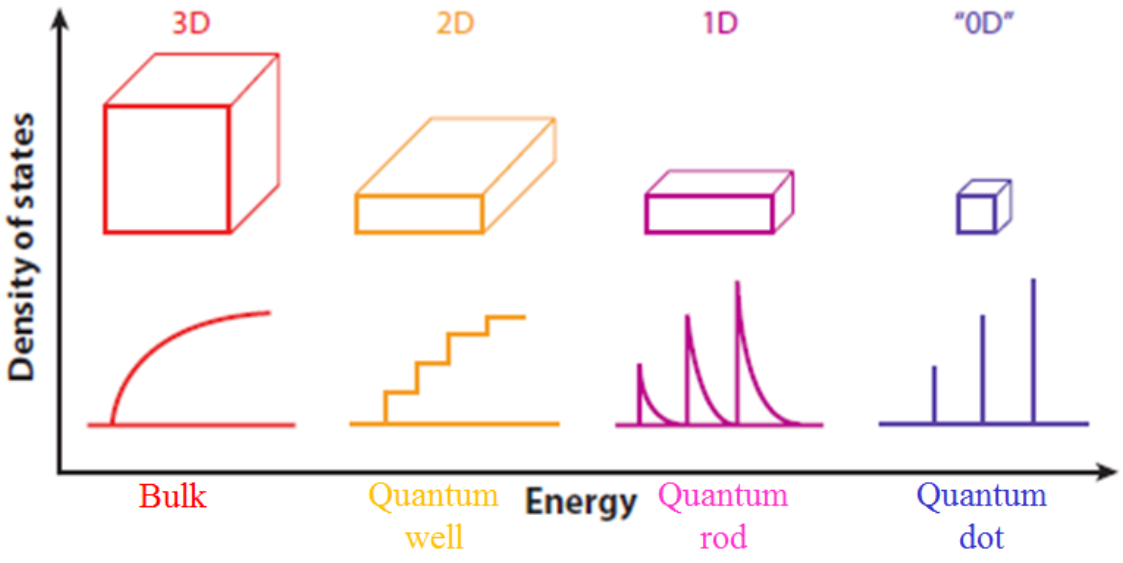

Figure 1-5. Density of states in one band of a semiconductor as a function of dimension.

And zero-dimensional (0d) quantum dot type materials with three-dimensional quantum confinement, only discrete energy levels are allowed.

The change of dimension and corresponding density of states are plotted in figure 1-5. [48-50] Since photon absorption are proportional to the density of states, absorption could be a direct probe for this unique system, and there are intriguing opportunities to tune the electron wavefunction distribution, viz. the electron wavefunction engineering.

1.2.2 Optical characterization

Since the absorption could easily be correlated with the energy states, and generally the semiconductor absorption energy are between 0.5 to 3.0 ev, which is in the ultraviolet and visible

range, UV-Vis absorption became the routine probe for the semiconductor nanocrystals. For the

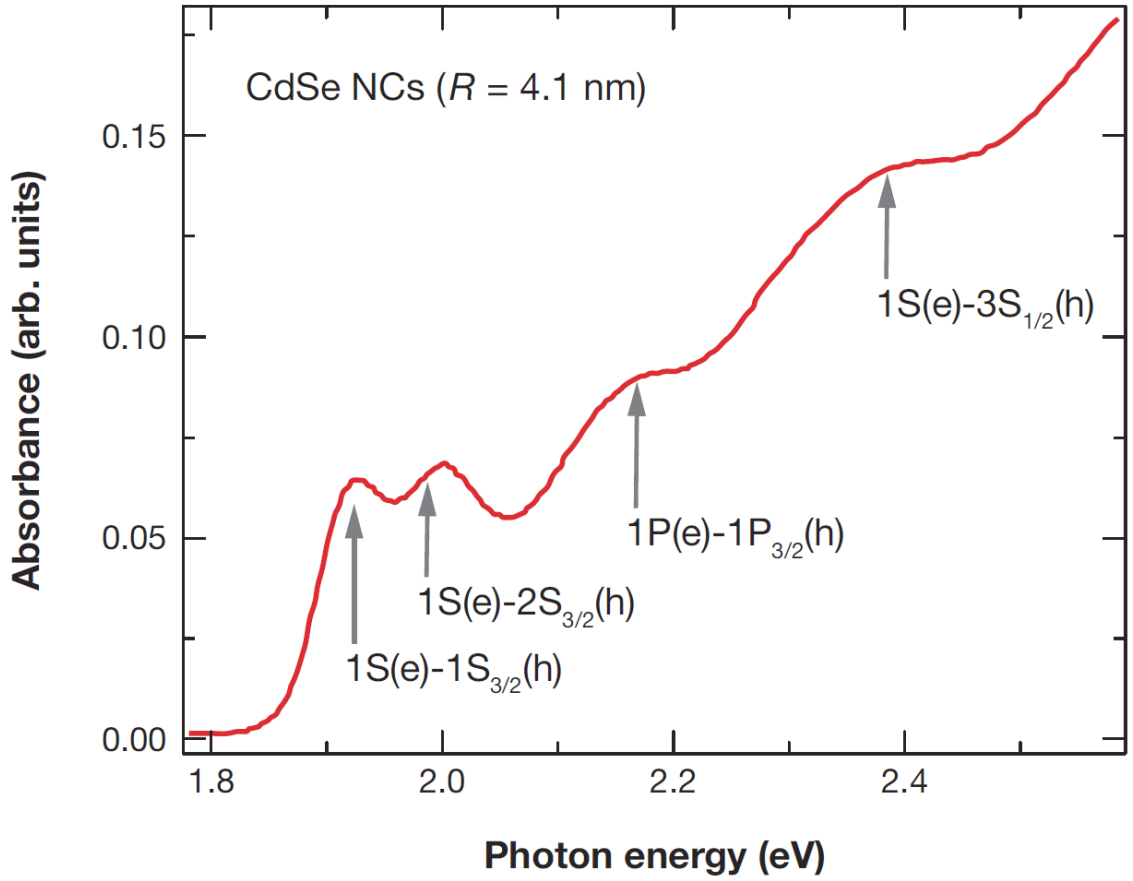

Figure 1-6. A linear (ground-state) absorption spectrum of CdSe nanocrystals with a mean radius of 4.1 nm. Arrows mark the positions of four well-resolved transitions that involve either the 1S or 1P electron states.

common semiconductor nanocrystals, CdSe are the most thoroughly investigated, and I'm going to take CdSe semiconductor nanocrystals as the model system to illustrate its band structure.

For the common II-VI semiconductor materials, such as CdSe, the HOMO/VB are composed by the linear combination of the atomic orbitals of Se^{2-}, which is the 4p state; and the LUMO/CB are made by the linear combination of the atomic orbitals of Cd^{2+}, which is the 5s state. [51-53] And

the photon absorption process is accompanied with the electron excitation from the VB to CB. In this case, the true quantum number is the total angular momentum, F, which is the sum of spin-orbit coupled angular momentum from corresponding atomic orbitals, J, and angular momentum from corresponding particle-in-a-box orbital envelop function, L, $F = J + L$. It's generally wrote in the form of nL_F, as shown in Figure 1-6, a typical CdSe quantum dot nanocrystals UV-Vis absorption with characteristic peaks could be assigned with corresponding electron states. [54, 55]

Given the discrete energy state of quantum dots, the intraband transition energy would be much larger than the phonon energy, making the phonon-assisted intraband transition inefficient, phonon bottleneck was thus proposed. [56, 57] Later on, ultrafast spectroscopy studies indicate that there is no difference between bulk semiconductor and corresponding quantum dots. [58-60] The relaxation of hot exciton, which is the excited electronic state higher than band-edge exciton, to the band-edge is in the subpicosecond scale. The absence of phonon bottleneck was ascribed to the hole-assisted energy dissipation, since hole generally have larger effective mass, and hence larger density of states than the electron. [61-64] So the quantum dots still follow the Kasha's rule, the intraband transition is much faster than the interband transition, and the observable photon emission at band-edge is still the only channel even though it may be excited to higher states, that is, the photoluminescence (PL) are independent of the excitation source wavelength.

The intraband transition of semiconductor quantum dots was measured on the subpicosecond scale, and the interband photon emission was characterized with PL lifetime measurement, which turns out to be on the tens of nanosecond (ns) scale. This is the fundamental reason behind the phenomena that PL emission is independent of excitation source wavelength. At the same time, it was realized that the semiconductor quantum dots lifetime is much longer than corresponding bulk materials, which was around 1 ns. [65] At first, this phenomenon was explained in accordance

with the surface effect, viz. the increase of surface area ratio when decreasing the size from bulk to nanometer scale. It was considered that the excited exciton was localized at the interface, leading to decreased electron/hole wavefunction overlap, and corresponding increase of lifetime. However, it turns out this anomalously long lifetime in semiconductor quantum dots could be successfully explained by the exciton fine structure.

Since the photon emission is always from the relaxation of band-edge exciton, in the case of CdSe quantum dots, it's the $1S_{1/2}$(e)-$1S_{3/2}$(h). The excited electron resides at the Cd 5s state, hole stays at the Se 4p state, and corresponding total angular momentum comes exclusively from the spin-orbital coupled angular momentum, with value J as 1/2 and 3/2, respectively. Generally the band-edge exciton state was treated as eightfold degenerate, however, in reality, some second-order effects need to be considered. The first effect is the routinely observed prolate instead of perfectly spherical quantum dots shape, together with the possible hexagonal wurzite structure, this crystal field effect will lift the hole state of $J = 3/2$ into $J_m = \pm 3/2$ (heavy hole) and $J_m = \pm 1/2$ (light hole) with corresponding crystal field splitting energy difference, where J_m is the projection of J. The second effect is the completely omitted electron-hole exchange interaction in the bulk case, which is proportional to the electron and hole wavefunction overlap, would become significant with the decrease of semiconductor volume from bulk to quantum dots. Since the total angular momentum for electron and hole at the band-edge are $F_e = 1/2$, $F_h = 3/2$, the band-edge exciton should be considered as the mixing between electron and hole, with totally angular momentum $N = F_e \pm F_h$, that is, fivefold degenerate $N = 2$, and threefold degenerate $N = 1$. The good quantum number after taking both effects into consideration would be N_m, the projection of total angular momentum N along the unique crystal axis. After taking these two effects into account, the initially eightfold degenerate band-edge exciton would be split into five

sublevels as shown in Figure 1-7 left. The total angular momentum N equal to 2 have lower energy than $N = 1$, in order to differentiate N_m with same value ($|N_m| > 0$ itself for each N value are twofold degenerate), it was labeled with N_m upper (^{U}) or lower (^{L}), corresponding to $N = 1$ or $N = 2$.

For CdSe quantum dots before photon absorption, the electronic states are closed shell configuration with total angular momentum of 0, and photon is spin 1 bosons, during the photon

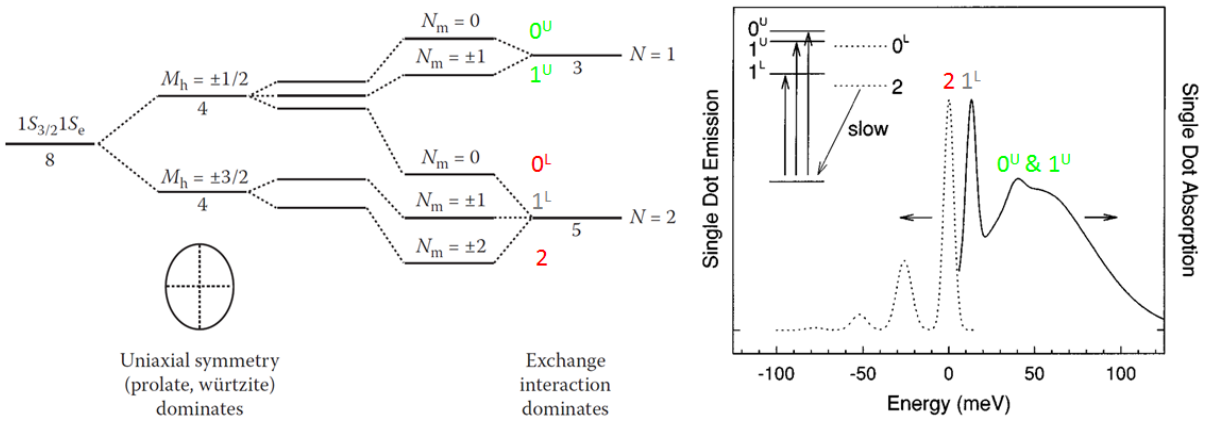

Figure 1-7. Energy-level diagram describing the exciton fine structure (left). Single dot absorption (solid line) and emission (dotted line) structure for ~1.9 nm effective radius CdSe nanocrystals (right).

absorption/emission, the electronic transition between ground state and excited state should have maximum angular momentum difference of 1, based upon the conservation of angular momentum rule. This indicates that the band-edge exciton with total angular momentum of 2 are optical passive states since the direct photon absorption/emission are forbidden. At the same time, since the optical absorption could excite CdSe quantum dots from ground state to the optical active states such as the states with total angular momentum of 1, it would relax to the band-edge 2 state following the Kasha's rule before photon emission. The recombination of band-edge exciton through photon emission would need the assistance of phonon to carry away the

excessive angular momentum. Since this process is three-particle procedure and more inefficient, its recombination rates are much smaller, resulting with the experimentally observed longer PL lifetime. As shown in Figure 1-7 right, this is the classic dark exciton theory, investigating the band-edge exciton fine structure and explaining its related phenomena such as the long PL lifetime. [66-68]

There are three points need further emphasis over here:

1. The crystal field splitting for the band-edge hole into heavy hole and light hole does not exist for zinc-blende and diamond lattices, since those two crystal structures are isotropic compared to the anisotropic wurzite structure. However, even take zinc-blende cubic CdSe as an example, the electron-hole exchange interaction still led to the splitting of eightfold degenerate band-edge exciton into similar dark exciton states [45] as detailed in the case of wurzite CdSe in the aforementioned paragraph, which means this phenomena is general in terms of crystal structures.
2. Although the band-edge absorption was assigned as 1^L in Figure 1-7 right, strictly speaking, its correlation with the total angular momentum of 2 should be treated as the optical passive states, and it was considered as only weakly allowed in small dots. [68]
3. The energy difference between states 1^L and 2 is the origin of stokes shift.

One of most promising applications of semiconductor quantum dots is the light emitting source, originating from its size-dependent quantum confinement and emission wavelength. Along this direction, tremendous efforts were devoted into the optimization of its PL quantum yield (QY), that is, the amount of photon emitted compared to the amount of photon absorbed. Detailed investigation discovered that semiconductor quantum dots emission property are highly

dependent upon its crystallinity and surface atoms, since the crystal defects and surface dangling bonds could form trapping sites, affecting its emission quality, and its quantum yield. In order to prepare single crystal semiconductor quantum dots, high temperature colloidal synthesis methods were developed to anneal away the crystal defects, into thermodynamically stable single crystals; [69] and saturating the dangling bonds with appropriate organic surfactants turns out to be a feasible method to enhance semiconductor nanocrystals emission quality. Later on, epitaxially growing another layer of inorganic semiconductor materials with higher bandgap as the shell forming type-I heterostructure was considered as the most effective way to insulate the core electron and hole wavefunction from environmental influence, [70-72] resulting with optimized optical properties and QY.

Although the semiconductor core matrix could be prepared with varied PL QY due to different synthesis protocol, there is generally one interesting phenomenon observed during the successive growth of shell materials. Taking classic type-I CdSe/ZnS as an example, during the increase of ZnS shell thickness, there is generally an increase of PL QY at the beginning of shell growth, and then the PL QY would gradually decrease with further shell growth. [71, 73-79] Intriguingly, this phenomenon could successfully be explained by following reasoning: [80-82]

For different core and shell composition, there would be lattice mismatch at the epitaxial interface. When the shell just started depositing on the core materials, it tends to contract/expand to align itself with the core lattice, however, when the shell became thicker and thicker, it starts returning to its original lattice constant. The tradeoff over here depends upon two factors:

1. The strain energy when shell materials tend to align itself with the core, and this energy is proportional to the shell volume;

2. The dislocation energy when the shell keeps its original lattice constant, the lattice mismatch and the related dislocation energy are proportional to the interface area.

Based upon the reciprocal energy interaction between the strain energy and dislocation energy, it would be reasonable to deduce that the shell materials tend to align the lattice with the core when the shell thickness is thin, and then gradually return to its intrinsic lattice constant with the increase of shell thickness. The thickness at which this transition occurs is the critical shell thickness. When the shell was thin, the shell tends to align its lattice with core, due to the increase of shell coverage to get rid of core dangling bonds and better insulate the core from environment, the PL QY would gradually increase; with further increase of shell thickness, the increase of shell volume would induce the shell lattice to maintain its intrinsic value, with the formation of lattice mismatch at the core/shell interface at the same time, which would be the defects sites quenching the PL emission, then the PL QY would gradually decrease.

1.3 Spectroscopic identification and common artifacts

For the chemical reaction going on at the molecular scale, spectroscopic probes are the most effective and efficient “eyes” for the chemists. Due to the limited experience and scope of my research, I’ll give a selective and brief introduction to some related spectroscopic methods, especially some common artifacts.

1.3.1 Nuclear magnetic resonance (NMR)

The success of organic chemistry largely relies on the reliable and convenient NMR probe to study related systems. For the magnetic active nuclei (nuclei spin quantum number $S \neq 0$), it could absorb specific wavelength radiofrequency radiation under certain magnetic field due to the Zeeman effect, not only each nuclei has its specific "fingerprint" radiofrequency range, most importantly, its absorption frequency was also influenced by the surrounding electrons, which is the chemical environment around each nuclei. In this way, the chemical environment around certain magnetic active nuclei could be conveniently detected by the NMR: generally speaking, the lower the electron density around the nuclei, the higher magnetic field the nuclei could feel, and higher corresponding resonance frequency. This is the famous chemical shift in the NMR axis to label the chemical species. [83-85]

Besides numerous advantage of NMR such as noninvasive, highly selective, etc. one merits of

Delay time (s)	CH	CH_2
0.3	0.78	1.70
0.6	0.78	1.70
1	0.83	1.77
5	0.91	1.90
10	0.96	1.96
20	0.95	1.94
60	0.99	1.99

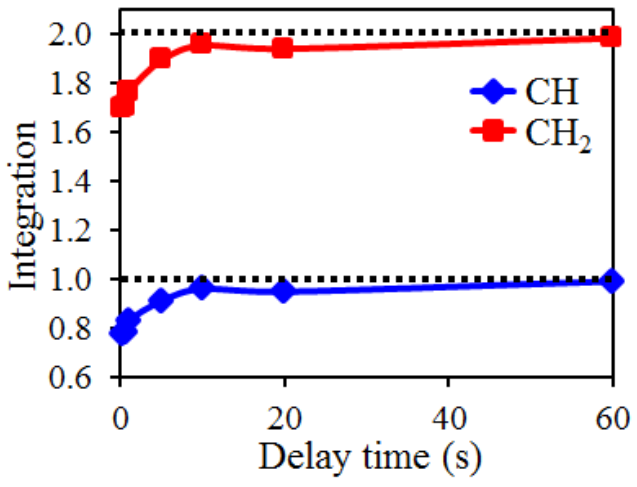

Figure 1-8. Quantitative proton NMR study on the high purity 1-Octadecene (99.5%), with methyl group integration normalized to 3 and varied recycle delay time.

this methods is that it could be used to quantitative analyze the chemical components, which is significant and fundamental to our understanding to chemical systems. However, the quantitative analysis could easily be overwhelmed by the time and artifacts during the process. Taken the most routine proton NMR as an example, we used it to quantitatively analyze high purity 1-Octadecene (99.5%), its functional group could easily be identified by corresponding chemical shifts, and the amount could be calculated by the peak area integration. By normalizing the methyl group peak integration value to 3 for the CH_3, we calculated the corresponding double bond CH and CH_2 amount with value as around 0.78 and 1.70, which is far from the expected value of 1 and 2 based on the chemical formula.

It turns out that under routine proton NMR analysis, in order to get better signal to noise ratio, the recycle delay time, the amount of time waited after each excitation and data collection period was shortened to around 0.3 second. However, with such short time, the excited nuclei has not recovered from the excited states to the corresponding Boltzmann distribution, and continuous excitation would artificially make the detected signal smaller than the ideal value. [86] As shown in Figure 1-8, after elongating the recycle delay time gradually from 0.3 to 60 seconds, we could see that corresponding integration value for double bond CH and CH_2 started to converge to 1 and 2, the expected theoretical value under properly set NMR parameters. In this way, we could see that quantitative NMR studies are not only meticulous, but also time consuming, for each data collection cycle, the recycle delay time from 0.3 to 60 seconds would make routine 64 scans taking from around 5 minutes to 1 hour and 8 minutes. For other nuclei, since its relative signal sensitivity are generally lower than proton, and nuclear overhauser effect needs to be taken into account, making quantitative analysis projects even more frightening.

1.3.2 Photoluminescence (PL) and Photoluminescence excitation (PLE)

In order to avoid excitation source scattering interference, the PL detection was set with 90 degree angle with the excitation light path. There are two common artifacts need attention in routine measurement:

1. Inner filter effect. The reabsorption of PL between molecules in the sample, that is, molecule with absorption range in the emission of other molecules could absorb its PL emission. This intermolecular energy transfer would generally make redder emission more advantageous than the high energy bluer ones from the reabsorption, at the same time, the final spectrum collected at the PL detector would reflect this fact. Especially, for the PL QY measurement, accurate and reliable results needs to be carried out under sufficiently low optical density to avoid inner filter effects, that is, through reducing particle concentration in the sample to decrease the possibility of intermolecular reabsorption. [87]
2. Second order diffraction. In order to differentiate the emission wavelength, generally monochromator was applied between the sample and detector in the emission light path. For the most monochromator, diffraction grating was set up to selectively diffract light with certain wavelength at specific angle according to equation 1-5:

   $$d\sin\theta = n\lambda \quad (1\text{-}5)$$

   where d is distance between adjacent grating, θ is the angle between the diffracted ray and the grating's normal vector, n is an integer, and λ is light wavelength.

   For example, the diffraction grating was set to selectively diffract light with wavelength at 600 nm, based on equation 1-5, the light at 300 nm could possibly diffracted with n (λ = 300 nm) = 2 n (λ = 600 nm), that is the origin of second order diffraction. In this case,

the 300 nm light would be collected as if it's the light with wavelength at 600 nm. In order to avoid this effect, especially the excitation light source with strong scattering, the parameter set up for the detection range during the experiments should be smaller than two times of excitation wavelength; however, if in certain case this could not be met, properly put bandpass excitation filter between the sample and monochromator could be used to avoid this effect. [87] Or else, this artifact could possibly mistakenly be treated as the signal from the sample. [88, 89]

PLE is complementary to absorption spectrum, on that the emission intensity at certain wavelength or range was detected by scanning through varied excitation wavelength. By comparing the PLE profile with corresponding absorption, the emission origin could be successfully identified. Besides, PLE could be used to resolve optical heterogeneity, that is, the red shifting of PLE detection wavelength, the corresponding PLE peak position could resolve sample homogeneity. [90-92]

1.3.3 Energy-dispersive X-ray spectroscopy (EDX)

For the electrons at inner shell of the chemical compounds, it could be excited to escape from the compounds, forming ions with hole left at original shell, and the relaxation of electrons at higher energy states to the hole position could possibly generate X-rays to dissipate the excess energy during the relaxation process. Since every atom has its specific electron configuration, this inter-shell electron transition and corresponding X-ray energy is the "fingerprint" of the nuclei, making EDX one of most adopted methods for elemental analysis. For the common excitation

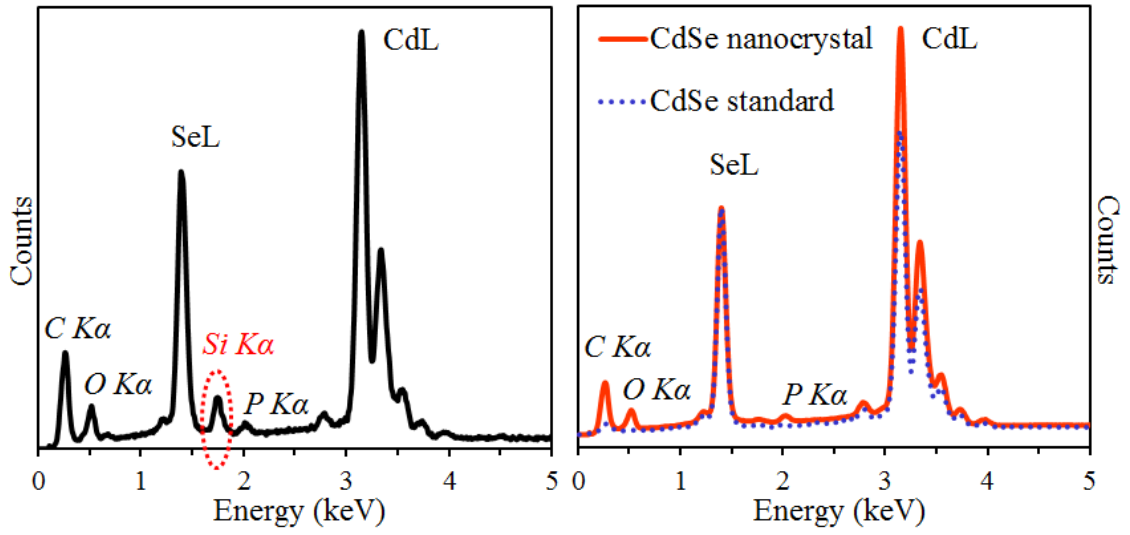

Figure 1-9. EDX spectrum of the CdSe nanocrystals (left), EDX spectra of properly purified CdSe nanocrystals and CdSe standard (right).

source, it could be high energy electron or photon, which is the electron microscope coupled with EDX or X-ray fluorescence (XRF), respectively.

During the routine elemental analysis for CdSe semiconductor nanocrystals with EDX coupled to (Environmental Scanning Electron Microscope) ESEM, there was one bizarre phenomenon observed: the seemingly random appearance of Si *Kα* signal on EDX as shown in Figure 1-9 left. Since there should not be any silicon in the aimed analyte, this ghost peak was really annoying and hard to explain. After carefully designed control experiments and analysis, this artifact could successfully be explained by following facts:

In order to separate the sample chamber from the common Si(Li) detector, generally a Beryllium window with Si grid support was used to withstand pressure difference, during the travel path of emitted X-ray from sample to Si(Li) detector, there is a possibility that the X-ray was collided with the Si grid support instead of going through the “transparent” Be window. And the X-ray could possibly be absorbed by the Si grid with the sample X-ray as excitation source just as in

the case of XRF, with emission from Si grid to the Si(Li) detector. [93] More importantly, there is possibility that the Si components in the Si(Li) detector itself would play similar role as the Si grid in the Be window, with the generation of Si X-ray, which is called as the Silicon internal fluorescence peak. [94]

Then the question comes to when would this silicon peak appear? Since the experimental results seems to be somehow random detection of silicon peak. This would highly dependent upon the Si mass absorption coefficient as a function of X-ray energy as shown in Figure 1-10 and equation 1-6. [95]

$$I = I_0 \exp[-(\frac{\mu}{\rho})\rho t] \quad (1\text{-}6)$$

Where I is transmitted intensity, I_0 is the incident intensity, $\frac{\mu}{\rho}$ is the mass absorption coefficient (cm^2/g), ρ is the density (g/cm^3), and t is the thickness (cm) of the absorber.

Since ρ and t is constant in this case, the absorption of Si is highly dependent upon the mass absorption coefficient, which is a function of X-ray energy as shown in Figure 1-10. The absorption coefficient has the peak value just pass Si K-edge (1.84 KeV), then decrease rapidly with the increase of X-ray energy. It's reasonably to see that the element just after Si with K emission would have large absorption coefficient for Si, which is the P *Kα* emission with energy at around 2.01 KeV. And for the synthesis of colloidal CdSe nanocrystals, trialkylphosphine are generally used, and we did see the P *Kα* signal in Figure 1-9 left. Following the logic behind this, if the trialkylphosphine could be properly purified away, the Si ghost signal would disappear with the elimination of P elements, which is the case as seen in Figure 1-9 right for the properly purified CdSe nanocrystals, only trace amount of P signal was detected, and the Si ghost signal

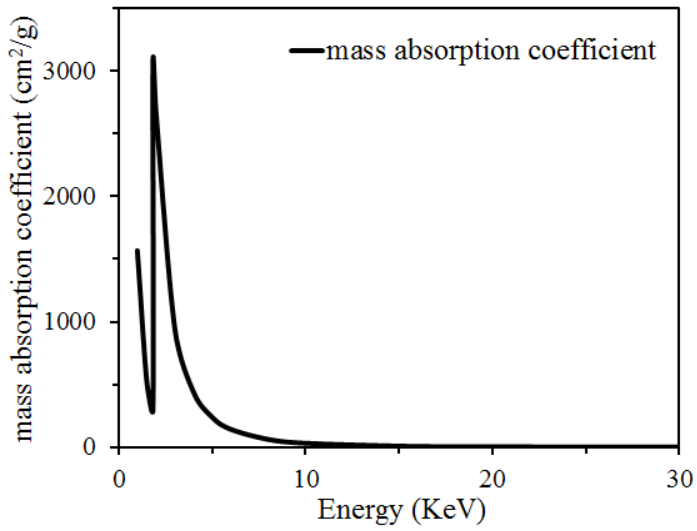

Figure 1-10. Si mass absorption coefficient as a function of X-ray energy.

was almost completely removed. Intriguingly, there are other elements such as Y (*Lα1*, 1.92 KeV), Re (*Mα1*, 1.84 KeV), Os (*Mα1*, 1.91 KeV), and Ir (*Mα1*, 1.98 KeV) have the X-ray emission energy just pass the Si K-edge, which would induce significant absorption and emission from the Si. Preliminary literature research on this found out that Y related compound under EDX study did show considerable Si signal, which should not be observed from the analyte. [96]

In order to avoid this artifact, proper purification such as in the case of colloidal CdSe nanocrystals should be exerted. If the components could not be purified away such as in the case of Y related compound, using EDX with silicon drift detector would get rid of the internal fluorescence, or by switching to the higher energy resolution wavelength-dispersive X-ray spectroscopy would avoid this problem. [71, 94] Most importantly, this artifact should not be treated as the signal from the analyte.

There is another minor point I'd like to mention over here: In order to get quantitative accurate elemental analysis results from EDX, reasonable amount of sample and properly arranged

control should be applied. Generally, scanning electron microscope (SEM) would be an ideal platform for this. However, since semiconductor nanocrystals are intrinsically not a good conductor for the electrons, how to avoid the charging from semiconductor nanocrystals sample became critical. Although traditionally applying gold sputter coating on the sample surface would guide the electron to the carbon conductive tape, the elemental analysis accuracy would be affected since the control would be more difficult and X-ray emitted from the sample with different energy has varied absorption possibility at the gold coating, affecting the final counting accuracy at the detector. Fortunately, the development of pressure controlled valve made it possible to have reasonable high pressure at the sample chamber, at the same time maintain enough low air pressure at the electron source to protect it from burning damage, which is the environmental-SEM. The benefit from this is that the air moisture in the sample chamber will be ionized into H^+ and OH^- at the sample and air interface, and transporting away the excess electron to avoid charging problem, at the same time making the traditional gold coating on sample unnecessary. [94] So the ESEM coupled with EDX would be the ideal platform for the elemental analysis of semiconductor nanocrystals.

1.4 Dissertation Objective and Overview

While synthesis of semiconductor nanocrystals has been in rapid development, the related molecular mechanism studies are rare, which leaves synthetic chemistry of colloidal nanocrystals at an empirical level. The objective of this dissertation is to illustrate that systematic and quantitative study of molecular mechanism for the formation of colloidal nanocrystals is possible, and the results will not only help us to understand formation mechanisms of colloidal nanocrystals but also advance their synthetic methods in chapter two.

At present, synthetic methods for colloidal semiconductor nanocrystals with three-dimensional quantum confinement (quantum dots) and two-dimensional confinement (quantum rods) have been reasonably developed. In chapter three, we will discuss formation of colloidal-stable disk-shaped II-VI semiconductor nanocrystals as one-dimensional quantum confinement systems (quantum disks). Then in chapter four, some unique properties of these new quantum objects, such as size-dependent lattice dilation, extremely sharp band-edge photoluminescence, and two-order of magnitude faster photoluminescence decay compared to quantum dots, shall be discussed.

1.5 References

1. Eigler, D. M.; Schweizer, E. K. Positioning Single Atoms With A Scanning Tunneling Microscope. *Nature* **1990**, *344*, 524-526.

2. Jones, R. Feynman's unfinished business. *Nature Nanotechnology* **2009**, *4*, 785-785.

3. Toumey, C. 35 atoms that changed the nanoworld. *Nature Nanotechnology* **2010**, *5*, 239-241.

4. Mohn, F.; Gross, L.; Moll, N.; Meyer, G. Imaging the charge distribution within a single molecule. *Nature Nanotechnology* **2012**, *7*, 227-231.

5. Grutter, P. Scanning Probe Microscopy Seeing the Charge Within. *Nature Nanotechnology* **2012**, *7*, 210-211.

6. Yang, P.; Yan, R.; Fardy, M. Semiconductor Nanowire: What's Next? *Nano Letters* **2010**, *10*, 1529-1536.

7. Ahmadi, T. S.; Wang, Z. L.; Green, T. C.; Henglein, A.; ElSayed, M. A. Shape-controlled synthesis of colloidal platinum nanoparticles. *Science* **1996**, *272*, 1924-1926.

8. Daniel, M. C.; Astruc, D. Gold nanoparticles: Assembly, supramolecular chemistry, quantum-size-related properties, and applications toward biology, catalysis, and nanotechnology. *Chemical Reviews* **2004**, *104*, 293-346.

9. Lim, B.; Jiang, M.; Camargo, P. H. C.; Cho, E. C.; Tao, J.; Lu, X.; Zhu, Y.; Xia, Y. Pd-Pt Bimetallic Nanodendrites with High Activity for Oxygen Reduction. *Science* **2009**, *324*, 1302-1305.

10. Akerman, M. E.; Chan, W. C. W.; Laakkonen, P.; Bhatia, S. N.; Ruoslahti, E. Nanocrystal targeting in vivo. *Proceedings of the National Academy of Sciences of the United States of America* **2002**, *99*, 12617-12621.

11. Allen, T. M.; Cullis, P. R. Drug delivery systems: Entering the mainstream. *Science* **2004**, *303*, 1818-1822.

12. Gao, X. H.; Cui, Y. Y.; Levenson, R. M.; Chung, L. W. K.; Nie, S. M. In vivo cancer targeting and imaging with semiconductor quantum dots. *Nature Biotechnology* **2004**, *22*, 969-976.

13. Bruchez, M.; Moronne, M.; Gin, P.; Weiss, S.; Alivisatos, A. P. Semiconductor nanocrystals as fluorescent biological labels. *Science* **1998**, *281*, 2013-2016.

14. Chan, W. C. W.; Nie, S. M. Quantum dot bioconjugates for ultrasensitive nonisotopic detection. *Science* **1998**, *281*, 2016-2018.

15. Whitesides, G. M. The 'right' size in nanobiotechnology. *Nature Biotechnology* **2003**, *21*, 1161-1165.

16. Michalet, X.; Pinaud, F. F.; Bentolila, L. A.; Tsay, J. M.; Doose, S.; Li, J. J.; Sundaresan, G.; Wu, A. M.; Gambhir, S. S.; Weiss, S. Quantum dots for live cells, in vivo imaging, and diagnostics. *Science* **2005**, *307*, 538-544.

17. Resch-Genger, U.; Grabolle, M.; Cavaliere-Jaricot, S.; Nitschke, R.; Nann, T. Quantum dots versus organic dyes as fluorescent labels. *Nature Methods* **2008**, *5*, 763-775.

18. Greenham, N. C.; Peng, X. G.; Alivisatos, A. P. Charge separation and transport in conjugated-polymer/semiconductor-nanocrystal composites studied by photoluminescence quenching and photoconductivity. *Physical Review B* **1996**, *54*, 17628-17637.

19. Huynh, W. U.; Dittmer, J. J.; Alivisatos, A. P. Hybrid nanorod-polymer solar cells. *Science* **2002**, *295*, 2425-2427.

20. Semonin, O. E.; Luther, J. M.; Choi, S.; Chen, H. Y.; Gao, J.; Nozik, A. J.; Beard, M. C. Peak External Photocurrent Quantum Efficiency Exceeding 100% via MEG in a Quantum Dot Solar Cell. *Science* **2011**, *334*, 1530-3.

21. Colvin, V. L.; Schlamp, M. C.; Alivisatos, A. P. Light-Emitting-Diodes Made From Cadmium Selenide Nanocrystals And A Semiconducting Polymer. *Nature* **1994**, *370*, 354-357.

22. Lee, J.; Sundar, V. C.; Heine, J. R.; Bawendi, M. G.; Jensen, K. F. Full color emission from II-VI semiconductor quantum dot-polymer composites. *Advanced Materials* **2000**, *12*, 1102-+.

23. Coe, S.; Woo, W. K.; Bawendi, M.; Bulovic, V. Electroluminescence from single monolayers of nanocrystals in molecular organic devices. *Nature* **2002**, *420*, 800-803.

24. Dai, Q.; Duty, C. E.; Hu, M. Z. Semiconductor-Nanocrystals-Based White Light-Emitting Diodes. *Small* **2010**, *6*, 1577-1588.

25. Moore, G. E. Cramming more components onto integrated circuits (Reprinted from Electronics, pg 114-117, April 19, 1965). *Proceedings of the Ieee* **1998**, *86*, 82-85.

26. Schaller, R. R. Moore's Law: Past, present, and future. *Ieee Spectrum* **1997**, *34*, 52-&.

27. Lundstrom, M. Moore's law forever? *Science* **2003**, *299*, 210-211.

28. Madelung, O., *Semiconductors : data handbook*. Springer: Berlin; New York, 2004.

29. Peng, X. Band Gap and Composition Engineering on a Nanocrystal (BCEN) in Solution. *Accounts of Chemical Research* **2010**, *43*, 1387-1395.

30. Van de Walle, C. G.; Neugebauer, J. Universal alignment of hydrogen levels in semiconductors, insulators and solutions. *Nature* **2003**, *423*, 626-628.

31. Norris, D. J.; Efros, A. L.; Erwin, S. C. Doped nanocrystals. *Science* **2008**, *319*, 1776-1779.

32. Alivisatos, A. P. Perspectives on the physical chemistry of semiconductor nanocrystals. *Journal of Physical Chemistry* **1996**, *100*, 13226-13239.

33. Murray, C. B.; Kagan, C. R.; Bawendi, M. G. Synthesis and characterization of monodisperse nanocrystals and close-packed nanocrystal assemblies. *Annual Review of Materials Science* **2000**, *30*, 545-610.

34. Yin, Y.; Alivisatos, A. P. Colloidal nanocrystal synthesis and the organic-inorganic interface. *Nature* **2005**, *437*, 664-670.

35. Peng, X. G. An essay on synthetic chemistry of colloidal nanocrystals. *Nano Research* **2009**, *2*, 425-447.

36. Brus, L. Commentary: Carbon Nanotubes, CdSe Nanocrystals, and Electron-Electron Interaction. *Nano Letters* **2010**, *10*, 363-365.

37. Smith, A. M.; Nie, S. Semiconductor Nanocrystals: Structure, Properties, and Band Gap Engineering. *Accounts of Chemical Research* **2010**, *43*, 190-200.

38. Peng, Z. A.; Peng, X. G. Nearly monodisperse and shape-controlled CdSe nanocrystals via alternative routes: Nucleation and growth. *Journal of the American Chemical Society* **2002**, *124*, 3343-3353.

39. Brus, L. E. Electron Electron And Electron-Hole Interactions In Small Semiconductor Crystallites - The Size Dependence Of The Lowest Excited Electronic State. *Journal of Chemical Physics* **1984**, *80*, 4403-4409.

40. Efros, A. L.; Efros, A. L. Interband Absorption Of Light In A Semiconductor Sphere. *Soviet Physics Semiconductors-Ussr* **1982**, *16*, 772-775.

41. Ekimov, A. I.; Efros, A. L.; Onushchenko, A. A. Quantum Size Effect In Semiconductor Microcrystals. *Solid State Communications* **1985**, *56*, 921-924.

42. Rossetti, R.; Nakahara, S.; Brus, L. E. Quantum Size Effects In The Redox Potentials, Resonance Raman-Spectra, And Electronic-Spectra Of CdS Crystallites In Aqueous-Solution. *Journal of Chemical Physics* **1983**, *79*, 1086-1088.

43. Weller, H.; Koch, U.; Gutierrez, M.; Henglein, A. Photochemistry Of Colloidal Metal Sulfides .7. Absorption And Fluorescence Of Extremely Small Zns Particles - The World Of The Neglected Dimensions. *Berichte Der Bunsen-Gesellschaft-Physical Chemistry Chemical Physics* **1984**, *88*, 649-656.

44. McQuarrie, D. A., *Quantum chemistry*. University Science Books: Sausalito, Calif., 2008.

45. Klimov, V. I., *Nanocrystal quantum dots*. CRC Press: Boca Raton, 2010.

46. Grahn, H. T., *Introduction to semiconductor physics*. World Scientific: Singapore; River Edge, NJ, 1999.

47. Schmid, G., *Nanoparticles : from theory to application*. Wiley-VCH: Weinheim, 2010.

48. Yoffe, A. D. Low-Dimensional Systems - Quantum-Size Effects And Electronic-Properties Of Semiconductor Microcrystallites (Zero-Dimensional Systems) And Some Quasi-2-Dimensional Systems. *Advances in Physics* **1993**, *42*, 173-266.

49. Alivisatos, A. P. Semiconductor clusters, nanocrystals, and quantum dots. *Science* **1996**, *271*, 933-937.

50. Choi, C. L.; Alivisatos, A. P., From Artificial Atoms to Nanocrystal Molecules: Preparation and Properties of More Complex Nanostructures. In *Annual Review of Physical Chemistry, Vol 61*, Annual Reviews: Palo Alto, 2010; Vol. 61, pp 369-389.

51. Nirmal, M.; Brus, L. Luminescence photophysics in semiconductor nanocrystals. *Accounts of Chemical Research* **1999**, *32*, 407-414.

52. Soloviev, V. N.; Eichhofer, A.; Fenske, D.; Banin, U. Molecular limit of a bulk semiconductor: Size dependence of the "band gap" in CdSe cluster molecules. *Journal of the American Chemical Society* **2000**, *122*, 2673-2674.

53. El-Sayed, M. A. Small is different: Shape-, size-, and composition-dependent properties of some colloidal semiconductor nanocrystals. *Accounts of Chemical Research* **2004**, *37*, 326-333.

54. Ekimov, A. I.; Hache, F.; Schanneklein, M. C.; Ricard, D.; Flytzanis, C.; Kudryavtsev, I. A.; Yazeva, T. V.; Rodina, A. V.; Efros, A. L. Absorption And Intensity-Dependent Photoluminescence Measurements On CdSe Quantum Dots - Assignment Of The 1st Electronic-Transitions. *Journal of the Optical Society of America B-Optical Physics* **1993**, *10*, 100-107.

55. Klimov, V. I., Spectral and dynamical properties of multilexcitons in semiconductor nanocrystals. In *Annual Review of Physical Chemistry*, 2007; Vol. 58, pp 635-673.

56. Bockelmann, U.; Bastard, G. Phonon-Scattering And Energy Relaxation In 2-Dimensional, One-Dimensional, And Zero-Dimensional Electron Gases. *Physical Review B* **1990**, *42*, 8947-8951.

57. Benisty, H.; Sotomayortorres, C. M.; Weisbuch, C. Intrinsic Mechanism For The Poor Luminescence Properties Of Quantum-Box Systems. *Physical Review B* **1991**, *44*, 10945-10948.

58. Klimov, V. I.; McBranch, D. W. Femtosecond 1P-to-1S electron relaxation in strongly confined semiconductor nanocrystals. *Physical Review Letters* **1998**, *80*, 4028-4031.

59. Xu, S.; Mikhailovsky, A. A.; Hollingsworth, J. A.; Klimov, V. I. Hole intraband relaxation in strongly confined quantum dots: Revisiting the "phonon bottleneck" problem. *Physical Review B* **2002**, *65*, 5.

60. Schaller, R. D.; Pietryga, J. M.; Goupalov, S. V.; Petruska, M. A.; Ivanov, S. A.; Klimov, V. I. Breaking the phonon bottleneck in semiconductor nanocrystals via multiphonon emission induced by intrinsic nonadiabatic interactions. *Physical Review Letters* **2005**, *95*, 4.

61. Efros, A. L.; Kharchenko, V. A.; Rosen, M. Breaking The Phonon Bottleneck In Nanometer Quantum Dots - Role Of Auger-Like Processes. *Solid State Communications* **1995**, *93*, 281-284.

62. Wang, L. W.; Califano, M.; Zunger, A.; Franceschetti, A. Pseudopotential theory of Auger processes in CdSe quantum dots. *Physical Review Letters* **2003**, *91*.

63. Hendry, E.; Koeberg, M.; Wang, F.; Zhang, H.; Donega, C. D.; Vanmaekelbergh, D.; Bonn, M. Direct observation of electron-to-hole energy transfer in CdSe quantum dots. *Physical Review Letters* **2006**, *96*.

64. Pandey, A.; Guyot-Sionnest, P. Slow Electron Cooling in Colloidal Quantum Dots. *Science* **2008**, *322*, 929-932.

65. Henry, C. H.; Nassau, K. Lifetimes Of Bound Excitons In CdS. *Physical Review B* **1970**, *1*, 1628-1634.

66. Nirmal, M.; Norris, D. J.; Kuno, M.; Bawendi, M. G.; Efros, A. L.; Rosen, M. Observation Of The Dark Exciton In CdSe Quantum Dots. *Physical Review Letters* **1995**, *75*, 3728-3731.

67. Efros, A. L.; Rosen, M.; Kuno, M.; Nirmal, M.; Norris, D. J.; Bawendi, M. Band-edge exciton in quantum dots of semiconductors with a degenerate valence band: Dark and bright exciton states. *Physical Review B* **1996**, *54*, 4843-4856.

68. Norris, D. J.; Efros, A. L.; Rosen, M.; Bawendi, M. G. Size dependence of exciton fine structure in CdSe quantum dots. *Physical Review B* **1996**, *53*, 16347-16354.

69. Steigerwald, M. L.; Brus, L. E. Semiconductor Crystallites - A Class Of Large Molecules. *Accounts of Chemical Research* **1990**, *23*, 183-188.

70. Hines, M. A.; Guyot-Sionnest, P. Synthesis and characterization of strongly luminescing ZnS-Capped CdSe nanocrystals. *Journal of Physical Chemistry* **1996**, *100*, 468-471.

71. Dabbousi, B. O.; RodriguezViejo, J.; Mikulec, F. V.; Heine, J. R.; Mattoussi, H.; Ober, R.; Jensen, K. F.; Bawendi, M. G. (CdSe)ZnS core-shell quantum dots: Synthesis and characterization of a size series of highly luminescent nanocrystallites. *Journal of Physical Chemistry B* **1997**, *101*, 9463-9475.

72. Peng, X. G.; Schlamp, M. C.; Kadavanich, A. V.; Alivisatos, A. P. Epitaxial growth of highly luminescent CdSe/CdS core/shell nanocrystals with photostability and electronic accessibility. *Journal of the American Chemical Society* **1997**, *119*, 7019-7029.

73. Talapin, D. V.; Rogach, A. L.; Kornowski, A.; Haase, M.; Weller, H. Highly luminescent monodisperse CdSe and CdSe/ZnS nanocrystals synthesized in a hexadecylamine-trioctylphosphine oxide-trioctylphospine mixture. *Nano Letters* **2001**, *1*, 207-211.

74. Mokari, T.; Banin, U. Synthesis and properties of CdSe/ZnS core/shell nanorods. *Chemistry of Materials* **2003**, *15*, 3955-3960.

75. Talapin, D. V.; Mekis, I.; Gotzinger, S.; Kornowski, A.; Benson, O.; Weller, H. CdSe/CdS/ZnS and CdSe/ZnSe/ZnS core-shell-shell nanocrystals. *Journal of Physical Chemistry B* **2004**, *108*, 18826-18831.

76. Xie, R. G.; Kolb, U.; Li, J. X.; Basche, T.; Mews, A. Synthesis and characterization of highly luminescent CdSe-Core CdS/Zn0.5Cd0.5S/ZnS multishell nanocrystals. *Journal of the American Chemical Society* **2005**, *127*, 7480-7488.

77. Reiss, P.; Protiere, M.; Li, L. Core/Shell Semiconductor Nanocrystals. *Small* **2009**, *5*, 154-168.

78. Xia, X.; Liu, Z.; Du, G.; Li, Y.; Ma, M. Structural Evolution and Photoluminescence of Zinc-Blende CdSe-Based CdSe/ZnS Nanocrystals. *Journal of Physical Chemistry C* **2010**, *114*, 13414-13420.

79. Ghosh Chaudhuri, R.; Paria, S. Core/Shell Nanoparticles: Classes, Properties, Synthesis Mechanisms, Characterization, and Applications. *Chemical Reviews* **2011**.

80. Herman, M. A.; Richter, W.; Sitter, H., *Epitaxy : physical principles and technical implementation*. Springer: Berlin; New York, 2004.

81. Ayers, J. E., *Heteroepitaxy of semiconductors : theory, growth, and characterization*. CRC Press: Boca Raton, 2007.

82. Yu, P. Y.; Cardona, M., *Fundamentals of semiconductors : physics and materials properties*. Springer: Berlin; London, 2009.

83. Abragam, A., *The principles of nuclear magnetism*. Clarendon Press: Oxford, 1961.

84. Silverstein, R. M.; Webster, F. X.; Kiemle, D. J., *Spectrometric identification of organic compounds*. John Wiley & Sons: Hoboken, NJ, 2005.

85. Levitt, M. H., *Spin dynamics : basics of nuclear magnetic resonance*. Wiley: Hoboken, N.J., 2008.

86. Grant, D. M.; Harris, R. K., *Encyclopedia of nuclear magnetic resonance*. John Wiley: Chichester; New York, 1996.

87. Lakowicz, J. R., *Principles of fluorescence spectroscopy*. Springer: New York, 2006.

88. Rahman, A. F. M. M.; Bhattacharya, S.; Peng, X.; Kimura, T.; Komatsu, N. Unexpectedly large binding constants of azulenes with fullerenes. *Chemical Communications* **2008**, 1196-1198.

89. Stella, L.; Capodilupo, A. L.; Bietti, M. A reassessment of the association between azulene and 60 fullerene. Possible pitfalls in the determination of binding constants through fluorescence spectroscopy. *Chemical Communications* **2008**, 4744-4746.

90. Chen, X. B.; Samia, A. C. S.; Lou, Y. B.; Burda, C. Investigation of the crystallization process in 2 nm CdSe quantum dots. *Journal of the American Chemical Society* **2005**, *127*, 4372-4375.

91. Dorfs, D.; Salant, A.; Popov, I.; Banin, U. ZnSe quantum dots within CdS nanorods: A seeded-growth type-II system. *Small* **2008**, *4*, 1319-1323.

92. Riehle, F. S.; Bienert, R.; Thomann, R.; Urban, G. A.; Kruegert, M. Blue Luminescence and Superstructures from Magic Size Clusters of CdSe. *Nano Letters* **2009**, *9*, 514-518.

93. Garratt-Reed, A. J.; Bell, D. C., *Energy-dispersive X-ray analysis in the electron microscope*. BIOS: Oxford, 2003.

94. Goldstein, J., *Scanning electron microscopy and x-ray microanalysis*. Kluwer Academic/Plenum Publishers: New York, 2003.

95. http://www.nist.gov/pml/data/xraycoef/index.cfm.

96. Mamak, M.; Metraux, G. S.; Petrov, S.; Coombs, N.; Ozin, G. A.; Green, M. A. Lanthanum strontium manganite/yttria-stabilized zirconia nanocomposites derived from a surfactant assisted, co-assembled mesoporous phase. *Journal of the American Chemical Society* **2003**, *125*, 5161-5175.

Chapter 2 Correlation of CdS Nanocrystal Formation with Elemental Sulfur Activation and Its Implication in Synthetic Development

Formation of CdS nanocrystals in the classic approach (with octadecene (ODE) as the solvent, elemental sulfur and cadmium carboxylate as the precursors) was found to be kinetically dependent on reduction of elemental sulfur by ODE, which possessed a critical temperature (~180 ^{o}C). After elemental sulfur was activated by ODE, the formation reaction of CdS followed closely. 2-tetradecylthiophene from the activation of S by ODE and fatty acids from the formation reaction of CdS were found to be the only soluble side products. The overall reaction stoichiometry further suggested that oxidation of each ODE molecule generated two molecules of H_2S, which in turn reacted with two molecules of cadmium carboxylate molecules to yield two CdS molecular units and four molecules of fatty acids. In comparison to alkanes, octadecene was found to be substantially more active as a reductant for elemental sulfur. To the best of our knowledge, this is the first example on quantitative correlation between chemical reactions and formation of high quality nanocrystals under synthetic conditions. To demonstrate the importance of such discovery, we designed two independent and simplified synthetic approaches for synthesis of CdS nanocrystals. One approach with its reaction temperature at the critical temperature of S activation (180 ^{o}C) used the same reactant composition as the classic approach but without any hot injection. The other approach performed at an ordinary laboratory temperature ($\leq$ 100 ^{o}C) and in a common organic solvent (toluene), which was achieved by addition of fatty amine as activation reagent of elemental sulfur.

2.1 Introduction

Studies on formation mechanism of nearly monodisperse colloidal nanocrystals have attracted substantial attention in the field of chemistry because of their great potential as functional materials and interesting model systems for fundamental research. [1, 2] Although formation of nanocrystals should be a typical crystallization process, there are often some chemical reactions needed to take place prior to the crystallization process. This is so because the field is actively pushing towards "greener" synthetic chemistry, [3] which often requires synthesis starts with precursors that need to be converted to reactive "monomers" for the nucleation and growth of the targeted nanocrystals. For instance, for the most studied high quality chalcogenide nanocrystals (including II-VI, IV-VI, and I-III-VI semiconductor nanocrystals), elemental sulfur, selenium and tellurium dissolved in organic solvents (such as octadecene and organophosphines) are commonly used as the chalcogenide precursors. [4, 5] These elements (S^0, Se^0 and Te^0) must be reduced into a certain form, and then they can bond with the necessary cations to form the targeted semiconductor nanocrystals. As a result, the mechanistic studies on formation of high quality semiconductor nanocrystals have been focused on two separated fronts. Along the first front, kinetics on formation of nanocrystals — especially their size and shape evolution — has been studied extensively in the past 20 years. [1, 2] On the second front, studies on the related chemical reactions and molecular mechanisms have become active recently. [6-27] Although molecular mechanism studies might be carried out with crystallization kinetics in the background, [10, 19, 21, 28] the correlation between these two fronts has not been clearly identified yet. Understanding of such correlation is not only important for establishing much needed quantitative framework for crystallization, but also shall further shed new light on development of synthetic chemistry for high quality nanocrystals as to be demonstrated in this chapter.

II-VI semiconductor nanocrystals, especially CdSe and CdS, were established as the first examples of high quality colloidal nanocrystals among all types of colloidal nanocrystals. [4, 5] As fundamental model systems, their well-defined size dependent optical properties due to quantum confinement [29] offer convenient probes for the mechanistic studies on formation of nanocrystals. Equally important, active exploration of technical applications of colloidal nanocrystals in both academic and industrial settings has been mostly centered on II-VI semiconductor nanocrystals at present.

The commonly adopted synthetic methods for high quality CdSe and CdS nanocrystals in the field are typically performed under temperatures roughly in the range between 200 and 300 ^{o}C. [5, 30, 31] Studies on the molecular reaction mechanisms for CdSe nanocrystals in both coordinating solvents [9] and non-coordinating solvents [7, 9, 11, 19, 22] have been reported extensively in the past several years. Very recent reports further indicate that formation of high quality CdSe nanocrystals using Se dissolved in organophosphines as the Se precursor was largely associated/controlled by the structure and activation of the Se-phosphine precursors. [19, 21, 22 27] These studies revealed that, in both types of media, the chemical reactions involved in formation of CdSe nanocrystals are quite different from what was originally hypothesized. Although such insights have not been incorporated into new synthetic development yet, they certainly helped us to understand the chemical complexity during formation of high quality CdSe nanocrystals. Conversely, to the best of our knowledge, molecular mechanisms for formation of high quality CdS nanocrystals has not been explored though the classic synthetic approach of high quality CdS nanocrystals was introduced into the field along with the non-coordinating solvent approach about ten years ago. [30] The different status between CdSe and CdS systems is partially because one might think that the molecular reaction mechanism for formation of CdSe and CdS

nanocrystals with similar precursors in a similar solvent system, such as the common non-coordinating solvent — octadecene (ODE), would be similar. The results to be described below shall actually reveal that this was not the case.

In this chapter, we chose CdS nanocrystals as the main model system to explore the correlation between formation of the nanocrystals and the key chemical reaction (or, the rate-determining reaction step). The chemical reactions involved and formation of nanocrystals shall both be explored quantitatively or semi-quantitatively for clarification of the correlation. The results described below shall reveal that the reduction of elemental sulfur by ODE, instead of nucleation of the nanocrystals, was likely the rate-limiting step for synthesis of high quality CdS nanocrystals. To verify this conclusion, a non-injection synthetic approach was designed and examined, which yielded CdS nanocrystals with similar quality. Furthermore, by activating elemental sulfur with fatty amines, formation of good quality CdS nanocrystals at much reduced reaction temperature, ~100 ^{o}C in comparison to ~250 ^{o}C in the classic approach, using a common organic solvent (toluene) was achieved. Success on growth of good quality CdS nanocrystals using typical laboratory temperatures and solvents not only further confirms the determining role of activation of the S precursor on formation of CdS nanocrystals, but also paves way for removing the high temperature requirement and exotic solvents in high quality colloidal nanocrystals synthesis.

2.2 Experimental

Materials. Cadmium oxide (CdO, Alfa), oleic acid (Aldrich), octanoic acid (Alfa), Sulfur (Alfa), lead (II) acetate (Alfa), silver nitrate (Alfa), zinc acetate (Alfa), octylamine (Alfa), tetradecane

(Alfa), 1-Octadecene (ODE, 90%, Alfa), 1-Octadecene (≥99.5%, Fluka), nitric acid (HNO_3, Zhejiang Zhongxing Chemical Reagent Co), 1-(4-Nitrophenyl)-3-(4-phenylazophenyl) triazene (Cadion, Aladdin), triton X-100 (Alfa), cadmium acetate dihydrate (Alfa), butylamine (Alfa), potassium hydroxide (KOH, Tianjin Damao Chemical Reagent Factory), chloroform (Alfa), acetone (EM Science), toluene (EM Science), D-chloroform (Alfa), methanol, ethanol, hexanes (National Pharmaceutical Group Chemical Reagent Co) were used without further purification. All the cadmium fatty acid salts were prepared by the methods developed in our group.

Sythesis of CdS nanocrystal was based on the literature. [30] For a typical synthesis (reactions shown in Figure 2-2), 0.0128 g cadmium oxide (0.10 mmol), 0.3390 g oleic acid (1.20 mmol) and 3.6 g ODE (90%) was heated to 300 ^{o}C under Ar protection until clear solution was formed, cooled down to designated temperature in Ar atmosphere, then 0.0016 g S (0.05 mmol) dissolved in 0.4 g ODE (90%) was injected. After the injection of sulfur precursor, small aliquots were taken out at different time, diluted in the toluene solution and measured by UV-Vis.

The cadmium precursor conversion ratio (Cd yield) in Figure 2-2 D was determined by a two-stage extraction technique. In the first stage, final products (0.5 ml) were mixed with 0.5 ml hexanes and 1 ml methanol at 50 ^{o}C to form two phases. The upper phase of this extraction system (non-polar phase) was kept. In the second stage, extraction was repeated three times. In each extraction step, the volume of remaining solution from the previous extraction step was increased to 1 ml by adding more hexanes, then, 20 μL butylamine and 1 ml methanol were added to form two phases at 50 ^{o}C. Kept the upper solution and repeated this procedure three times to complete the second stage extraction. FTIR spectra were applied to monitor the removal of Cd fatty acid salts (see Figure 2-1 as examples) and UV-Vis was employed to ensure the separation of CdS nanocrystals in the upper solution in each extraction step. To the final

heaxnes-ODE solution, acetone was added and the turbid mixture was centrifugated at 4000 RPM for 15 minutes. The supernatant was decanted and 30 drops of concentrated nitric acid was added into the precipitate. The mixture was slowly heated to 300 ^{o}C to completely dissolve the sample and evaporate the remaining nitric acid. Subsequently, 20 drops of nitric acid was added and heated to 100 ^{o}C for 5 minutes, and DI-water was added to make a 25 ml solution. The cadmium concentration in each solution was identified by comparing to the calibration curve. [32] The Cadion solution was prepared by dissolving 0.02 g Cadion into 100 ml 0.2 M KOH ethanol solution, forming a 0.2 g/l Cadion stock solution. 2 ml 0.2 g/l Cadion stock solution, 2 ml 10 wt% Triton X-100 water solution, and a known amount of cadmium acetate water solution (or the nitric acid treated sample solution, see Experimental for preparation of such a sample solution) was mixed together and adjusted the volume to 25 ml as the "measurement solution". The "Cadion blank" spectrum (Figure 2-1 C) was taken using DI-water as the reference, with absorbance difference between 478 and 567 nm calculated as $A_1 = A_{478} - A_{567}$. The UV-Vis spectrum for each "measurement solution" (either in the calibration series or from a given sample series) was measured using "Cadion blank" as the reference, and the absorbance difference between 478 and 567 nm for each "measurement solution" spectrum was calculated as $A_2 = A_{478} - A_{567}$. To obtain A_0 for each "measurement solution" needed for either the calibration curve or the determination of Cd concentration for a sample, A_0 was calculated as the sum of A_1 from the common "Cadion blank" spectrum and A_2 for the corresponding "measurement solution" ($A_0 = A_1 + A_2$). More details are included in the caption of Figure 2-1.

Detection of H_2S gas in Figure 2-2 E was followed by heating elemental sulfur and 1-Octadecene without cadmium precursor under Ar protection, and the gas was collected with lead acetate paper by purging through Ar. The lead acetate paper strips were collected together and

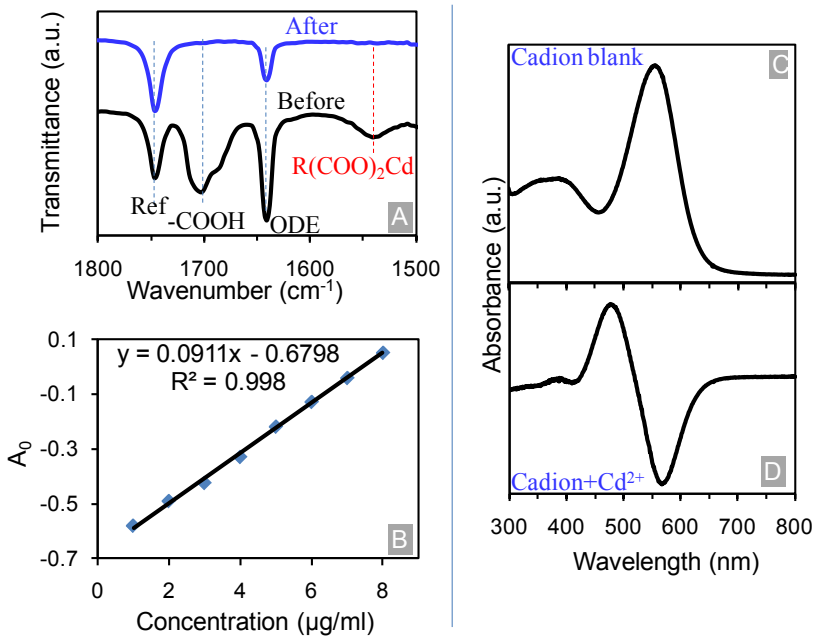

Figure 2-1. (A): FTIR spectra of the reaction solutions before and after purification process. A fixed amount of methyl-stearate ester was added as reference (the carbonyl vibration is marked as "Ref" in the plot) to a fixed volume of the nanocrystals solutions (0.5 ml) before and after the two-stage extraction. The solutions with the reference dissolved in were casted onto a CdF_2 IR substrate for measurements. Complete removal of the Cd fatty acid salt and free fatty acid was evidenced. (B): Calibration curve for determination of the cadmium concentration using the Cadion colorimetric method. (C) and (D): UV-Vis absorption spectra of the standard Cadion solution and a cadmium sample mixed with Cadion solution.

taken a digital picture in the same shot to ensure reliable grayscale values measured in Adobe Photoshop.

For the non-injection synthesis protocol, 0.0674 g cadmium oleate (0.10 mmol), 0.2825 g oleic acid (1.00 mmol), 0.0016 g S (0.05 mmol) and 4 g ODE (90%) was added into three neck flask, bubbled with Ar for 10 minutes, then heated to 180 ^{o}C under Ar protection with heating ramp at around 15 ^{o}C/min.

In a typical low temperature synthesis, 0.0398 g cadmium octanoate (0.10 mmol) was mixed with 8 g toluene, after degassing at room temperature for 10 minutes with Ar, the solution was heated up to 100 ^{o}C under Ar protection, then 0.0008 g S (0.025 mmol) dissolved in 0.05ml octylamine was injected.

The biased precursors/ODE ratio reactions used for quantitative NMR analysis, IR measurements, GC-MS etc were carried out as following. Equal molar amount (2 mmol) of cadmium octanoate ($Cd(Oc)_2$), elemental sulfur and ODE (≥99.5%) were heated under Ar protection to designated temperature, once the solution was heated to the specified temperature, heating mantle was removed, then cooled down to room temperature in Ar atmosphere, and 20 ml chloroform was added into the flask. After stirring the final products with chloroform solution for 10 minutes, 10 ml 6 M HCl solution was injected into the flask, the gas was collected by silver nitrate solution. The black precipitate in the $AgNO_3$ solution was collected by centrifugation, washed through deionized water, dried under vacuum oven overnight. Corresponding Ag_2S weight was recorded to calculate CdS yield. The $CHCl_3$ layer in the flask was evaporated on a rotary evaporator, and then added into the D-chloroform to carry out the NMR measurement. Parallel experiments were carried out under the same reaction conditions to collect the final samples for IR characterization.

And in order to confirm that the final products from biased precursor ratio was indeed formed for routine reaction condition, following experiments were carried out for corresponding NMR

analysis in Figure 2-6: 0.0398g cadmium octanoate (0.10mmol), 0.0016 g S (0.05 mmol) and 4 g ODE (90%) was mixed in the three neck flask, bubbled with Ar for 10 minutes, then heated to 220 ^{o}C and reacted under 220 ^{o}C for 1 hour. The control experiment was carried out exactly the same just without the addition of elemental sulfur. For the quantitative analysis, first, one batch of CdS nanocrystals was prepared as following: 0.796 g (2.0 mmol) cadmium octanoate, 0.064 g (2.0mmol) S mixed together with 40 g ODE, bubbled with Ar for 10 minutes, then heated up to 200 ^{o}C under Ar protection and kept under 200 ^{o}C for 1 hour. The final products were digested for gravimetric analysis through weighing Ag_2S just as in the experimental section, with 78.7 ± 7.9% of initially added elemental sulfur converted into CdS nanocrystals. The organic products were extracted into chloroform, and then known concentration of thiophene in $CDCl_3$ was added into the organic products as the internal standard for NMR quantitative analysis. In order to avoid the possible dynamic range problem of NMR since the excess amount ODE may saturate the signal detector, limited spectrum range with only interested signal on ^{1}H NMR was recorded. Detailed setup is the same as in the experimental section except limited spectrum range selected. And ^{1}H NMR quantitative analysis found out that 5.0 ± 0.3 % of initially added elemental sulfur was transformed into 2-tetradecylthiophene. By combining the results of CdS and 2-tetradecylthiophene yield, around 13% CdS synthesized was due to the formation of 2-tetradecylthiophene.

NMR measurement. ^{1}H and ^{13}C NMR measurements were carried out on Bruker 300 and 400 MHz instrument. For quantitatively integration of ^{1}H spectra to calculate the ODE consumption, a recycle delay time of 60 s was set up to make sure that proton nuclei returned to the equilibrium Boltzmann distribution between pulses.

2-tetradecylthiophene: ^{1}H NMR (300 MHz, $CDCl_3$): δ = 7.10 [dd, ^{3}J(H,H)=5.1 Hz, ^{4}J(H,H)=1.1 Hz, 1 H, 5-H], 6.91 [dd, ^{3}J(H,H)=5.1 Hz, ^{3}J(H,H)=3.4 Hz, 1 H, 4-H], 6.77 [tdd, ^{3}J(H,H)=3.4 Hz, ^{4}J(H,H)=1.1 Hz, ^{4}J(H,H)=1.1 Hz, 1 H, 3-H], 2.81 [t, ^{3}J(H,H)=7.6 Hz, 2 H, α-CH_2].

Optical Measurements. UV-Vis spectra were taken on an HP 8453 UV-visible spectrophotometer. Photoluminescence spectra were measured using a Spex Fluorolog-3 fluorometer.

Transmission Electron Microscopy (TEM). TEM images were taken on a JEOL 100 CX electron microscope using a 100 kV accelerating voltage. CdS nanocrystal was dispersed into toluene or hexane solution, then several drops of the solution were added onto a Formvar-coated copper grid, and the grid with the nanocrystals was dried in air.

Fourier Transform Infrared Spectroscopy (FTIR). FTIR spectra were recorded on a Bruker Tensor 27 FT-IR spectrometer at room temperature by directly applying sample onto CaF_2 salt plates.

Gas chromatography-Mass Spectroscopy (GC-MS). The final products after digestion were measured by a Shimadzu QP5050A quadrupole GC/MS system interfaced with a GC-17A gas chromatography. The capillary column used was a Rtx-5 MS 30-m long X 0.25-mm i.d. X 0.25-um film thickness. (Crossbond® 5% diphenyl/95% dimethyl polysiloxane, Restek, Bellefonte, PA). Temperature program, 50-300 °C at 20 °C/min. Column flow rate, 1.3 ml/min. Split ratio, 1:1. Acquisition mass range, 50-450 Da.

2.3 Results and Discussions

Three synthetic schemes. Three distinguishable but related reaction schemes were adopted/developed in this work. In the first synthetic system, CdS nanocrystals were formed by injection of elemental sulfur dissolved in octadecene (ODE) into a hot solution of cadmium fatty acid salts in ODE at a given reaction temperature (see details in Experimental Section). This scheme was introduced into the field in 2002 [30] and will be called as—the classic synthetic approach for the sake of presentation in this chapter.

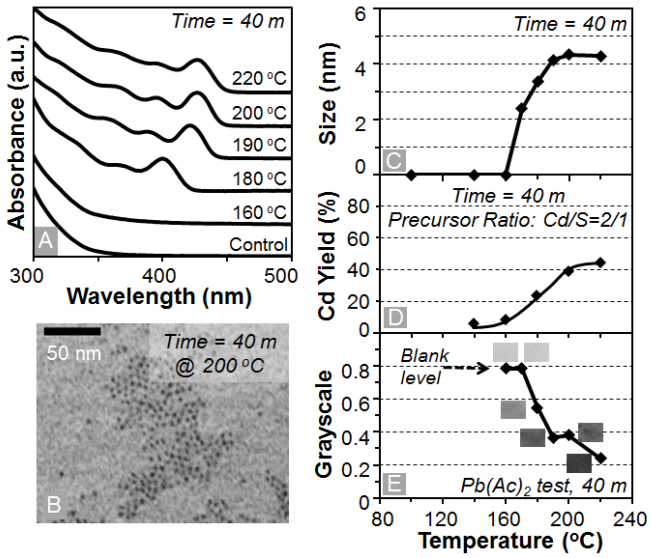

Figure 2-2. (A) Temperature dependence of formation of CdS nanocrystal, UV-Vis spectra taken at 40 minutes for each reaction. (B) TEM image of CdS nanocrystal grown under 200 °C for 40 minutes. (C) Temperature dependent particle size of CdS nanocrystals at 40 minutes. (D) Cd precursor conversion ratio (Cd yield) for the reactions at different temperatures. (E) Images and grayscale plot of lead acetate ($Pb(Ac)_2$) testing papers for H_2S detection after 40-minutes exposure to the reaction atmosphere under different temperatures (no cadmium precursor in the reaction flask).

The second reaction scheme did not involve any hot injection but with the same precursors and solvent with the classic approach, which will be called as non-injection approach in this chapter. Such a non-injection synthetic approach was formulated after identification of the rate-determining step—activation of elemental sulfur at a given temperature range—in the first system.

The third reaction system was designed to explore synthesis of CdS nanocrystals in a typical laboratory temperature (≤ 100 °C) in a regular solvent (such as toluene). This reduced temperature approach was also designed to further confirm the activation of elemental sulfur as the key chemical reaction in the formation of CdS nanocrystals by the addition of aliphatic amine which is known as a strong activation reagent for elemental sulfur.

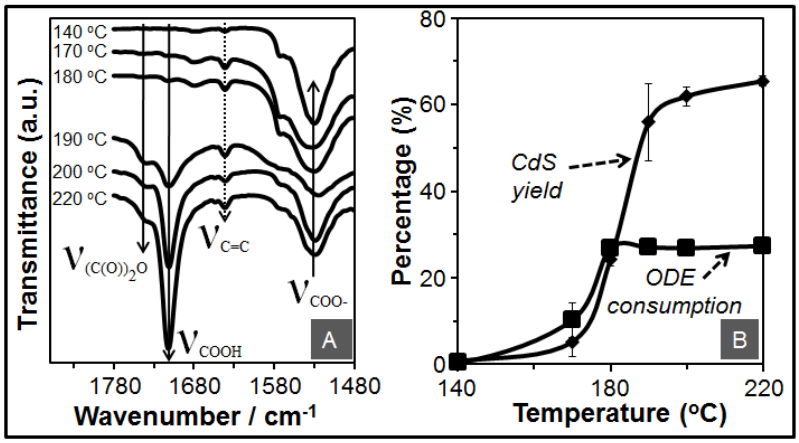

Figure 2-3. (A) Evolution of FT-IR spectra of the mixture of $Cd(Oc)_2$, ODE and elemental sulfur *at different reaction temperatures. (B) Consumption of ODE determined by NMR measurements and CdS yield measured by the conversion ratio of elemental* sulfur *for a series of reactions (initial $Cd(Oc)_2$: ODE : elemental* sulfur *=1 : 1 :1) at different reaction temperatures.*

Temperature dependence of formation of CdS nanocrystals in the classic synthetic scheme. Experiments were carried out to identify temperature effects for formation of CdS nanocrystals using the classic synthetic approach in the temperature range between about 100 °C and 220 °C. The temperatures used here was somewhat lower than that used in the original synthetic scheme (typically > 250 °C). [30] Some preliminary results reported recently by us indicated that formation of high quality CdS nanocrystals comparable to the classic approach using the same reaction system could occur at a temperature below 250 °C, [28] and the preliminary data further implied

that formation of CdS nanocrystals in this classic approach was likely controlled by a chemical kinetic process, instead of nucleation process. These preliminary results served as an initial base for us to design the experiments for this part of research.

Figure 2-2 A illustrates the UV-Vis absorption spectra of the aliquots taken from the reaction mixtures carried out at a given temperature. All reactions were performed with identical chemical composition and the only difference between these reactions was the reaction temperature (marked in Figure 2-2 A). When the aliquots were taken for recording the spectra, each reaction proceeded for 40 minutes after injection of the sulfur solution. Results clearly revealed that, for the reactions with reaction temperature below about 170 ^{o}C, the absorption spectrum of the aliquots (see the spectrum for 160 ^{o}C reaction in Figure 2-2 A) resembled that of the mixture of the starting materials (see the spectrum marked as "control" in Figure 2-2 A). This indicates that, at this relatively low temperature range, no formation of CdS nanoclusters/nanocrystals was observable by UV-Vis spectra after the reactants aged for 40 minutes.

Conversely, when the reaction temperature was above 170 ^{o}C, formation of nearly monodisperse CdS nanocrystals was observed under the same reaction conditions, which was indicated by the sharp absorption features in each spectrum (Figure 2-2 A). The quality of the nanocrystals was about the same as that obtained in the classic scheme carried out in the temperature range between 250 and 300 ^{o}C, [30] with similar sharp absorption features, nearly pure bandgap photoluminescence, and narrow size distribution with dot-shape (see a transmission electron microscope (TEM) image in Figure 2-2 B as an example).

The average size of the CdS nanocrystals in the 40-minute aliquots for each reaction was determined using the absorption peak position, [33] which showed a sharp increase by increasing the reaction temperature in the range approximately between 170 ^{o}C and 200 ^{o}C (Figure 2-2 C). The Cd conversion ratio (Figure 2-2 D) from the Cd precursor to CdS units in nanocrystals (Cd yield) determined using the so-called "Cadion" colorimetric method (see Experimental for details) showed a similar increase trend in this temperature range. A gravimetric analysis for CdS unit yield for a more concentrated reaction (Figure 2-3 and see details below) also demonstrated a similar trend seen in Figure 2-2 D.

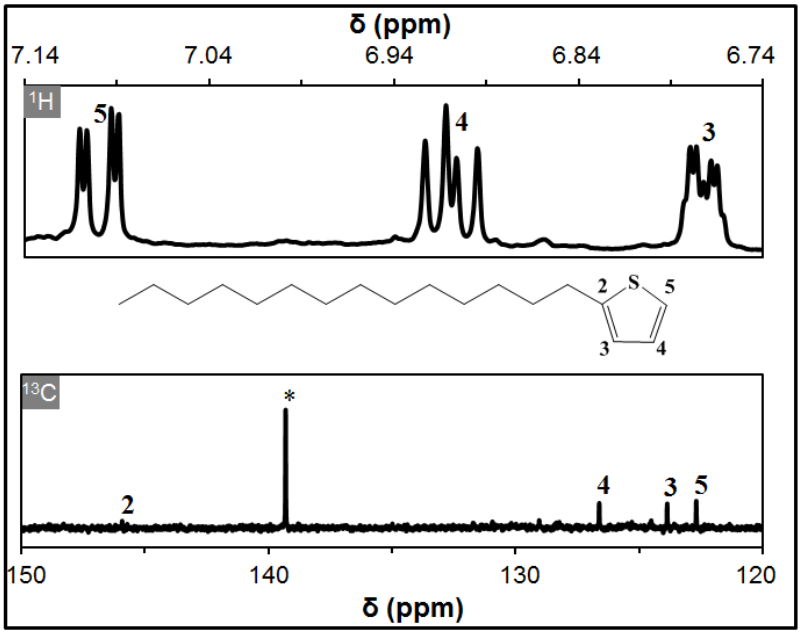

Figure 2-4. ^{1}H and ^{13}C spectra of the final products at 220 ^{o}C after HCl digestion. The peak with asterisk on ^{13}C spectrum comes from the carbon at 2 position of 1-octadecene.

These results imply that formation of CdS nanocrystals occurred rather abruptly after the system reached a critical temperature, ~180 ^{o}C. The existence of a critical temperature in Figure 2-2 C might be due to a thermally activated chemical reaction at this temperature. This is consistent with the preliminary results reported recently by us, that formation of CdS nanocrystals in the classic approach was controlled by a chemical kinetic process instead of nucleation kinetics. [28]

The Cd yield data identified under synthetic conditions (Figure 2-2 D) are important to reveal the reaction stoichiometry for formation of CdS nanocrystals. The data sets presented in Figure 2-2, specifically including Figure 2-2 D, were collected for the reaction with oleic acid as the ligands for both Cd precursor and nanocrystals (see "typical synthesis" in Experimental). The results indicate that this trend was quantitatively reproducible with either oleic acid or a saturated fatty acid as the ligands. However, the accuracy of the Cd yields measured by the cadion method largely depended on the purification of the CdS nanocrystals from the other metal-containing impurities, i.e., Cd fatty acid salts in our case. Using a new purification procedure (see

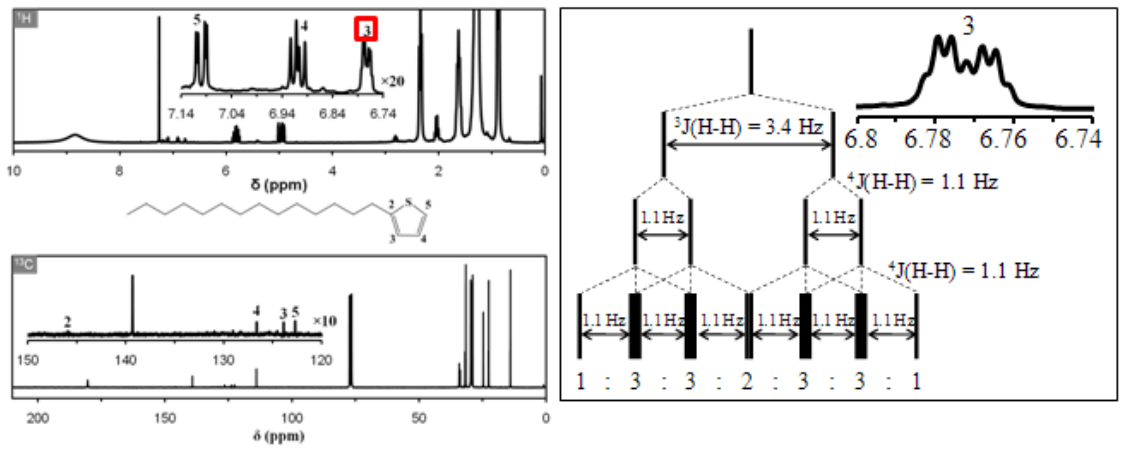

Figure 2-5. ^{1}H (left, top) and ^{13}C (left, bottom) spectra of the final products with Cd : S : ODE ratio being 1 : 1 : 1 at 220 ^{o}C after digestion by HCl acid. Enlargement and detailed coupling pattern (right) of proton at 3 position of thiophene ring. (Peak assignment: ^{1}H octanoic acid -- 8.84 carboxylic proton, 2.35 α-H, 1.63 β-H; 1-ODE -- 5.82 2-proton, 4.95 1-proton, 2.04 α-H. ^{13}C octanoic acid -- 180.5 carboxylic carbon; 1-ODE -- 139.3 2-carbon, 114.1 1-carbon. The peak at 0.07 ppm on ^{1}H and 1.0 ppm on ^{13}C spectra originated from the vacuum grease used during the synthesis.

Experimental), it was possible to remove unreacted Cd fatty acid salts quantitatively (see FTIR spectra in Figure 2-1). It should be mentioned that our results indicate that the Cd yields calculated using the extinction coefficients of CdS nanocrystals published previously [33] was only qualitatively correct, which is possibly due to two reasons, namely, the biased Cd ion concentration from unpurified Cd fatty acid salts in the measurements of the original extinction coefficients and the excess Cd ions on the surface of nanocrystals (see discussions below).

Rate-determining chemical reaction in formation of CdS nanocrystals. Experiments were performed to identify possible chemical reaction(s) that might match the critical temperature discussed in the above paragraph. Cadmium fatty acid salts alone, pure ODE, and mixtures of cadmium fatty acids salts with the corresponding fatty acids and ODE, if no elemental sulfur existed in the solution, were found to be stable in the experimental temperature range. No changes were identified by UV-Vis, FTIR, and NMR measurements. Conversely, significant changes were detected by heating up the mixture of elemental sulfur and ODE, without any cadmium precursors, in the temperature range of interest by several experimental techniques.

Figure 2-2 E shows the results of lead acetate ($Pb(Ac)_2$) tests for H_2S detection by applying $Pb(Ac)_2$ testing paper strips to the reaction atmosphere above the mixture of elemental sulfur and ODE. It reveals that the testing paper strips were colorless at low temperatures and they turned black at temperature above 170 ^oC due to the formation of black lead sulfide. The general trend of the grayscale plot of this test matched well with the trend for the formation of CdS nanocrystals when the cadmium precursors—cadmium fatty acid salts— was in place (comparing Figure 2-2 C and 2-2 D with 2-2 E). The gas phase mixture from the reactions without cadmium precursors was also bubbled into silver nitrate and zinc acetate solutions separately. The colorless silver nitrate and zinc acetate solutions became black and white

suspensions, respectively, implying the formation of black silver sulfide and white zinc sulfide. These results all indicate the generation of H_2S gas by reacting elemental sulfur with ODE.

$$S + CH_3(CH_2)_{15}CH{=}CH_2 \rightarrow H_2S + \text{side product(s)} \quad (2\text{-}1)$$

The nice correlation between the plots in the right panel of Figure 2-2 suggests that this reaction is likely the rate-determining step for the formation of CdS nanocrystals. This will be verified in the following sub-section. Furthermore, in Reaction (2-1), we did not specify the nature of side products, which will also be discussed in the following sub-section.

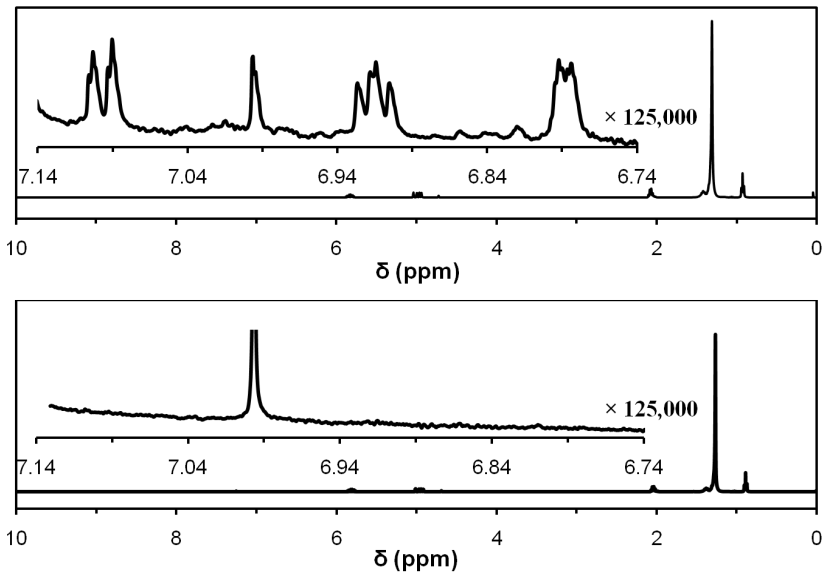

Figure 2-6. ^1H NMR spectra of the final products under synthetic conditions with (top, accumulation number: 12,000) and without (bottom, accumulation number: 8,000) the addition of elemental sulfur. See Figure 2-5 for assignment of the peaks. The sharp peak at 7.0 ppm is from ^{13}C satellite signal of trace $CHCl_3$ in $CDCl_3$ with coupling constant as 209 Hz.

Chemical reactions involved in formation of CdS nanocrystals. Results in Figure 2-2 imply that formation of CdS nanocrystals is likely initiated by the activation of elemental sulfur. To confirm this

hypothesis and identify the reaction stoichiometry, reactions with an equal molar amount of cadmium octanoate ($Cd(Oc)_2$), ODE and elemental sulfur were carried out (Figure 2-3). The results in the above sub-section indicate that ODE can react with elemental sulfur to generate H_2S gas. When a sufficient amount of cadmium fatty acid salts were in the reaction mixture, however, H_2S gas became not detectable using the same methods mentioned in the above sub-section. Instead, formation of CdS nanocrystals was observed presumably by the rapid reaction of H_2S with cadmium fatty acid salts presented in the reaction solution. If this reaction did take place, one of the side products should be fatty acid. FTIR measurements indeed revealed formation of fatty acid (Figure 2-3 A), which could not be observed without the presence of elemental sulfur as mentioned above. Furthermore, FTIR results revealed that formation of free fatty acid occurred in a similar temperature range (Figure 2-3 A) for the formation of H_2S shown in Figure 2-2 E. In addition to formation of the fatty acid, a trace amount of the corresponding anhydride was also detected by FTIR (Figure 2-3 A), [34] which presumably should be the product of dehydroxylation of the fatty acids upon prolongated heating. If ignoring the existence of this trace amount of anhydride, one can write the main reaction for formation of CdS as follows (using Cd octanoate ($Cd(Oc)_2$) as the cadmium precursor).

$$H_2S + Cd(Oc)_2 \rightarrow CdS + 2HOc \qquad (2\text{-}2)$$

In principle, if Reaction (2-2) was fast enough, formation of CdS through Reaction (2-2) should follow (2-1) closely. To further verify the correlation between Reactions (2-1) and (2-2), quantitative studies were carried out at different temperatures with an equal molar amount of $Cd(Oc)_2$, ODE and elemental sulfur, namely the ones shown in Figure 2-3. Here, Reaction (2-1) was measured by the consumption of ODE in the final products, which was determined using the α-H NMR peak of its C=C double bond. For a given final products, Reaction (2-2) was

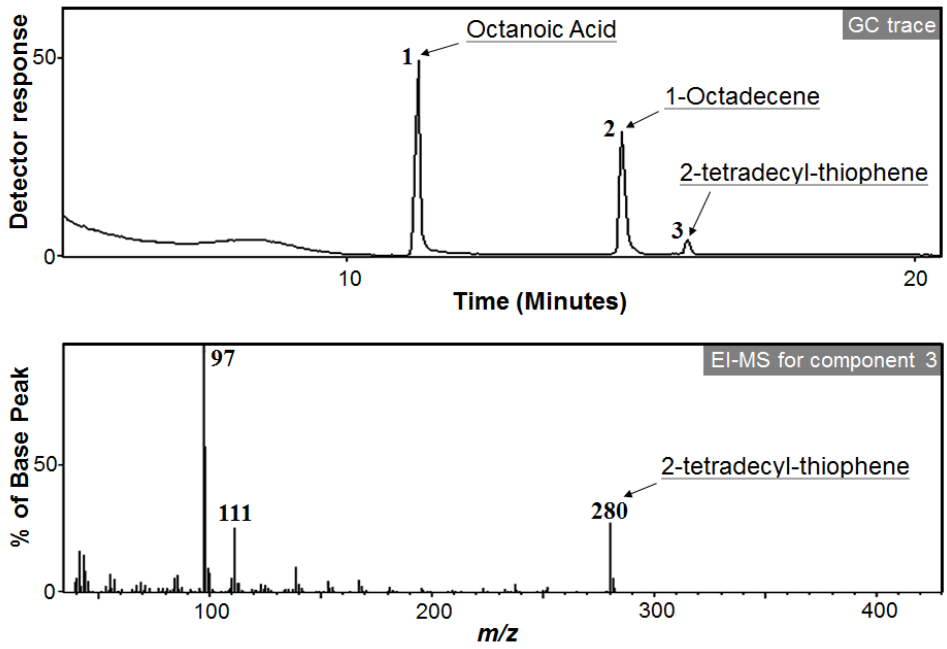

Figure 2-7. Gas chromatography (GC) of the final products after digestion by HCl and the electron ionization-mass spectrum (EI-MS) of the third component in the GC trace.

quantitatively monitored using the unit yield of CdS in solid form through gravimetric analysis (see Experimental Section for details). The quantitative results are shown in Figure 2-3 B, which firstly confirmed that the temperature dependence of both reactions were consistent with the trend shown in the right panel of Figure 2-2. Secondly, for a reaction started with $Cd(Oc)_2$: ODE : S = 1 : 1 : 1 (molar ratio), the ultimate yield of CdS units was about twice of the consumption of the ODE (see the plateau values for two curves in Figure 2-3 B) , which means that:

(Yield of CdS) : (Consumption of ODE) = 2 : 1 (2-3)

Importantly, (Yield of CdS) : (Consumption of ODE) was found to be almost the same even if the reaction was proceeded for 60 minutes at a relatively high temperature, namely 220 ^{o}C. From

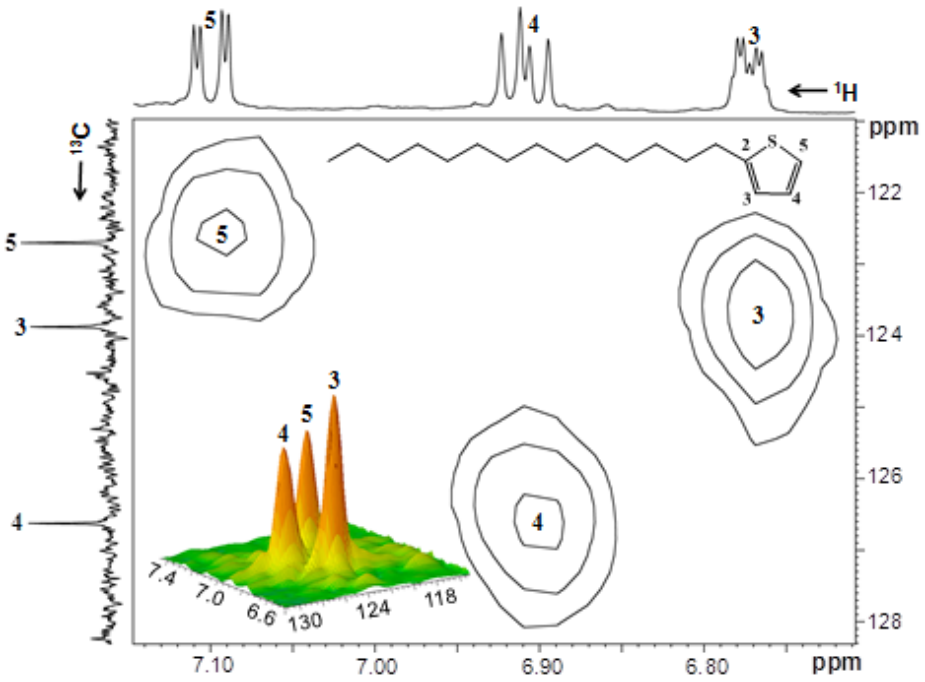

Figure 2-8. ^{1}H-^{13}C HMQC spectrum (top, full frame; bottom, enlarged) of the final product with Cd : S : ODE ratio being 1 : 1 : 1 after digestion by HCl acid.

the stoichiometry of the reaction mixture, because the ultimate consumption of ODE was about 33% (See Figure 2-3 B), one can further calculate that:

(Consumption of S) : (Consumption of ODE) = 3 : 1 (2-4)

As discussed above, both ODE consumption and CdS yield showed an ultimate value, indicated by the plateau in both curves in Figure 2-3 B. Two facts supported that the ultimate yield of CdS at relatively high temperatures in Figure 2-3 was likely due to the total consumption of elemental sulfur. Firstly, NMR measurements indicate that there was plenty of ODE left (see ^{13}C NMR in Figure 2-4 and Figure 2-5) when the reactions reached plateau in Figure 2-3 B. Secondly, given the initial equal molar amount of ODE and S, consumption of elemental sulfur was about thrice as much as that of ODE (Equation (2-4) and Figure 2-3 B).

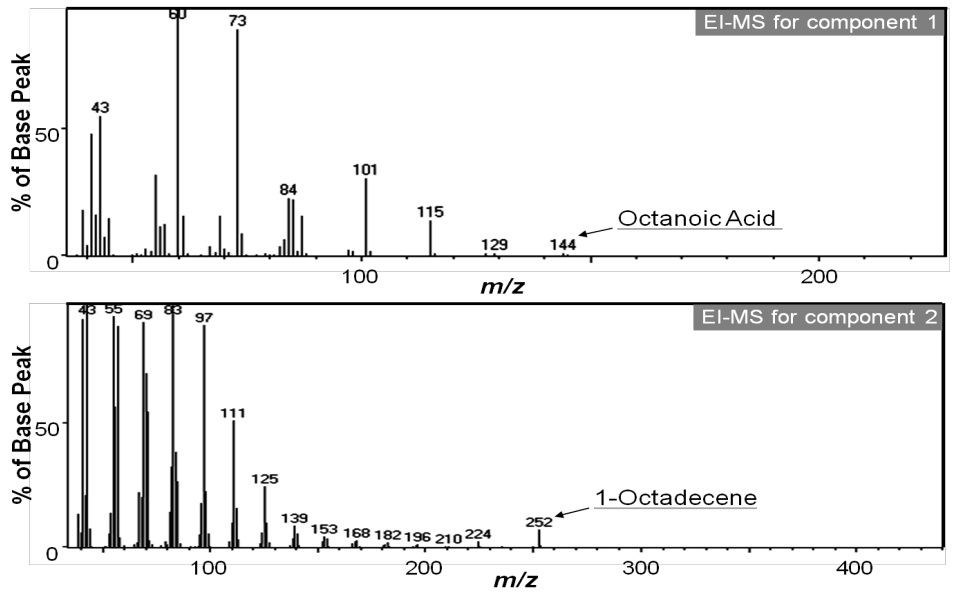

Figure 2-9. Electron ionization-mass spectra (EI-MS) of the 1st and 2nd component in the GC trace.

As ultimate yield of S in the form of CdS was only 2/3 of the initial elemental sulfur, some elemental sulfur should be consumed by formation of inactive side product(s) in Reaction (1). For the reaction with $Cd(Oc)_2$: ODE : S = 1 : 1 : 1, the final products were digested by using concentrated HCl to decompose CdS completely, and $CdCl_2$ was removed by extraction (see Experimental Section for details). The oxidation product of ODE in organic phase could be divided into two portions. The first portion was typically black in color and not soluble in common organic solvents tested, and analysis of the chemical structure was not successful. The second portion was identified as 2-tetradecylthiophene (see the molecular structure as an inset in Figure 2-4). As the thiophene molecule has an S atom, the conversion ratio of elemental sulfur could not be 100%, supporting elemental sulfur as the limiting reagents. Further quantitative analysis reveals that this oxidation product of ODE in the second portion accounted for about

~13% of total CdS yielded under a general synthesis condition (Figure 2-6 and its caption). With this result, we write the following reaction at least as a part of Reaction (2-1).

$$3S + CH_3(CH_2)_{15}CH{=}CH_2 \rightarrow 2H_2S + CH_3(CH_2)_{13}(C_4H_3S) \quad (2\text{-}5)$$

It should be emphasized that Reaction (2-5) was based on the existence of the 2-tetradecylthiophene as the only S-containing side product in the soluble portion of the organic residue. However, it is interesting to notice that, although Reaction (2-5) was established by the soluble portion of the oxidation products of ODE, it gave 3 : 1 consumption ratio between elemental sulfur and ODE. Evidently, this number is consistent with Equation (2-4), which was deduced with a different set of experimental evidences (see the text above Equation (2-4)). This led to a conclusion that the overall activation reaction of elemental sulfur by ODE, namely Reaction (2-1), should give a similar set of reaction coefficients for the reactants (ODE and S) although we could not identify the exact structure(s) of the side product(s) in the insoluble portion.

The exact structure of 2-tetradecylthiophene was identified by NMR (Figure 2-4), gas chromatography-mass spectroscopy (GC-MS, Figure 2-7), and ^{1}H-^{13}C HMQC (Heteronuclear Multiple Quantum Correlation, Figure 2-8). The final products were analyzed using GC-MS after digestion by concentrated HCl and removal of water-soluble species including all inorganic ions. The GC trace in Figure 2-7 (top) indicates that there are three organic components in the reaction mixture. The identification of the chemical composition for each component was provided by the following electron ionization-mass spectrum (EI-MS). The first and second components were determined as octanoic acid — converted from cadmium fatty acid salt through either Reaction (2-2) or the digestion process — and ODE (see their EI-MS in Figure 2-9), respectively.

The EI-MS spectrum of the third component (Figure 2-7, bottom) is consistent with tetradecylthiophene. The molecular ion peak located at 280 confirmed the existence of tetradecylthiophene.

The small peak at 281 could be assigned as result of the natural abundance of the elements. The EI-MS peaks at 111 and 97 series with 14 mass units apart for the third component could be assigned to the fragmented tetradecyl alkane chain with one CH_2 difference in mass. These results indicate that the GC-MS experiments confirmed the assignment of the

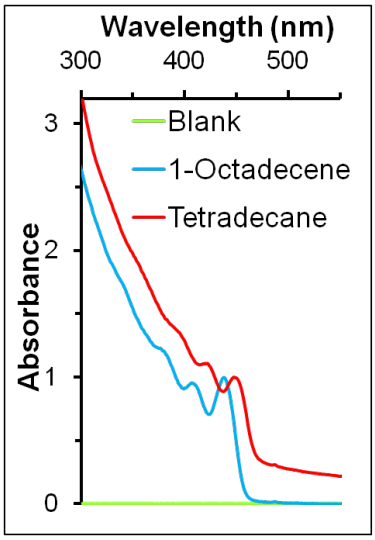

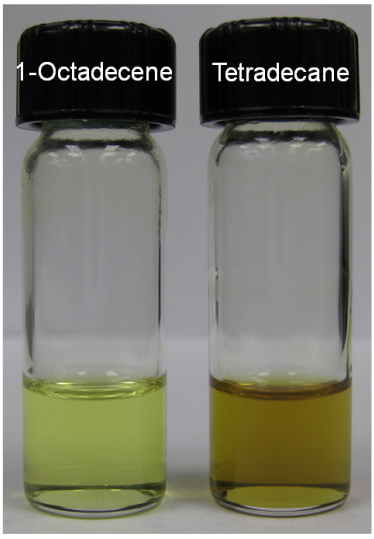

Figure 2-10. Normalized UV-Vis absorption spectra and corresponding digital pictures of CdS nanocrystals prepared in 1-Octadecene and tetradecane. Reaction condition are as following: 0.0567 g cadmium myristic acid salt (0.10 mmol), 0.2284 g myristic acid (1.0 mmol) and 3.6 g tetradecane was heated to 220 ^{o}C under Ar protection, 0.0016 g S (0.05 mmol) dissolved in 0.4 g tetradecane was injected. The synthesis of CdS in ODE was carried out in similar situation with the change of solvent to 1-ODE. And the spectrum was taken after reacting at 220 ^{o}C for 1 hour. The non-zero and tilted background for the spectrum corresponding to the synthesis in tetradecane is due to the scattering of largely sized particles which appeared to be black in the corresponding picture.

structure of tetradecylthiophene and supported the reactions involved in formation of CdS nanocrystals (Reactions (2-1), (2-2), and (2-5)). While GC-MS experiments offered molecular formula information about the molecule suspected to be tetradecylthiophene, ^{1}H-^{13}C HMQC and the analysis (Figure 2-8) indicate that its structure is consistent with the molecular structure of 2-tetradecylthiophene. Due to the electronegativity of sulfur on thiophene ring, proton at 5 position has a relatively low density of electron cloud around it compared with proton at other positions, which resulted in a higher chemical shift at 7.10 ppm. Subsequently, a reduced inductive effect could be referred to the assignments of the chemical shifts for proton located at 4 and 3 positions in the thiophene ring with chemical shift at 6.91 and 6.77 ppm, respectively. All of these assignments are in good agreement with the literature. [35, 36] Correspondingly, ^{13}C NMR (Figure 2-4, bottom panel) confirmed the existence of four different carbon environments on the thiophene ring. Due to a long relaxation time and little NOE (Nuclear Overhauser Effect) enhancement of quaternary carbon at 2 position in thiophene ring, this carbon has much lower signal intensity compared to the other three ^{13}C signals.

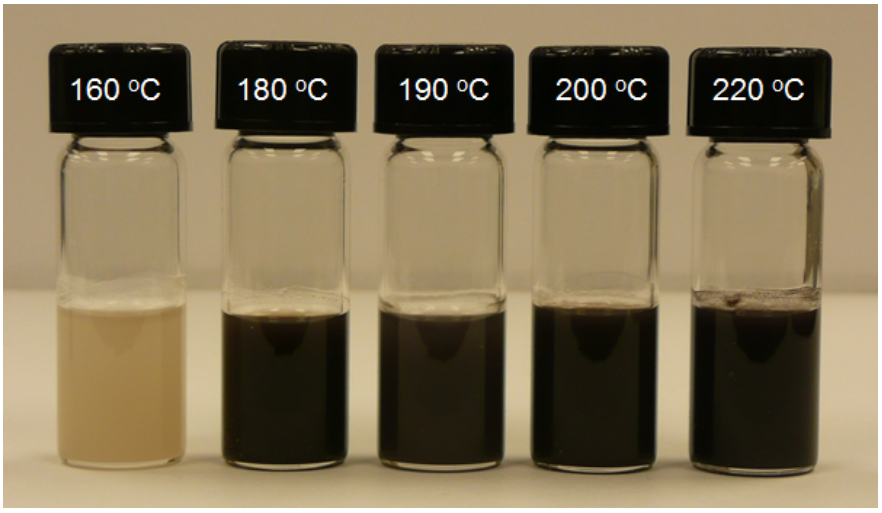

Figure 2-11. Digital picture of final products indicating temperature dependence for PbS reacted under same reaction condition except different temperature for 20 minutes.

Various characterization techniques including

NMR, FTIR and GC-MS did not show any sign of thiol, disulfide during the synthesis of CdS nanocrystals, although their counterparts were observed in the case of formation of CdSe nanocrystals using a similar reaction system. [22] Furthermore, the Se version of the identified oxidation product of S observed in this work (2-tetradecylthiophene) had not been reported for formation of CdSe nanocrystals using a similar reaction system. [9, 11, 22]

The existence of the double bond presumably made the α and β hydrogens reactive for oxidative elimination in ODE. With elemental sulfur in place, this further induced the formation of 2-tetradecylthiophene as the final oxidation product in Reaction (2-5). Non-existence of other types of S containing side products as mentioned in the above paragraph further indicate that the saturated hydrocarbon chain of octadecene could not compete with the α and β hydrogens of the double bond. It should be pointed out that, reduction of S by hydrocarbons to form thiophenes as redox products was mentioned in some books. [37-39]

However, it is well known that elemental sulfur can react with alkane under elevated temperatures to generate many types of S containing and complex products. [37-40] Therefore, in order to examine the unique properties of the double bond in ODE for activating elemental sulfur in the classic synthetic approach of CdS nanocrystals, [30] experiments were attempted to use high boiling point alkane as the solvent. The results indicate that formation of CdS nanocrystals could be achieved in such a saturated hydrocarbon solvent. However, even if the resulting CdS nanocrystals were quite small, the resulting reaction solution was brown to black in color, instead of colorless (bright yellow for large CdS nanocrystals) reaction solution obtained in ODE (Figure 2-10). Consistent with this, the typical UV-Vis spectra of the CdS nanocrystals formed in high boiling point alkane showed a significant scattering background (Figure 2-10). With these facts,

one could conclude that ODE, in comparison with saturated hydrocarbons, is a preferred reducing reagent (solvent) for elemental sulfur due to the existence of the double bond.

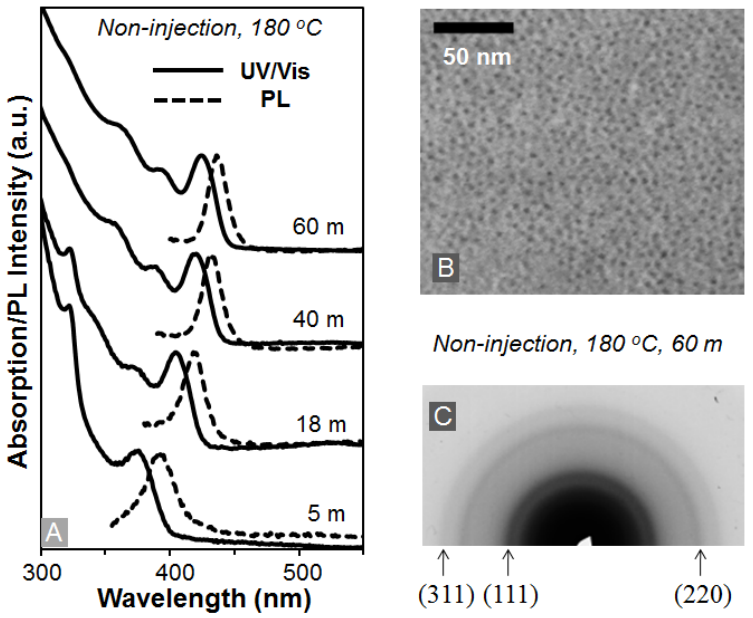

Figure 2-12. (A): Temporal evolution of UV-Vis absorption and photoluminescence of a non-injection reaction with the final reaction temperature as 180 °C. (B): TEM image of CdS nanocrystals sample of the reaction shown in (A). (C): Electron diffraction pattern of the same sample.

Preliminary results on synthesis of PbS nanocrystals using a similar reaction system (Fugre 2-11) indicates a similar correlation pattern between activation of elemental sulfur by ODE and formation of PbS nanocrystals. Similar to the CdS nanocrystals system discussed above, formation of PbS colloidal nanocrystals was found to be abruptly activated in the temperature range between 160 and 180 °C (Figure 2-11).

Consistency between the reactions in Figure 2-2 and the ones in Figure 2-3. The reactions in Figure 2-3 were performed with an equal molar amount of $Cd(Oc)_2$, ODE and elemental sulfur, which made it possible to obtain a decent amount of side products for necessary characterization discussed in the above subsection. Comparing with the reactions carried out under common synthetic conditions (the ones in Figure 2-2), the reactions in Figure 2-3 were with biased high

concentrations of $Cd(Oc)_2$ and elemental sulfur and much less ODE. However, the results and analysis below shall reveal that the chemical reactions illustrated above are consistent for both sets of reactions.

The CdS unit yield in Figure 2-3 B should be equal to the Cd yield for the given system because the resulting CdS was in the form of bulk and each CdS unit contains one Cd ion. For bulk CdS, the Cd to S ratio should be 1 to 1. Therefore, for the reactions shown in Figure 2-3, the corresponding Cd yield has an ultimate value at about 66%. Because the Cd to S precursor ratio was 2 to 1 in Figure 2-2, instead of 1 to 1 in Figure 2-3, this should give us about 33% as the ultimate Cd yield for the reactions in Figure 2-2.

The experimental value in Figure 2-2 is about 42% (Figure 2-2D). On the first sight, this value seemed to be contradictory to the value discussed in the above paragraph (33%). However,

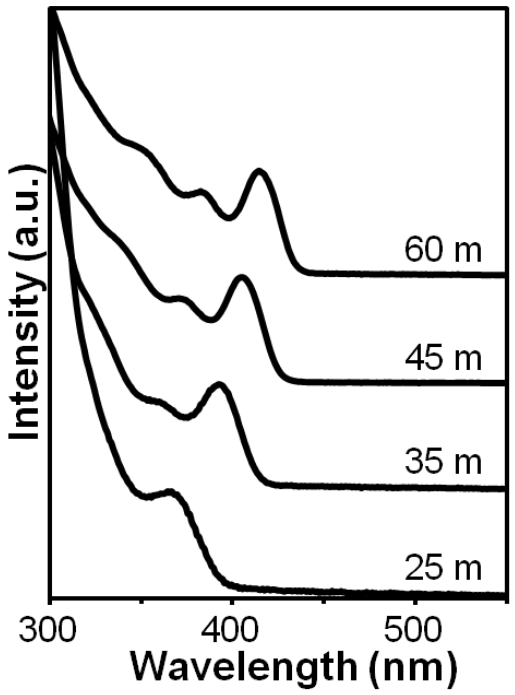

Figure 2-13. Temporal evolution of UV-Vis absorption spectra of an injection reaction carried out at 180 ^{o}C. Cadmium oxide (0.0128 g ,0.10 mmol), 0.3390 g oleic acid (1.20 mmol), and 3.6 g ODE was heated to 300 ^{o}C forming clear solution, then cooled down to 180 ^{o}C in Ar atmosphere, 0.0016 g S (0.05 mmol) dissolved in 0.4 g ODE was injected, and corresponding UV-Vis absorption spectra were recorded.

because the only ligands in the reaction system were fatty acids, the surface of the nanocrystals and the ligands were connected by RCOO-Cd bonds. Consequently, this should give CdS nanocrystals with a Cd-rich surface, which is similar to that in the case of CdSe nanocrystals solely passivated with carboxylate ligands. [41] Noticed that the size of CdS nanocrystals formed at 220 ^{o}C (Figure 2-2 A) was about 4.3 nm, one could estimate that a full monolayer of RCOO-Cd on the surface of these nanocrystals should increase the ultimate Cd yield from 33% to about 50%. This simple model obviously over estimated the amount of RCOO-Cd because the nanocrystals surface would be too crowded to accommodate a full monolayer of RCOO-Cd. With these considerations, it would be reasonable to conclude that the ultimate Cd yield based on bulk CdS (33%) and that calculated from the CdS nanocrystals (42%) are in good agreement. With the ultimate yields being consistent, we can see that the general trend in Figure 2-2 D and Figure 2B is very much similar to each other.

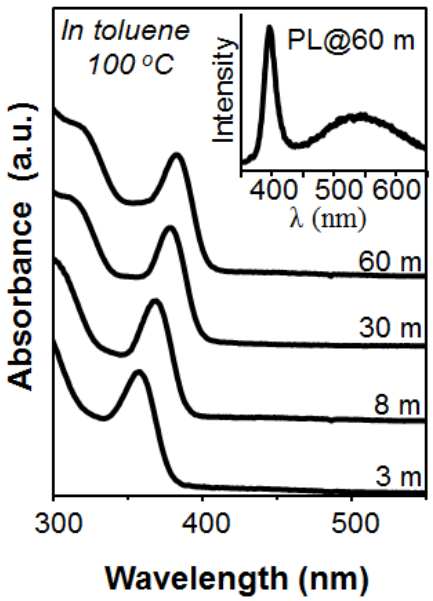

Figure 2-14. Temporal evolution of UV-Vis absorption spectra of CdS nanocrystals grown at 100 ^{o}C in toluene. Inset is the photoluminescence (PL) spectrum of the CdS aliquots taken at 60 minutes.

As for the side products identified above through the high concentration reactions in Figures 2, 3, and 4, both fatty acids (Figure 2-1) and 2-tetradecylthiophene (Figure 2-6) were identified for the reactions under the regular synthetic conditions. Specifically, 2-tetradecylthiophene was

identified as the oxidation product of S by ODE but there was no black insoluble substance observed under synthetic conditions.

Non-injection synthetic approach in ODE. The results above strongly imply that synthesis of high quality CdS nanocrystals using the classic approach [30] involved the reduction of elemental sulfur by ODE as the rate-determining step. If this was true, the rather abrupt activation of this reaction in the temperature range between around 160 and 180 ^{o}C (Figures 1 and 2) would mean that the hot-injection step in the classic protocol [30] may not be necessary. This is so because the abrupt activation at elevated temperatures should play a similar role as a rapid injection, which should be similar to the phenomenon observed very recently for the case of Co nanocrystals. [42]

The results in Figure 2-12 verified the above hypothesis. All starting materials used in a typical classic approach by hot injection, namely ODE (4 g) with 0.0674 g cadmium oleate, 0.2825 g oleic acid, and 0.0016 g S, were loaded together into the reaction flask at room temperature. The mixture was heated to 180 ^{o}C at a rate approximately 15 ^{o}C/minute. The temporal evolution of the optical properties (Figure 2-12 A) followed a similar pattern as a hot-injection reaction at the same temperature (Figure 2-13). The sharp absorption features and photoluminescence peak of the final product imply that the resulting nanocrystals are nearly monodisperse and of high optical quality. The nanocrystals were dot-shaped as confirmed by TEM (Figure 2-12 B). The electron diffraction pattern (Figure 2-12 C) indicates that the crystal structure of the resulting CdS nanocrystals was zinc-blende.

The results in Figure 2-12 firstly supported the temperature-dependent activation of elemental sulfur revealed by studying the classic approach (Figures 2-2 and 2-3). Secondly, the non-injection approach could further simplify synthesis of high quality CdS nanocrystals. It should be

mentioned that non-injection synthesis of high quality CdS nanocrystals with zinc-blende structure was reported using two different types of sulfur precursors. [43, 44] Presumably one sulfur precursor was in place for nucleation and the other for growth. In addition, the reaction temperatures used in those reports were in the range of 220 and 300 ^{o}C, which was somewhat higher than the temperature used in this chapter. Also at 240 ^{o}C, a very recent report showed that high quality CdS nanocrystals could be synthesized using non-injection approach in ODE. [45]

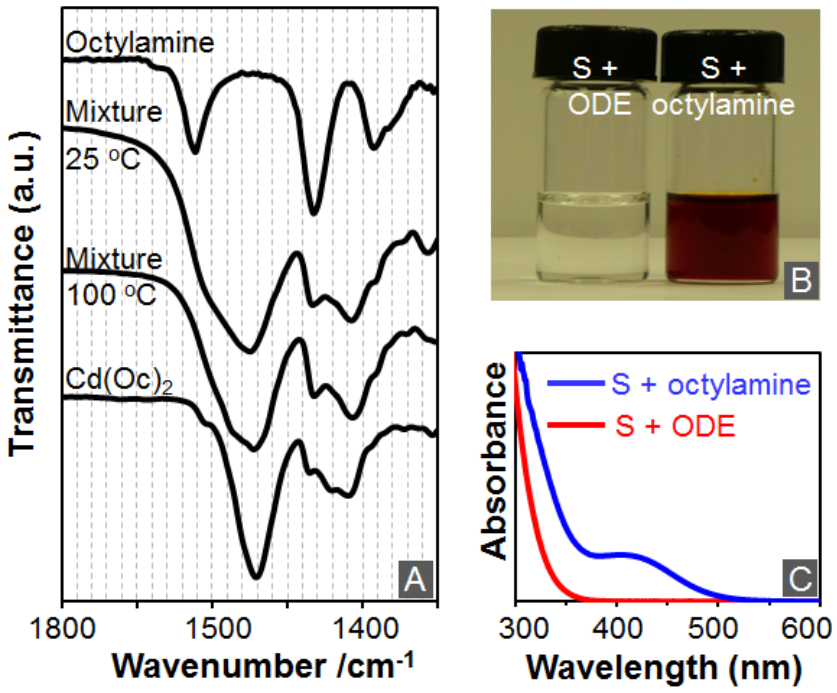

Figure 2-15. (A): FTIR spectra of pure octylamine, mixture of octylamine and cadmium octanoate ($Cd(Oc)_2$) at 25 ^{o}C, mixture of octylamine and $Cd(Oc)_2$ at 100 ^{o}C, and pure $Cd(Oc)_2$. (B): Picture of elemental sulfur in ODE and octylamine. (C) UV-Vis spectra of sulfur dissolved in ODE and octylamine.

Reduced-temperature approach in toluene. The results obtained in both classic approach and non-injection approach discussed above indicate that, as long as elemental sulfur could be activated, formation of CdS nanocrystals would follow closely. It has been established that elemental sulfur could be activated by basic chemicals such as amines, presumably by opening the S_8 ring. [40] Such an activation process

could even occur at room temperature. These facts invited us to consider synthesis of CdS nanocrystals at a temperature range reachable with common organic solvents, such as toluene, by adding amine into a reaction system.

The relatively sharp absorption spectra in Figure 2-14 illustrate that good quality CdS nanocrystals indeed formed at 100 ^{o}C by adding octylamine into the reaction system consisting of elemental sulfur, cadmium fatty acid salts, and fatty amine with toluene as the solvent (see details in Experimental Section). The temporal evolution of the UV-Vis spectra of the nanocrystals resembles a typical pattern using high temperature approaches in ODE (See Figure 2-12 A as an example). The photoluminescence spectrum of one aliquot is shown in Figure 2-14 as inset, which possesses a sharp band-edge emission with a weak deep trap emission tail to the long wavelength side (Figure 2-14, inset). The full-width-at-half-maximum (fwhm) for the band-edge emission was found to be about 22 nm, which is comparable to a typical fwhm value of PL spectra for high quality CdS nanocrystals synthesized using classic approach.

Except addition of amine, the chain length of both fatty amine and cadmium fatty acid salts were found to be important for synthesis of CdS nanocrystals in toluene. If oleylamine and cadmium stearate were used in place of octylamine and cadmium octanoate, growth of the CdS nanocrstyals was too slow to be appreciable. This was probably caused by a much reduced surface ligand dynamics on the surface of the nanocrystals at the reduced temperatures. [46] This implies that, although elemental sulfur could be activated at a common laboratory temperature, the controlled growth of high quality nanocrystals is still dependent on other parameters needed to be optimized for a successful synthetic scheme. It should be noticed that, in comparable temperature range, synthesis of CdS nanocrystals with somewhat lower optical quality was reported using relatively complex single precursors. [47, 48] Likely because of the high reactivity of

the single precursors, such as cadmium alkyl xanthates, cadmium thiocarbamates and cadmium thiocarbonates, ligands with long hydrocarbon chains were found to be effective.

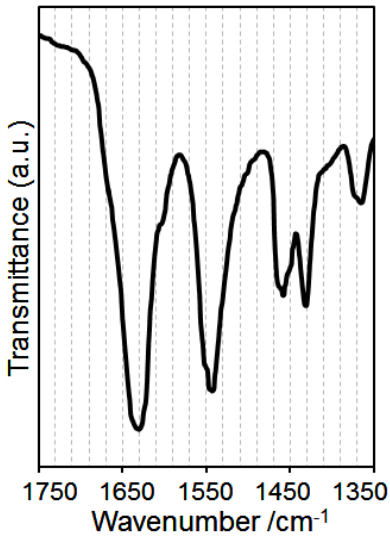

Figure 2-16. FT-IR spectra of N-butyldodecanamide.

A series of experiments were carried out to further confirm that amines were indeed activating elemental sulfur, instead of activating the cadmium fatty acid salts. It is well documented that fatty amine does react with cadmium fatty acid salts in the case of CdSe synthesis under high temperatures (usually higher than 250 ^{o}C) to form the corresponding amides. [49] However, under much reduced reaction temperature in this work (≤ 100 ^{o}C), FTIR spectra clearly revealed that no reaction occurred between fatty amine and cadmium fatty acid salts.

In Figure 2-15 A, the FTIR spectra of the mixture of octylamine and cadmium octanoate at two different temperatures, namely 25 ^{o}C and 100 ^{o}C, are presented. For the mixture at 100 ^{o}C, it was heated at this temperature in toluene (without elemental sulfur in place) for 60 minutes to ensure sufficient time for any possible reaction. Evidently, both spectra of the mixtures are the superposition of the standard spectra of octylamine (top curve) and cadmium octanoate (bottom curve). In the spectra of both mixtures, there was no sign of any amide formation (see Figure 2-16 for a standard IR spectrum of amide).

While reaction between amine and cadmium fatty acid salts in toluene did not occur, elemental sulfur easily reacted with amine. As shown in Figure 2-15 B, at room temperature, the ODE

solution of elemental sulfur is colorless but the color of elemental sulfur dissolved in octylamine is brownish red. The color difference of two mixtures yielded two distinguishable UV-Vis spectra (Figure 2-15 C). The color and absorption features in UV-Vis spectrum of the elemental sulfur and amine mixture were assigned to the formation of sulfur radicals and open chain fragments of S due to opening of S_8 ring. [50] Recently, the Ozin's group has reported a detailed account of NMR analysis of amine and elemental sulfur. [26] Our preliminary analysis of the mixture of octylamine and elemental sulfur using NMR was found to be qualitatively similar to what reported by the Ozin's group, with the formation of N'-octyl-2-thioketooctanamidine as possible activated products.

Although activation of elemental sulfur by amine involves much more complicated side products [26] than what was observed in sulfur activation solely by ODE—thiophene as the only detectable side product, generation of H_2S during the activation did occur in this case. Using the same testing method in Figure 2-2 E, lead acetate testing paper also turned black for a mixture of octylamine and elemental sulfur at 100 ^oC, while the testing paper remained white for the octylamine without sulfur in place. Furthermore, at 100 ^oC, generation of H_2S during the reaction conditions was quite rapid. As a result, prevention of H_2S from evaporation was a key parameter to determine the reproducibility of this low-temperature approach. It should be pointed out that, although the proposed reaction processes between amine and elemental sulfur were complex, H_2S also appeared as one possible product in the report by Ozin's group. [26]

It should be noted that, "greener" synthesis for CdSe [51] and ZnSe [52] nanocrystals in quantum confinement regime through hot-injection schemes usually needed the addition of fatty amine as an active ingredient. On the contrary, using similar solvents and precursors (metal fatty acid salts and elemental chalcogens), synthetic schemes for high quality CdS [30] and ZnS nanocrystals [52]

under high temperatures (usually above 250 ^{o}C) did not need the addition of amines. In fact, amines combined with high temperatures and using elemental sulfur often made the CdS and ZnS nanocrystals with poor optical performance, [53] typically with poor PL quantum yield and too large to observe quantum confinement for CdS and ZnS. The results shown here suggested that this might be a result of two related facts. One, elemental sulfur is a substantially stronger oxidant than the typical selenium precursor used, tributylphosphine-Se complex. Two, the reaction temperature used in the past for developing standard protocols for high quality II-VI semiconductor nanocrystals was high, usually in the range between 250 and 350 ^{o}C. [30, 52] As a result, if amine was in place, such high temperatures would cause elemental sulfur too reactive and result in a rapid growth of the sulfide nanocrystals with too large sizes to show any quantum confinement, although high temperature could be needed for activation of the selenium precursors.

2.4 Conclusions

In comparison to saturated hydrocarbons (alkanes), the α- and β-hydrogens in ODE were found to be sufficiently strong in a medium temperature range (~180 ^{o}C) for activation of elemental sulfur. Ultimately, there was only 2/3 of elemental sulfur could be found in the form of CdS nanocrystals, and the other 1/3 was believed to be converted into inactive organic compound, with 2-tetradecylthiophene as the only identified soluble sulfur-containing side product. The reaction stoichiometry further suggested that oxidation of each ODE molecule would generate two molecules of H_2S. As long as activation of S was in place, formation of CdS nanocrystals would follow closely. While cadmium carboxylate salts were used as the cadmium precursor, the reactions in turn yielded carboxylic acid as the side product. Identification of the close

correlation between activation of elemental sulfur and formation of CdS nanocrystals in the classic synthetic scheme enlightened us to develop a successful non-injection synthesis of high quality CdS nanocrystals at about 180 ^{o}C, using identical reactants used in a classic synthetic approach. Furthermore, by applying fatty amine as the activation reagent for elemental sulfur, we demonstrated that good quality CdS nanocrystals could be synthesized at ordinary laboratory temperatures ($\leq$ 100 ^{o}C) in common organic solvents (such as toluene). These synthetic successes not only broadened/simplified the existing protocols for metal sulfide nanocrystals, but also revealed the importance of understanding the relationship between the crystallization kinetics and the related molecular mechanisms.

2.5 References

1. Murray, C. B.; Kagan, C. R.; Bawendi, M. G. Synthesis and characterization of monodisperse nanocrystals and close-packed nanocrystal assemblies. *Annual Review of Materials Science* **2000**, *30*, 545-610.

2. Peng, X. G. An essay on synthetic chemistry of colloidal nanocrystals. *Nano Research* **2009**, *2*, 425-447.

3. Peng, X. G. Green chemical approaches toward high-quality semiconductor nanocrystals. *Chemistry-a European Journal* **2002**, *8*, 335-339.

4. Murray, C. B.; Norris, D. J.; Bawendi, M. G. Synthesis And Characterization Of Nearly Monodisperse CdE (E = S, Se, Te) Semiconductor Nanocrystallites. *Journal of the American Chemical Society* **1993**, *115*, 8706-8715.

5. Peng, Z. A.; Peng, X. G. Formation of high-quality CdTe, CdSe, and CdS nanocrystals using CdO as precursor. *Journal of the American Chemical Society* **2001**, *123*, 183-184.

6. Chen, Y. F.; Kim, M.; Lian, G.; Johnson, M. B.; Peng, X. G. Side reactions in controlling the quality, yield, and stability of high quality colloidal nanocrystals. *Journal of the American Chemical Society* **2005**, *127*, 13331-13337.

7. Deng, Z. T.; Cao, L.; Tang, F. Q.; Zou, B. S. A new route to zinc-blende CdSe nanocrystals: Mechanism and synthesis. *Journal of Physical Chemistry B* **2005**, *109*, 16671-16675.

8. Steckel, J. S.; Yen, B. K. H.; Oertel, D. C.; Bawendi, M. G. On the mechanism of lead chalcogenide nanocrystal formation. *Journal of the American Chemical Society* **2006**, *128*, 13032-13033.

9. Liu, H. T.; Owen, J. S.; Alivisatos, A. P. Mechanistic study of precursor evolution in colloidal group II-VI semiconductor nanocrystal synthesis. *Journal of the American Chemical Society* **2007**, *129*, 305-312.

10. Kwon, S. G.; Piao, Y.; Park, J.; Angappane, S.; Jo, Y.; Hwang, N.-M.; Park, J.-G.; Hyeon, T. Kinetics of monodisperse iron oxide nanocrystal formation by "heating-up" process. *Journal of the American Chemical Society* **2007**, *129*, 12571-12584.

11. Chen, O.; Chen, X.; Yang, Y. A.; Lynch, J.; Wu, H. M.; Zhuang, J. Q.; Cao, Y. C. Synthesis of Metal-Selenide Nanocrystals Using Selenium Dioxide as the Selenium Precursor. *Angewandte Chemie-International Edition* **2008**, *47*, 8638-8641.

12. Wang, F. D.; Tang, R.; Buhro, W. E. The Trouble with TOPO; Identification of Adventitious Impurities Beneficial to the Growth of Cadmium Selenide Quantum Dots, Rods, and Wires. *Nano Letters* **2008**, *8*, 3521-3524.

13. Yordanov, G. G.; Yoshimura, H.; Dushkin, C. D. Phosphine-free synthesis of metal chalcogenide quantum dots by means of in situ-generated hydrogen chalcogenides. *Colloid and Polymer Science* **2008**, *286*, 813-817.

14. Wang, F.; Tang, R.; Kao, J. L. F.; Dingman, S. D.; Buhro, W. E. Spectroscopic Identification of Tri-n-octylphosphine Oxide (TOPO) Impurities and Elucidation of Their Roles in Cadmium Selenide Quantum-Wire Growth. *Journal of the American Chemical Society* **2009**, *131*, 4983-4994.

15. Joo, J.; Pietryga, J. M.; McGuire, J. A.; Jeon, S. H.; Williams, D. J.; Wang, H. L.; Klimov, V. I. A Reduction Pathway in the Synthesis of PbSe Nanocrystal Quantum Dots. *Journal of the American Chemical Society* **2009**, *131*, 10620-10628.

16. Shen, H. B.; Wang, H. Z.; Li, X. M.; Niu, J. Z.; Wang, H.; Chen, X.; Li, L. S. Phosphine-free synthesis of high quality ZnSe, ZnSe/ZnS, and Cu-, Mn-doped ZnSe nanocrystals. *Dalton Transactions* **2009**, 10534-10540.

17. Jung, Y. K.; Kim, J. I.; Lee, J. K. Thermal Decomposition Mechanism of Single-Molecule Precursors Forming Metal Sulfide Nanoparticles. *Journal of the American Chemical Society* **2010**, *132*, 178-184.

18. Allen, P. M.; Walker, B. J.; Bawendi, M. G. Mechanistic Insights into the Formation of InP Quantum Dots. *Angewandte Chemie-International Edition* **2010**, *49*, 760-762.

19. Evans, C. M.; Evans, M. E.; Krauss, T. D. Mysteries of TOPSe Revealed: Insights into Quantum Dot Nucleation. *Journal of the American Chemical Society* **2010**, *132*, 10973-10975.

20. Cros-Gagneux, A.; Delpech, F.; Nayral, C.; Cornejo, A.; Coppel, Y.; Chaudret, B. Surface Chemistry of InP Quantum Dots: A Comprehensive Study. *Journal of the American Chemical Society* **2010**, *132*, 18147-18157.

21. Owen, J. S.; Chan, E. M.; Liu, H. T.; Alivisatos, A. P. Precursor Conversion Kinetics and the Nucleation of Cadmium Selenide Nanocrystals. *Journal of the American Chemical Society* **2010**, *132*, 18206-18213.

22. Bullen, C.; van Embden, J.; Jasieniak, J.; Cosgriff, J. E.; Mulder, R. J.; Rizzardo, E.; Gu, M.; Raston, C. L. High Activity Phosphine-Free Selenium Precursor Solution for Semiconductor Nanocrystal Growth. *Chemistry of Materials* **2010**, *22*, 4135-4143.

23. Shen, H. B.; Wang, H. Z.; Chen, X.; Niu, J. Z.; Xu, W. W.; Li, X. M.; Jiang, X. D.; Du, Z. L.; Li, L. S. Size- and Shape-Controlled Synthesis of CdTe and PbTe Nanocrystals Using Tellurium Dioxide as the Tellurium Precursor. *Chemistry of Materials* **2010**, *22*, 4756-4761.

24. Karan, N. S.; Mandal, A.; Panda, S. K.; Pradhan, N. Role of Fatty Acid in Controlling Nucleation and Growth of CdS Nanocrystals in Solution. *Journal of Physical Chemistry C* **2010**, *114*, 8873-8876.

25. Viswanatha, R.; Amenitsch, H.; Santra, S.; Sapra, S.; Datar, S. S.; Zhou, Y.; Nayak, S. K.; Kumar, S. K.; Sarma, D. D. Growth Mechanism of Cadmium Sulfide Nanocrystals. *Journal of Physical Chemistry Letters* **2010**, *1*, 304-308.

26. Thomson, J. W.; Nagashima, K.; Macdonald, P. M.; Ozin, G. A. From sulfur-amine solutions to metal sulfide nanocrystals: peering into the oleylamine-sulfur black box. *Journal of the American Chemical Society* **2011**, *133*, 5036-41.

27. Garcia-Rodriguez, R.; Liu, H. Mechanistic study of the synthesis of CdSe nanocrystals: release of selenium. *J Am Chem Soc* **2012**, *134*, 1400-3.

28. Xie, R. G.; Li, Z.; Peng, X. G. Nucleation Kinetics vs Chemical Kinetics in the Initial Formation of Semiconductor Nanocrystals. *Journal of the American Chemical Society* **2009**, *131*, 15457-15466.

29. Brus, L. E. Electron Electron And Electron-Hole Interactions In Small Semiconductor Crystallites - The Size Dependence Of The Lowest Excited Electronic State. *Journal of Chemical Physics* **1984**, *80*, 4403-4409.

30. Yu, W. W.; Peng, X. G. Formation of high-quality CdS and other II-VI semiconductor nanocrystals in noncoordinating solvents: Tunable reactivity of monomers. *Angewandte Chemie-International Edition* **2002**, *41*, 2368-2371.

31. Yang, Y. A.; Wu, H. M.; Williams, K. R.; Cao, Y. C. Synthesis of CdSe and CdTe nanocrystals without precursor injection. *Angewandte Chemie-International Edition* **2005**, *44*, 6712-6715.

32. Watanabe, H.; Ohmori, H. Dual-Wavelength Spectrophotometric Determination Of Cadmium With Cadion. *Talanta* **1979**, *26*, 959-961.

33. Yu, W. W.; Qu, L. H.; Guo, W. Z.; Peng, X. G. Experimental determination of the extinction coefficient of CdTe, CdSe, and CdS nanocrystals. *Chemistry of Materials* **2003**, *15*, 2854-2860.

34. Bellamy, L. J., *The infra-red spectra of complex molecules*. 3rd ed.; Chapman and Hall: London, 1975.

35. Wilson, P.; Lacey, D.; Sharma, S.; Worthington, B. The synthesis and characterisation of novel thienyl-pyrimidine liquid crystalline materials. *Molecular Crystals and Liquid Crystals* **2001**, *368*, 4047-4060.

36. Ellinger, S.; Kreyes, A.; Ziener, U.; Hoffmann-Richter, C.; Landfester, K.; Moller, M. Aggregation phenomena of long alpha- and alpha,omega-substituted oligothiophenes -

the effect of branched vs. linear end-groups. *European Journal of Organic Chemistry* **2007**, 5686-5702.

37. Nickless, G., *Inorganic sulphur chemistry*. Elsevier Pub. Co.: Amsterdam; New York etc., 1968.

38. Zabicky, J., *The Chemistry of alkenes. Volume 2*. Interscience Publishers: London; New York, 1970.

39. Oae, S., *Organic chemistry of sulfur*. Plenum Press: New York, 1977.

40. Cotton, F. A., *Advanced inorganic chemistry*. 6th ed.; Wiley: New York, 1999.

41. Li, Z.; Peng, X. Size/Shape-Controlled Synthesis of Colloidal CdSe Quantum Disks: Ligand and Temperature Effects. *Journal of the American Chemical Society* **2011**, *133*, 6578-6586.

42. Timonen, J. V. I.; Seppala, E. T.; Ikkala, O.; Ras, R. H. A. From Hot-Injection Synthesis to Heating-Up Synthesis of Cobalt Nanoparticles: Observation of Kinetically Controllable Nucleation. *Angewandte Chemie-International Edition* **2011**, *50*, 2080-2084.

43. Cao, Y. C.; Wang, J. H. One-pot synthesis of high-quality zinc-blende CdS nanocrystals. *Journal of the American Chemical Society* **2004**, *126*, 14336-14337.

44. Ouyang, J. Y.; Kuijper, J.; Brot, S.; Kingston, D.; Wu, X. H.; Leek, D. M.; Hu, M. Z.; Ripmeester, J. A.; Yu, K. Photoluminescent Colloidal CdS Nanocrystals with High Quality via Noninjection One-Pot Synthesis in 1-Octadecene. *Journal of Physical Chemistry C* **2009**, *113*, 7579-7593.

45. Zou, Y.; Li, D.; Yang, D. Noninjection Synthesis of CdS and Alloyed CdS(x)Se(1-x) Nanocrystals Without Nucleation Initiators. *Nanoscale Research Letters* **2010**, *5*, 966-971.

46. Pradhan, N.; Reifsnyder, D.; Xie, R. G.; Aldana, J.; Peng, X. G. Surface ligand dynamics in growth of nanocrystals. *Journal of the American Chemical Society* **2007**, *129*, 9500-9509.

47. Pradhan, N.; Efrima, S. Single-precursor, one-pot versatile synthesis under near ambient conditions of tunable, single and dual band fluorescing metal sulfide nanoparticles. *Journal of the American Chemical Society* **2003**, *125*, 2050-2051.

48. Pradhan, N.; Katz, B.; Efrima, S. Synthesis of high-quality metal sulfide nanoparticles from alkyl xanthate single precursors in alkylamine solvents. *Journal of Physical Chemistry B* **2003**, *107*, 13843-13854.

49. Ong, G. L.-P. Purification and surface studies of colloidal semiconductor nanocrystals. 2010.

50. Davis, R. E.; Nakshbendi, H. F. Sulfur In Amine Solvents. *Journal of the American Chemical Society* **1962**, *84*, 2085-&.

51. Qu, L. H.; Peng, X. G. Control of photoluminescence properties of CdSe nanocrystals in growth. *Journal of the American Chemical Society* **2002**, *124*, 2049-2055.

52. Li, L. S.; Pradhan, N.; Wang, Y. J.; Peng, X. G. High quality ZnSe and ZnS nanocrystals formed by activating zinc carboxylate precursors. *Nano Letters* **2004**, *4*, 2261-2264.

53. Joo, J.; Na, H. B.; Yu, T.; Yu, J. H.; Kim, Y. W.; Wu, F. X.; Zhang, J. Z.; Hyeon, T. Generalized and facile synthesis of semiconducting metal sulfide nanocrystals. *Journal of the American Chemical Society* **2003**, *125*, 11100-11105.

Chapter 3 Size/Shape-Controlled Synthesis of Colloidal CdSe Quantum Disks: Ligand and Temperature Effects

Size/shape-controlled colloidal CdSe quantum disks with zinc-blende (cubic) crystal structure were synthesized using air-stable and generic starting materials. The colloidal CdSe quantum disks were approximately square and their lateral dimensions were varied between 20 and 100 nm with the thickness controlled between 1 and 3 nm, which resulted in sharp and blue-shifted UV-Vis and PL peaks due to one-dimensional quantum confinement. The quantum disks were grown with either <001> or <111> direction—polar directions in the single crystalline disks—as the short axis, and both basal planes were terminated with Cd ions. These surface Cd ions were passivated with negatively-charged fatty acid ligands to neutralize the net positive charges caused by the excess monolayer of Cd ions. The coordination of the Cd ions and carboxylate groups further enabled the close-packing monolayer of fatty acid ligands on each basal plane. The close packing of the hydrocarbon chains of fatty acids dictated the up temperature limit for synthesis of the colloidal quantum disks, and the low temperature limit was found to be related to the reactivity of the starting materials. Overall, a high Cd to Se precursor ratio, negative-charged fatty acid ligands with a long hydrocarbon chain, and a proper temperature range (approximately between 140 and 250 ^{o}C) were found to be needed for successful synthesis of the colloidal CdSe quantum disks.

3.1 Introduction

Zero-dimensional [1, 2] and one-dimensional [3] colloidal semiconductor nanocrystals, respectively known as colloidal quantum dots and quantum rods, have been successfully synthesized about ten years ago with good control on size, shape, and size/shape distribution. [4-6] Their size/shape dependent properties coupled with excellent solution processability are being actively explored for applications in bio-medical labeling, [7, 8] solar cells, [9, 10] light emitting diodes, [11, 12] etc. Synthesis of colloidal two-dimensional semiconductor nanocrystals with one-dimensional quantum confinement, however, has not been well established yet. After synthesis of very thin CdSe nanoribbons was reported in 2006, [13] sheets and belts of semiconductors at least with one dimension in bulk size regime but with very small thickness showing one-dimensional quantum confinement have been reported, [14-19] but the colloidal processability/stability of those relatively large objects is usually not very good although it was mentioned that, upon sonication, nanosheets could be temporarily dispersed into organic solvents. [15] Although several examples of semiconductor nano-disks with their lateral dimensions below 100 nm have also been reported, [20-24] the optical properties of those nanodisks typically did not demonstrate one-dimensional quantum confinement. Up to present, the most inspiring results were reported by the Dubertret's group in their 2008 Communication. [25] Although the synthetic chemistry including size/shape control and characterization of the resulting nanocrystals was not well documented in the Dubertret's report, CdSe nanocrystals with strong evidences of one-dimensional quantum confinement and with their lateral sizes in the order of tens of nanometers were clearly observed, which should possess good colloidal stability. The Dubertret group's work further demonstrated that the CdSe 1D structures were in zinc-blende structure, and some interesting insights were offered on the formation of wurtzite CdSe 1D nanosheets. [15] These facts invited us to design

systematic experiments to establish reproducible and mechanism-driven synthetic schemes for size/shape controlled one-dimensional quantum confined and colloidal-stable nanostructures.

Formation mechanism of colloidal quantum rods [26, 27] and quantum dots [28, 29] has been extensively studied in the recent years, which could shed some light on designing/refining synthetic chemistry of colloidal two-dimensional semiconductor nanocrystals. Using the most studied CdSe nanocrystal system as an example, the first requirement for formation of CdSe quantum rods is the existence of a unique axis for growth. For wurtzite and zinc blende crystal structures that are common for typical II-VI and III-V semiconductors, the polar axes conveniently acted as this role. As a result, when the monomer concentration in solution was sufficiently high, one-dimensional growth (1D-growth) occurred to form quantum rods. Formation of quantum disks, on the contrary, will need to suppress the 1D-growth. One way to substantially reduce the reactivity of the polar surfaces—more accurately, reverse the reactivity of polar surface and the other surfaces of the nanocrystals—presumably is to completely passivate the polar surfaces of CdSe with complementary charges. In general, synthesis of colloidal nanocrystals relies on ligands for cations only, and thus, both basal planes of a quantum disk with its short axis being a polar axis should be terminated with cations, such as Cd ions for CdSe. As a result, the disk should possess an excess monolayer of cations and the ligands should be negatively charged, such as the commonly used deprotonated fatty acids.

The hypothesis presented in the above paragraph is some sort of "soft template" approach offered by the fatty acid ligands, which would require the surface ligands to be bonded onto the basal planes of the disks quite tightly. It was observed that, however, the surface ligands on colloidal nanocrystals could only act as "soft template" when the reaction temperature is substantially low, certainly below the boiling point of a ligand in its bulk form. [30] This is

understandable because high temperature would destroy the packing of ligands that is needed for formation of any “soft template”.

Therefore, combining the analysis of above two paragraphs, one could reason that two key parameters for synthesis of colloidal quantum disks should be an appropriate choice of ligands and a suited reaction temperature range for synthesis of quantum disks. In addition, a low monomer concentration to prevent the 1D-growth and a high Cd to Se ratio for the growth of CdSe disks should be other parameters to watch.

Experimental results to be described below confirmed that, within a defined temperature range, colloidal CdSe quantum disks with good control of both their thickness and lateral dimensions can be synthesized using generic and air-stable chemicals. The hydrocarbon chain length of the fatty acids was found to dictate the up temperature limit for the formation of quantum disks. The low temperature limit was most likely determined by the activation of elemental Se in the reaction system. Characterization of the nanocrystals verified that both top and bottom basal planes of CdSe quantum disks were polar facets with Cd ions as the out layer, and these Cd surface ions were terminated with carboxylate groups of the fatty acids used in the synthesis. The single crystalline colloidal CdSe quantum disks showed very sharp UV-Vis absorption and photoluminescence (PL) peaks due to one-dimensional quantum confinement. Experimental results strongly suggest that the resulting nanocrystals in the samples were quantum disks, instead of magic sized clusters.

3.2 Experimental

Materials. Cadmium acetate dihydrate (Alfa), stearic acid (Alfa), decanoic acid (Avocado), oleic acid (Aldrich), octanoic acid (Alfa), oleylamine (Aldrich), myristic acid (Alfa), selenium (Alfa), 1-octadecene (ODE, Alfa), tributylphosphine (TBP, Alfa), CdSe Microanalysis Compound Standards (EMS), ethanol (Pharmco), methanol (EM Science), hexanes (EM Science), chloroform (EM Science), acetone (EM Science), toluene (Mallinchrodt) were used without further purification.

Sythesis of CdSe quantum disks was carried out as following. For a typical reaction, 0.0533 g cadmium acetate dihydrate (0.20 mmol), 0.0040 g selenium (0.05 mmol), 0.0142 g stearic acid (0.05 mmol) and 4.0 g ODE was heated to designated temperature under Ar flow, small aliquots were taken out at different time intervals, diluted in toluene and measured by UV-Vis to monitor the reaction. The total amount of quantum disks from one synthesis reaction was on the milligram scale.

Examples of quantum disks with different lateral dimensions were synthesized with different chain length/concentration of fatty acid and reaction temperature. For instance, 0.0533 g cadmium acetate dihydrate (0.20 mmol), 0.0040 g selenium (0.05 mmol), 0.0057 g myristic acid (0.025 mmol) and 4.0 g ODE was heated up to 170 ^{o}C and reacted for 30 minutes, corresponding to Figure 3-4 B; 0.0533 g cadmium acetate dihydrate (0.20 mmol), 0.0040 g selenium (0.05 mmol), 0.0114 g myristic acid (0.05 mmol) and 4.0 g ODE was heated up to 170 ^{o}C and reacted for 30 minutes, corresponding to Figure 3-4 C; 0.0533 g cadmium acetate dihydrate (0.20 mmol), 0.0040 g selenium (0.05 mmol), 0.0142 g stearic acid (0.05 mmol) and 4.0 g ODE was heated up to 170 ^{o}C and reacted for 15 minutes, corresponding to Figure 3-4 D. For lower temperature synthesis, more details were provided in Figure 3-5 and the related caption.

Synthesis of CdSe quantum disks with the addition of oleylamine under low temperatures was carried out in the following way. Cadmium acetate dihydrate (0.0533 g, 0.20 mmol), 0.0040 g selenium (0.05 mmol), 0.0142 g stearic acid (0.05 mmol), 0.05 g oleylamine (0.19 mmol) and 3.95 g ODE was mixed together and then heated to 120 ^{o}C under Ar protection. Small aliquots were taken out at different time intervals, and diluted in toluene and measured by UV-Vis to monitor the reaction.

The PL QY of CdSe quantum disks were measured by comparing fluorescence intensity of coumarin 460 in ethanol [31] with CdSe quantum disks in toluene, with the same absorbance value at excitation wavelength (333 nm) and similar fluorescence wavelength.

Purification of CdSe quantum disks for different measurements. Purification of CdSe quantum disks was generally carried out by following procedure: TBP and EtOH mixture (10% volume ratio of TBP) was added into the final products, sonicated, then centrifugated at 14,000 RPM for 15 minutes, precipitate was preserved, and repeated for another 2 times. The purified samples were dissolved into toluene or hexanes forming clear solution.

Purification of CdSe quantum disks for XRD characterization was the same as the aforementioned procedure except that: centrifugation was carried out at 3,000 RPM for 15 minutes, and EtOH was used to wash the precipitate one more time, the final precipitate was preserved and dried in vacuum oven overnight before grinding in mortar for XRD analysis.

Purification of CdSe quantum disks for EDX analysis was carried out by the general procedure except following difference: all the centrifugation was carried out at 14,000 RPM for 5 minutes. The samples were first centrifugated to separate quantum disks from the solvent, supernatant decanted. And EtOH was applied to wash the samples for another three times. Final products were dried in vacuum oven overnight before applied to the conducting tape for EDX analysis.

Purification of CdSe quantum disks for FT-IR analysis was carried out by following procedure: the samples were centrifugated at 14,000 RPM for 15 minutes to separate quantum disks from the solvent, supernatant decanted. Precipitate was dissolved into hexanes, methanol was added into the solution, and analog vortex mixer was used to enhance extraction efficiency. The solution was set aside until forming separated layers, hexanes layer was carefully separately from methanol layer, and the hexanes layer was centrifugated at 14,000 RPM for 15 minutes. Then supernatant was decanted and the precipitate was dissolved into hexanes.

Optical Measurements. UV-vis spectra were taken on an HP 8453 UV-visible spectrophotometer. Photoluminescence spectra were measured using a Spex Fluorolog-3 fluorometer.

Transmission Electron Microscopy (TEM) and High-resolution TEM (HRTEM). TEM images were taken on a JEOL X-100 electron microscope using a 100 kV accelerating voltage. High resolution TEM images were taken on Fei Titan 80-300 microscope with an accerlating voltage of 300 kV. Purified CdSe quantum disks were dispersed into toluene or hexanes solution, then several drops of the solution were added onto a Formvar-coated or carbon film copper grid, and the grid with the nanocrystals was dried in air.

Fourier Transform Infrared Spectroscopy (FTIR). FTIR spectra were recorded on a Bruker Tensor 27 FT-IR spectrometer at room temperature by directly applying sample onto a KBr salt plate.

X-ray powder diffraction (XRD) patterns were acquired using Philips PW1830 X-ray diffractometer operating at 45kV/40mA and Rigaku MiniFlex X-ray diffractometer operating at 30kV/15mA.

Energy-dispersive X-ray spectroscopy (EDX) was used for elemental analysis using a Philips ESEM XL30 scanning electron microscope equipped with a field emission gun and operated at 30 kV.

X-ray photoelectron spectroscopy (XPS). XPS spectra were obtained on PHI 5000 VersaProbe instrument.

3.3 Results and Discussions

The synthetic system used in this work was similar to a regular "greener" approach for the synthesis of CdSe nanocrystals using octadecene (ODE) as a non-coordinating solvent, with elemental Se as the selenium precursor and cadmium fatty acid salts as cadmium precursor. [32, 33] Fatty acids—either with the same hydrocarbon chain length or a different one with the cadmium fatty acid salts—might be added as additional ligands when needed. As pointed out above, the chain length of the fatty acids from the cadmium precursor and/or the additional ligands used was a key parameter varied during the study.

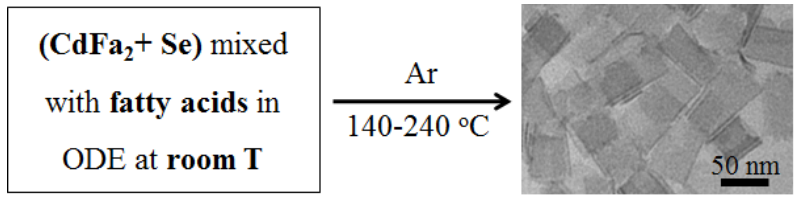

Figure 3-1. Reaction Scheme for synthesis of CdSe quantum disks. Here, $CdFa_2$ stands for cadmium fatty acid salts. The up reaction temperature limit depended on the fatty acids used in the system.

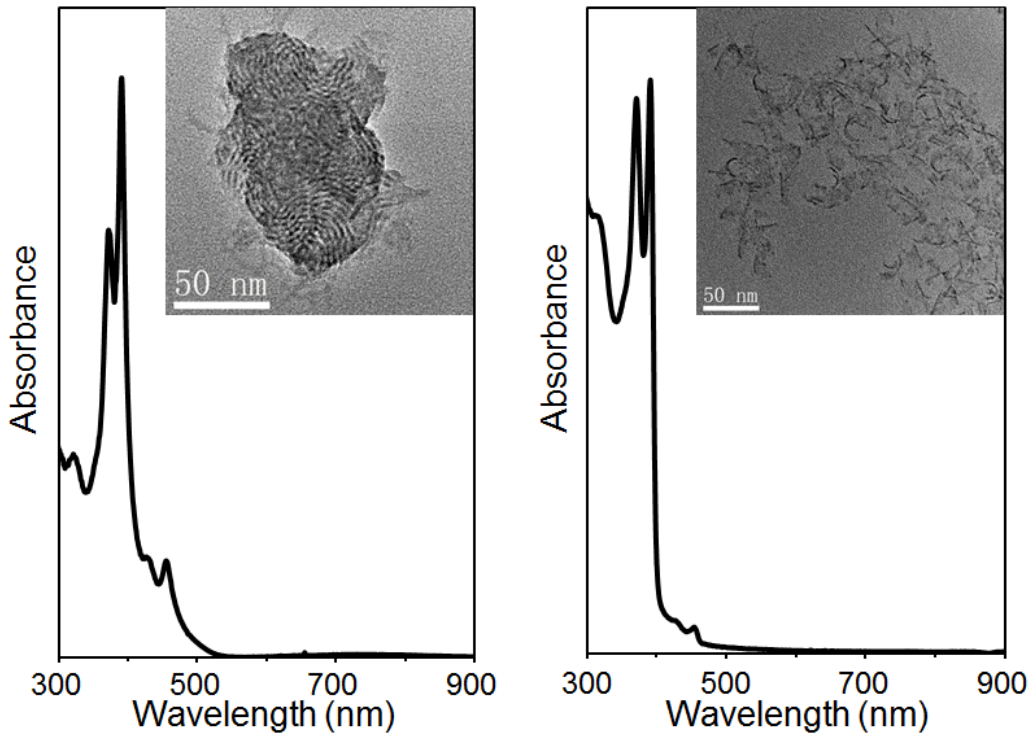

Figure 3-2. UV-Vis absorption of the CdSe 1D structures prepared without cadmium acetate and corresponding TEM image (inset). For the synthesis using cadmium octanoate (left): reaction was carried out at 150 ^{o}C for 30 minutes with 0.20 mmol cadmium octanoate, 0.05 mmol Se and 4 g ODE, UV-Vis absorption was taken after purification and background subtraction. For the synthesis using cadmium butanoate (right): at 150 ^{o}C for 30 minutes with 0.20 mmol cadmium butanoate, 0.05 mmol Se, 0.10 mmol stearic acid, and 4 g ODE. Probably because of the very thin thickness, curving of the 1D structures was observed by the TEM.

It should be pointed out that several different types of cadmium fatty acid salts, such as cadmium acetate ($CdAc_2$), cadmium butanoate ($CdBu_2$), and cadmium octanoate ($CdOc_2$) were examined. Under proper conditions, all of these cadmium fatty acid salts yielded CdSe quantum disks. Furthermore, the cadmium fatty acid salts such as $CdBu_2$, $CdOc_2$, and additional corresponding

fatty acid ligands also led to the formation of 1D confined nanostructures (See Figure 3-2). Due to ready availability of cadmium acetate, we concentrated on optimization of the quantum disk synthesis using this generic cadmium precursor. Studies on using cadmium fatty acid salts with different hydrocarbon chain lengths shall be the subject of future research.

The facts mentioned in the above paragraph seemed different from what reported by the Dubertret's group. [25] They mentioned in their report that $CdAc_2$ or other types of acetates were found to be necessary for the formation of two-dimensional CdSe nanostructures.

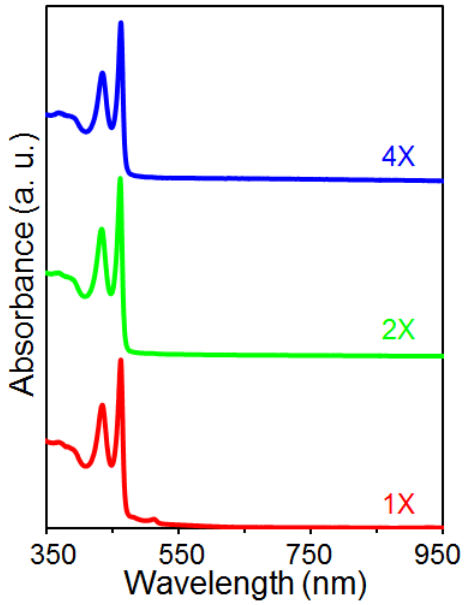

Figure 3-3. UV-Vis absorption of the CdSe quantum disks prepared with different monomer concentration. Original concentration (1X) as 0.20 mmol cadmium acetate, 0.05 mmol Se, 0.05 mmol stearic acid and 4 g ODE, together with 2 times (2X) and 4 times (4X) cadmium acetate, Se, stearic acid concentration reacted at 200 ^{o}C for 30 minutes.

It was known that, for formation of CdSe and other types of II-VI quantum rods, monomer concentrations must be sufficiently high to promote 1D-growth [26, 27, 34] and maintain the stability of the thermodynamically unstable rod shape. To study the monomer concentration effect, we varied the initial precursor concentrations in the solution. However, the results (See Figure 3-3) did not show noticeable difference within the precursor concentration range tested.

We suspected that, since the Se powder was used directly in the synthesis without any activation reagents (see Figure 3-1), the active monomer concentration in the solution at the relatively low reaction temperatures employed in this work was never sufficiently high (see detail below for activation of Se precursor). Thus, future work would be needed to clarify this effect.

It was further identified that formation of CdSe quantum disks did not require any injections. In other words, all of the reactants could be mixed at room temperature and heated to a designated reaction temperature (see Scheme in Figure 3-1). This was true for all types of cadmium fatty acid salts used. The designated reaction temperature range depended on the chain length of the fatty acids used, but generally it was between 140 ^{o}C and 250 ^{o}C. Detailed results for identification of the reaction temperature range will be discussed systematically later.

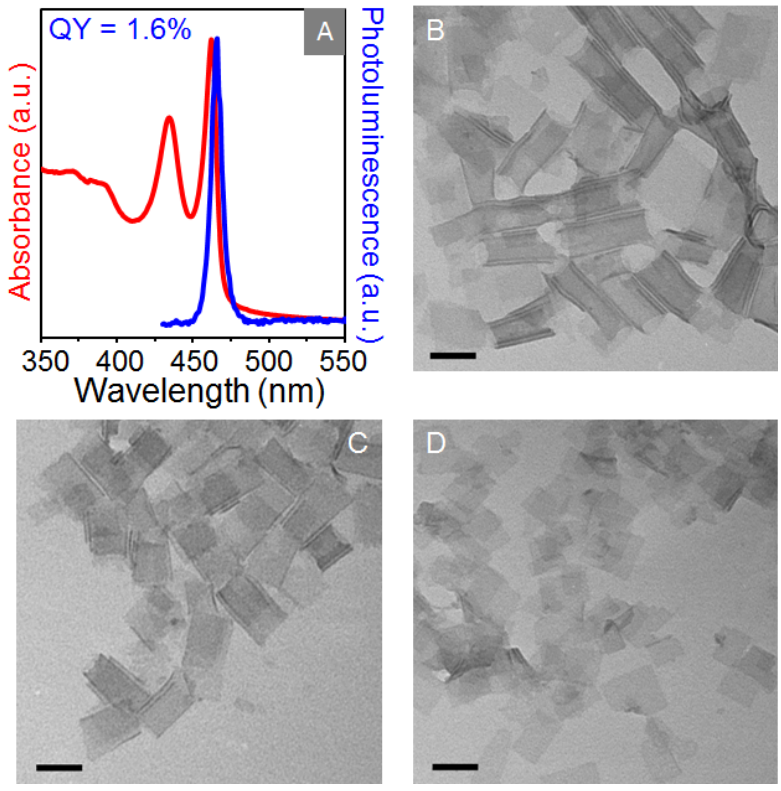

Figure 3-4. Panel A: UV-Vis(red curve) and PL (blue curve) of a typical CdSe quantum disks colloidal solution. Panel B, C, and D: TEM pictures of CdSe quantum disks with different lateral dimensions. Scale bar: 50 nm.

The one-dimensional quantum confinement of the two-dimensional quantum

disks was confirmed with UV-Vis and PL measurements. In Figure 3-4 A, a typical quantum disks sample shows a significantly blue shifted absorption band edge in comparison to that of bulk CdSe that is known to be at around 720 nm. The two sharp peaks in the UV-Vis spectra could be assigned to the excitonic absorption features of a two-dimensional CdSe nanocrystal sample with the thickness being around 2 nm. [25]

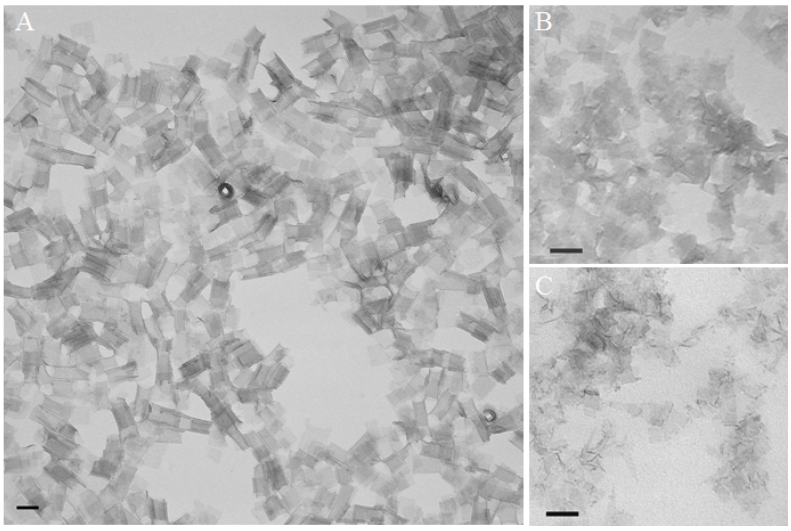

Figure 3-5. Large area TEM image of sample in Figure 3-4 C (A). Typical TEM images of CdSe quantum disks with smaller lateral size prepared at 160 ^{o}C (B) and 150 ^{o}C (C). Scale bar: 50 nm. The reaction condition for B and C are as following: 0.0533 g cadmium acetate dihydrate (0.20 mmol), 0.0040 g selenium (0.05 mmol), 0.0142 g stearic acid (0.05 mmol) and 4.0 g ODE was heated to 160 ^{o}C (B) or 150 ^{o}C (C) under Ar protection.

Similar to the sharp UV-Vis features, the PL peak of CdSe quantum disks was also sharp, with its full width at half maximum being around 0.05 eV (8 nm). For the sample shown in Figure 3-4 A, the PL quantum yield was found to be around 1.6% but generally this value was observed to be extremely sensitive to the solution composition. The PL brightness was diminished by purifying away the free fatty acid ligands in the solution, indicating a relatively weak bonding of the surface ligands as expected.

Colloidal CdSe quantum disks with their UV-Vis peaks at 392 and 512 nm—corresponding to thickness as around 1.6 and 2.2 nm [25] —were also obtained in this study although we concentrated on the ones with their UV-Vis and PL spectra shown in Figure 3-4.

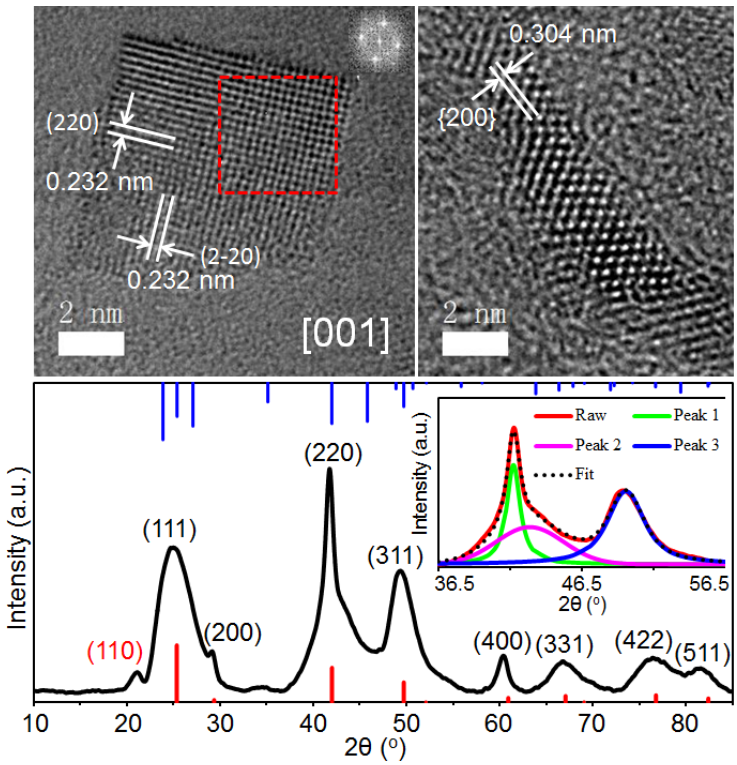

Figure 3-6. HRTEM image of a quantum disk (top left), side view of a quantum disk (top right), x-ray diffraction pattern of a quantum disk sample (bottom) and the peak fit results for (220) and (311) peaks (bottom, inset). In the x-ray diffraction pattern (bottom), the standard diffraction peaks for wurtzite (blue lines, JCPDS card no. 77-2307) and zinc blende (red lines, JCPDS card no. 88-2346) are inserted as references.

Size and shape control of the two-dimensional CdSe nanocrystals was achieved. The shape of Colloidal CdSe quantum disks was generally controlled to be square/rectangular (see representative transmission electron microscope (TEM) images in Figure 3-4). When the lateral dimensions were relatively large, the quantum disks were always found to be curved along one direction (See Figure 3-4 B and Figure 3-5 panel A as an example). On the contrary, the colloidal quantum

disks with small lateral dimensions (Figure 3-4 D) would not appear to be curved on TEM images but they intended to stack on top of each other substantially.

Thin sheets nanocrystals with their lateral dimensions above microns were found to be unstable as a colloidal solution in common solvents such as hexanes, toluene, chloroform etc. The temporary suspension in nonpolar solvents typically possessed a significant scattering tail extending into near infrared window in their UV-Vis absorption spectra. Sometimes, significant light scattering could be observed with bare eyes if the nanosheets were too large. As the emphasis of this work was colloidal stable nanocrystals with one-dimensional quantum confinement, we did not study the formation of those nanosheets in detail.

The lateral dimensions of the quantum disks could be varied in the range between 20 and 100 nm, which still possessed good colloidal stability. The lateral dimensions were found to be mostly dependent on the concentration of fatty acids, the chain length of fatty acids, and the reaction temperature. A low concentration of fatty acid ligands resulted in large lateral dimensions if other reaction conditions were the same. For example, at 170 ^{o}C and in 4 g ODE, if myristic acid concentration was 0.025 mmol, the resulting quantum disks were the largest ones in Figure 3-4 (Figure 3-4 B) , and when the ligand concentration was doubled, we obtained the quantum disks shown in Figure 3-4 C. Increasing the chain length of fatty acids had a similar effect as increasing their concentration. For instance, the small quantum disks in Figure 3-4 D were synthesized using 0.050 mmol stearic acid as the ligands under the same reactions as those for synthesizing the quantum disks in Figure 3-4 C. As for temperature effects, a low reaction temperature typically yielded quantum disks with small lateral dimensions (see Figure 3-5, Panel B and C and the related caption).

The crystal structure and single-crystal nature of the colloidal quantum disks were identified using high-resolution TEM (HRTEM) and x-ray powder diffraction (Figure 3-6). HRTEM image in Figure 3-6 confirmed that the colloidal quantum disks were mostly square in shape (top left) and the thickness (top right) was similar to what estimated from the UV-Vis peak mentioned above. The corresponding Fourier transform (FT) of the red dotted area for the top view HRTEM image (top left, Figure 3-6) confirmed the zone axis as [001] direction of zinc blende CdSe. The side view HRTEM image (Figure 3-6, top right) with a quantum disk "standing up" verified the adjacent plane distance as 0.304 nm, in good accordance with the {200} plane distance in zinc blende structure. However, the {220} plane distance shown in the top view image (Figure 3-6, top left) was around 8 % larger than bulk value. These facts imply that there should be some distortion of the disks along different directions. It should be pointed out that, although we don't have definite explanation for this lattice expansion, both lattice contraction [35, 36] and lattice expansion [37-39] of nanoparticles were reported in literature. Furthermore, as to be described below, the x-ray diffraction measurements also confirmed the lattice parameter difference between the {220} planes on the lateral direction and the short axis direction.

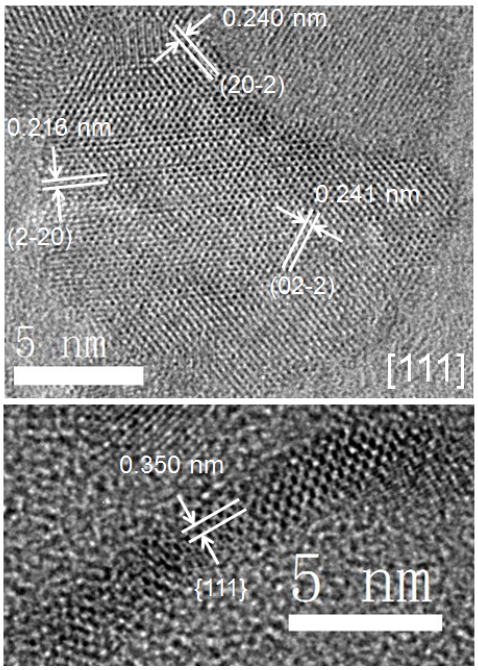

Figure 3-7. HRTEM images of CdSe quantum disks with <111> as its short axis.

Another distinguishable feature between quantum disks and quantum dots/rods is the non-uniform lattice fringes revealed by Figure 3-6, especially in the top view HRTEM image. This is

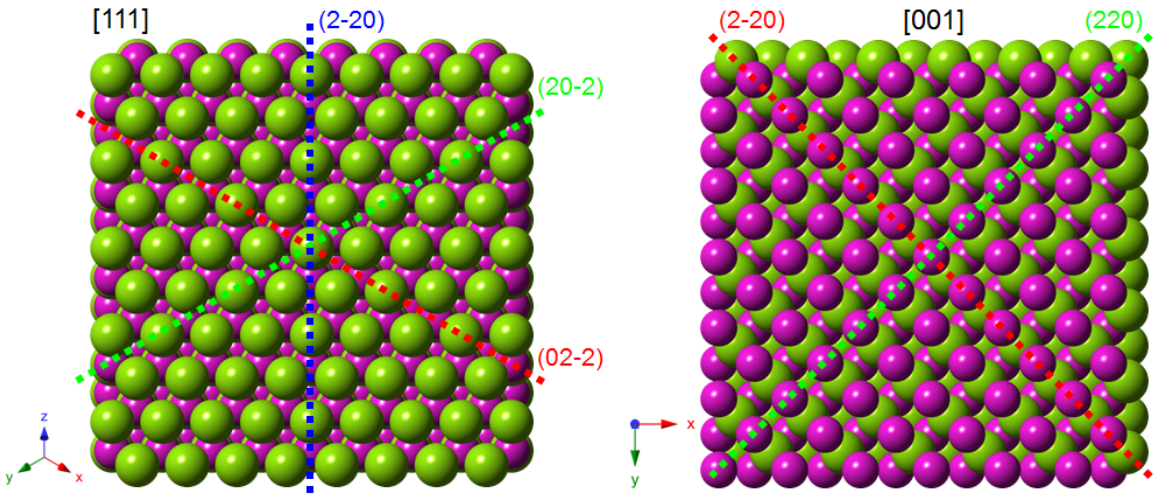

Figure 3-8. Atomic model showing the [111] (left) and [001] (right) zone axis, and corresponding {220} planes parallel to it. Cd, magenta; Se, lime green.

likely due to the combination of a very thin thickness and relatively large lateral dimensions of the quantum disks. As revealed by low resolution TEM images in Figure 3-4, such distortion would become even more significant as the edges of the quantum disks with large lateral dimensions curved along one direction (see Figure 3-4 B and the related text). As a result, HRTEM experiments with those quantum disks with relatively large lateral dimensions were found to be very difficult.

The growth directions of the CdSe quantum disks were determined mostly by x-ray diffraction with the support of HRTEM. From the HRTEM image shown in Figure 3-6 (top), one can identify that the short axis of that specific quantum disk is <001> direction. Based on broad (111) peak of XRD pattern, corroborated by surveying the quantum disks under HRTEM (see Figure 3-7), one could also identify another short axis direction as <111>. The best way to identify the

growth direction, however, is x-ray powder diffraction as demonstrated in the case of CdSe quantum rods. [3, 26, 27] This is because the width of a diffraction peak increases as the dimension of the periodic arrangement along the corresponding direction (commonly known as crystalline domain size) decreases. In principle, the domain size could be calculated quantitatively using the well-known Scherrer equation if no mechanical distortion in place.

Compared with two typical reference patterns of bulk CdSe, i.e., wurtzite and zinc blende structure, it is evident that the quantum disks are face-centered cubic F-43m structure, or zinc blende structure. This is consistent with the conclusion from HRTEM measurements as discussed above.

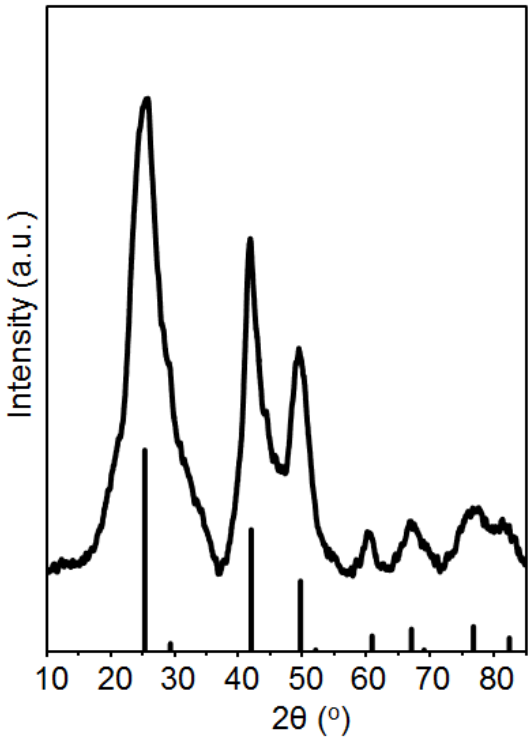

Figure 3-9. XRD pattern of CdSe quantum disks with small lateral dimensions and reference patterns of CdSe with zinc-blende (JCPDS card no. 88-2346) at the bottom. Typical TEM images are shown in Figure 3-5, panel C.

For zinc blende (cubic lattice) structure, if the short axis directions of the quantum disks were <111> and <001> axes as suggested by HRTEM experiments, <110> and <100> could be the lateral directions perpendicular to the short axis direction (Figure 3-8). Considering the specific crystal structure, (220), (200) and (400) diffraction peaks should be the three main sharp diffraction peaks. By inspecting the diffraction pattern (Figure 3-6, bottom) qualitatively,

one could indeed identify (220), (200) and (400) peaks as three unusually sharp peaks in the pattern.

Among three sharp peaks, the (200) peak overlapped with the strong (111) peak and was difficult to interpret. However, inspecting the (220) and (400) diffraction peaks carefully, each of them is most likely a superposition of one broad peak and one very narrow peak. Taking the (220) as the example, two contributions could be well separated using computer peak fit with Voigt function, [40] with a narrow "peak 1" at 41.7 and a broad "peak 2" at 42.9 degree (Figure 3-6, bottom inset). As a comparison, the neighboring (311) peak was fitted well with a single Voigt function, "peak 3".

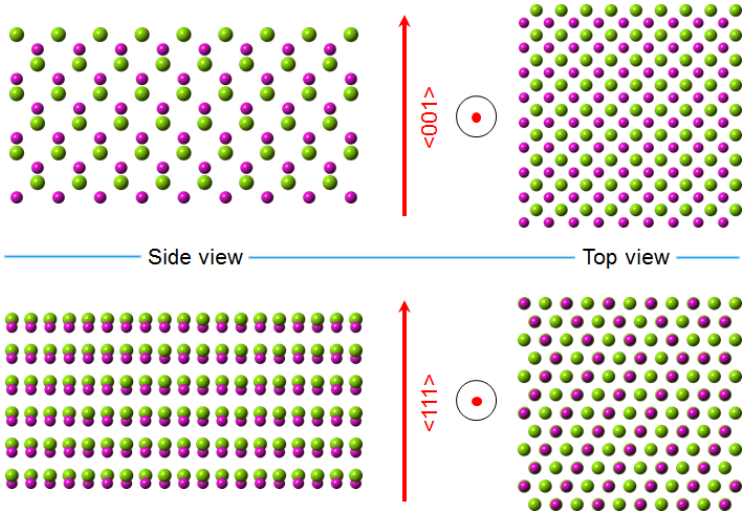

Figure 3-10. Schematic illustration of the atomic arrangement of CdSe zinc blende crystal with <001> direction (top panel) and <111> direction (bottom panel). The lime green and magenta balls represent Se and Cd ions, respectively.

A single diffraction peak with two distinguishable width values for (220) is not surprising for the colloidal CdSe quantum disks reported here. This is because, as pointed out above, the colloidal quantum disks were in zinc blende crystal structure, which is a cubic lattice and possess multiplicity of Bragg planes with the same diffraction peak. For an isotropic structure, all of these Bragg planes would overlap with each other, with the same position and same peak width. For a very thin disk, however, the

Bragg planes perpendicular to the short axis would show a much narrower (200) peak than the Bragg planes parallel to the short axis.

Overall, the entire diffraction pattern shown in figure 3-6 (bottom) matched well with the CdSe quantum disks with a mixture of <111> and <001> as their short axes (See more results in Figure 3-8). Quantitatively, the crystalline domain size along the short axis calculated from the scherrer equation was around 2.3 nm, quite close to that estimated from UV-vis peak and TEM results (see above). The lateral dimensions estimated from XRD peak width was around 12.4 nm, which seemed to be far less than the values expected (around 50 nm for this specific sample based on TEM), although they were still much larger than that of the short axis dimension. This is likely due to the distortion of the lattice as observed by HRTEM. Presumably, lattice distortion would disturb the periodicity, which thus reduced the diffraction coherence. Furthermore, for those quantum disks with curved edges (see Figure 3-4 B and 3-4 C), the crystalline domain sizes along the lateral dimensions would be reduced significantly. The appearance of the forbidden (110) peak (Figure 3-6, bottom) is also likely due to the distortion of the lattice (Figure 3-9).

The x-ray diffraction patterns showed some sign for lattice distortion directly, namely the unusual (110) peak (Figure 3-6, bottom). Based on the selection rule, the (110) peak of zinc blende CdSe should be forbidden. In order to rule out the possibility of $\lambda/2$ contamination of $(220)_{\lambda/2}$ appearing as the $(110)_{\lambda}$, [41] the same powder sample was tested on two different instruments with different X-ray source accelerating voltage, which yielded exactly the same pattern. Furthermore, the diffractometer used are coupled with scintillation counter, and thus the (110) peak of the colloidal CdSe quantum disks was unlikely an artifact. [42, 43] A reasonable hypothesis for the appearance of this forbidden (110) peak is that the curved edges of the quantum disks (Figure 3-4 B) deteriorated the group symmetry, which in turn broke the selection

Nanodisk	Cd % (molar ratio)								Mean	Theoretical value
1	59.2	61.2	60.7	59.4	59.7	59.7	59.8	60.7	60.0 ± 0.7 [a]	
2	60.1	59.0	60.1	60.3	54.8	58.9	57.1	59.0	58.7 ± 1.9	~ 54.6
3	59.7	59.0	57.9	57.5	58.1	58.0	59.2	58.3	58.5 ± 0.7	
Standard	Cd % (molar ratio)								Mean	Theoretical value
	50.5	50.2	49.9	49.9	50.0	50.1	49.8	49.6	50.0 ± 0.3	50.0

Table 3-1. EDX analysis results of CdSe standard and the purified CdSe quantum disks. a: standard deviation.

rule of the structure. To confirm this hypothesis, a quantum disk sample with smaller lateral dimensions were examined with x-ray diffraction, which indeed showed similar diffraction pattern but with barely any (110) peak (Figure 3-9).

It should be mentioned that existence of two growth directions is not in contradictory with the optical properties of the quantum disks (Figure 3-4 A). Based on the calculations, since the actual repeating equivalent atom planes are {111} and {200} along <111> and <100> direction, [44] 5 repeating {111} gave 1.754 nm compared with 1.823 nm of 6 repeating {200} and 0.069 nm difference; 6 repeating {111} gave 2.105 nm compared with 2.127 nm of 7 repeating {200} and 0.022 nm difference. Given such small difference along these two directions, broadened instead of separate excitonic peak would be observed. The thickness difference along two growth directions would be extremely small, which should not lead to the appearance of distinguishable absorption and PL peaks due to different thickness.

The basal planes of the CdSe quantum disks possess one feature in common for the CdSe quantum disks with both types of short axis orientations, either <111> or <001> direction. Along <111> (or <001>) direction, a usual packing scheme for a neutral crystal shall be polar,

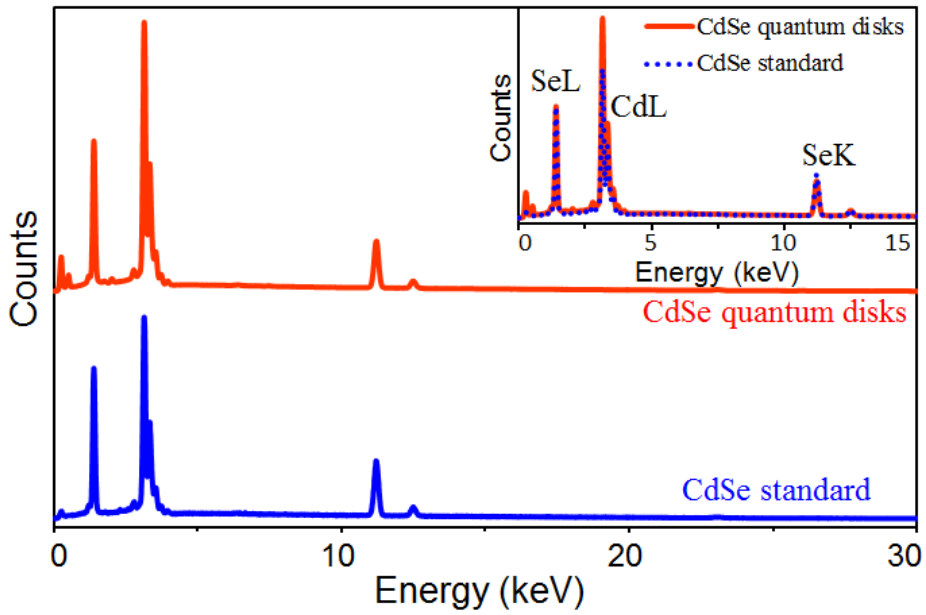

Figure 3-11. EDX spectra of the purified CdSe quantum disks averaged over 24 spectra and referenced with CdSe standard averaged over 8 spectra, with quantitative analysis results as $Cd_{0.59}Se_{0.41}$ for CdSe quantum disks and $Cd_{0.5}Se_{0.5}$ for CdSe standard. Inset: Overlaid enlarged EDX spectra and corresponding peak assignment. The peak at around 1.38, 3.14, 11.2, 12.5 keV could be assigned to Se L, Cd L, Se Kα, Se Kβ, and small peaks at around 0.26 and 0.52 keV came from the C Kα and O Kα, respectively. The carbon and oxygen signal on CdSe quantum disks was due to the residual ligands after purification, and the carbon signal of the CdSe standard was originated from the protective carbon coating on it. Besides, only trace amount of P Kα could be detected at around 2.02 keV on purified CdSe quantum disks, indicating the majority of TBP used during the purification process has been washed away.

with the dipole moment oriented exactly the same as <111> (or <001>) axis (Figure 3-10). Such dipole moment was caused by the alternating packing of Cd and Se layers along the given axis. [45, 46] This means that the basic structures of the quantum disks are consistent with what speculated

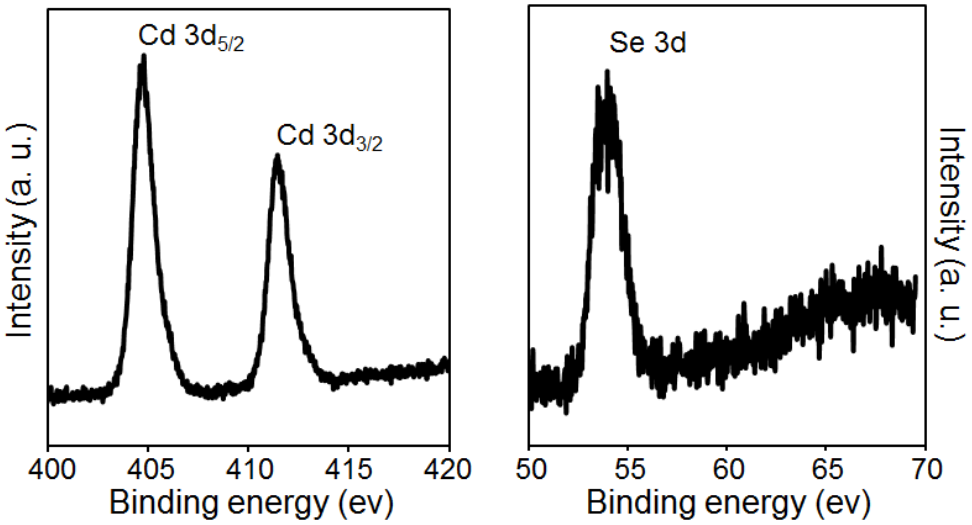

Figure 3-12. Close-up XPS survey scan for CdSe quantum disks. XPS spectra were calibrated with respect to C1s at 284.6 ev. Oxidation of Cd could be identified by the higher energy side shoulder on both $3d_{5/2}$ and $3d_{3/2}$ peak; and oxidation of Se would lead to the appearance of peak at around 59 ev. Both are absent for the spectra shown here.

in the Introduction Section: a quantum disk could be formed by stopping the 1D-growth along its polar axis in the lattice structure, which should thus turn a polar axis into the short axis of the disk.

The schematic packing patterns shown in Figure 3-10, however, reveal that only one side of the polar basal plane should be terminated with Cd for both cases if the Cd:Se ratio was 1 : 1 in the quantum disks for both cases. The other basal plane opposite to the one terminated with Cd ions should be completely terminated by Se ions in such a neutral crystal (see the side view schemes in Figure 3-10). In fact, this structural feature was believed to be the reason why II-VI semiconductor quantum rods could be controllably synthesized under significantly higher temperatures and higher monomer concentrations through the 1D-growth mode. [27]

The hypothesis mentioned in the Introduction Section, however, was to passivate both basal planes of the quantum disks with organic ligands, i.e., fatty acids. This would require the control of two basic parameters. The first one is a relatively low reaction temperature to retain the ligands bonding onto the basal planes, which will be confirmed in the next sub-section. The second requirement is to have an additional Cd ion layer grown onto the basal plane terminated with Se ions in Figure 3-10 (the top basal plane in the side view schemes, Figure 3-10), which should then enable the bonding of fatty acid ligands onto both basal planes.

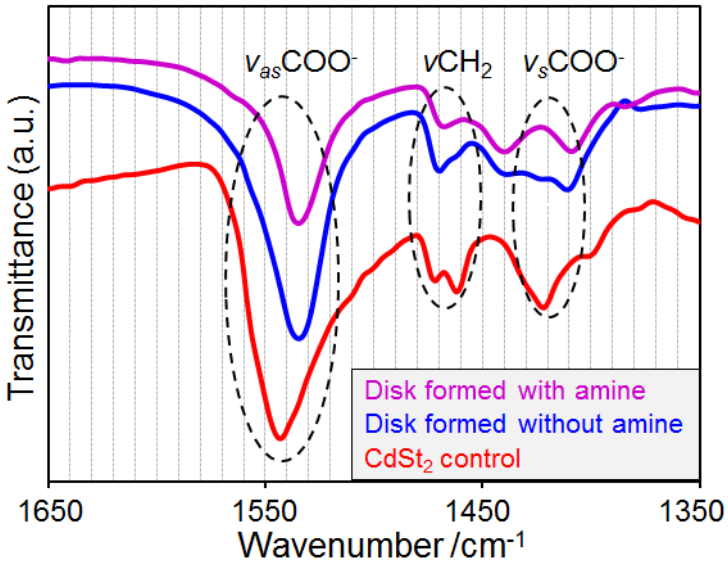

Figure 3-13. FTIR spectra of purified colloidal CdSe quantum disks formed with and without fatty amines added. For reference, the FTIR spectrum of cadmium stearate ($CdSt_2$) is also provided.

Evidently, if the second requirement discussed in the above paragraph was realized, one would find the Cd to Se ratio significantly different from 1 : 1, given that there were only a few monolayers of CdSe along the short axis directions. Energy dispersive X-ray spectroscopy (EDX) coupled with x-ray photoelectron spectroscopy (XPS) were employed to accurately identify the Cd to Se ratio in colloidal CdSe quantum disks. Three batches of carefully purified colloidal quantum disks samples were analyzed parallel with a commercial CdSe microanalysis standard (see the EDX spectra in Figure 3-11) using carefully calibrated EDX setup. [47] Quantitative

analysis of the commercial standard using the EDX protocol gave a Cd : Se ratio being 1.0 : 1.0, with an error of ± 0.3 % for 8 different measurements for the same standard. On the contrary, the Cd : Se ratio was found to be 1.0 : 0.69 for the quantum disk samples, with an error being ± 1.4 % for 24 different measurements with three different batches of colloidal quantum disks (See detailed analysis results in Table 3-1).

With the thickness of the quantum disks being around 2 nm, the number of repeating CdSe atomic layers should be approximately 5 to 6 repeating layers along the thickness direction. Simple theoretical calculation using such a model gave us a Cd : Se ratio being around 1.0 : 0.83. Considering the imperfection of the disk structures revealed by TEM studies (Figures 2 and 3) and the simplicity of the model, we considered that the theoretical value and experimental values were in a good agreement.

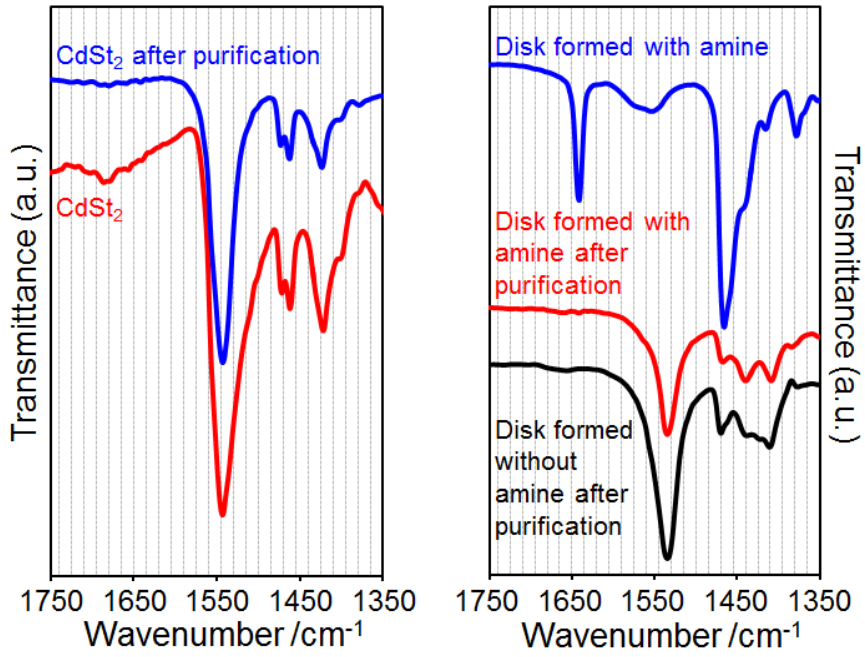

Figure 3-14. FT-IR spectra of cadmium stearate ($CdSt_2$) before and after purification as control (left), the CdSe quantum disks formed with amine before and after purification, and the CdSe quantum disks formed without amine after purification (right).

The somewhat higher Cd : Se ratio in the experimental data could be a result of the residue of starting Cd precursors or oxidation products (such as CdO) formed during synthesis and purification. Under the given synthetic conditions, the Cd ions in all of these types of Cd containing compounds should have a distinguishable chemical environment in comparison to the Cd-Se bond in the quantum disks. Most likely, those Cd ions should be bonded with oxygen. XPS measurements, however, undoubtedly confirmed that all Cd ions were bonded with Se (Figure 3-12), which excluded possible contamination of the starting materials and CdO.

A related experimental observation should be mentioned. It was found that, for the formation of good quality CdSe quantum disks, the

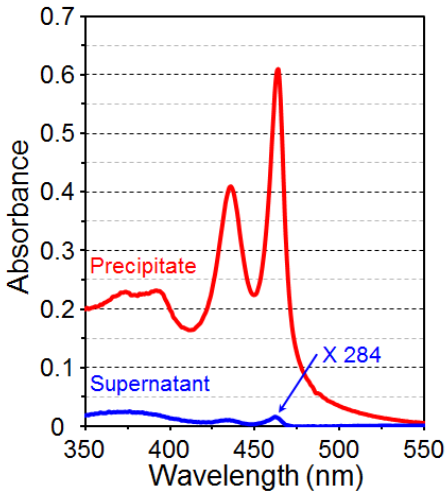

*Figure 3-15. UV-Vis absorption of the precipitate after centrifugating at 3000 RPM for 5 minutes and corresponding supernatant. The absorbance spectra were taken quantitatively: 0.005 g precipitate was diluted by 17.166 g toluene, and 0.259 g supernatant was diluted by 3.129 g toluene. Corresponding absorbance value at peak position for precipitate and supernatant is 0.61 and 0.015, based on the dilution factor, normalized absorbance value for precipitate and supernatant is 0.61/(0.005/17.166)=2094.25 and 0.015/(0.259/3.129)=0.18. This leads to the fact that (2094.25/(2094.25+0.18))*100% = 99.99% percentage of absorbance came from precipitate.*

Cd and Se precursor ratio must be substantially higher than 1 : 1 (See details in Experimental Section). Such reaction conditions are considered to be consistent with a Cd-rich product and fatty acid ligand passivation for stopping the 1D-growth along the polar axes of the nanocrystals.

The bonding nature between the ligands and the colloidal quantum disks was studied using FTIR. As shown in Figure 3-13, for the colloidal quantum disks formed either under typical reaction conditions or with the addition of fatty amines (the latter case to be discussed in detail later), the surface fatty acid ligands were in the form of negatively-charged carboxylate ($-COO^-$) as expected. Based on the peak position of the asymmetric vibration of the carboxylate group, one could conclude that the bonding between the carboxylate group and the surface cadmium ions was "bridging". [48-50]

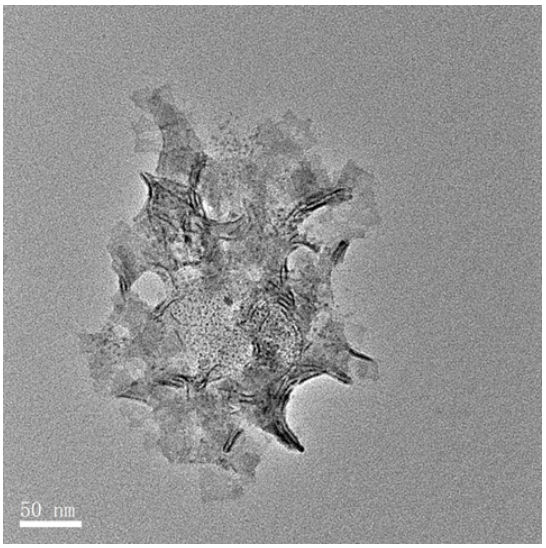

Figure 3-16. TEM image of CdSe quantum disks without purification. Black dots are visible and the disks showed significantly more serious aggregation, both of which could cause difficulty to draw a correct conclusion.

In comparison to the standard spectrum of cadmium stearate ($CdSt_2$), however, the asymmetric vibration band of $-COO^-$ group shifted noticeably to lower wavenumbers (Figure 3-13). This indicates that, in comparison to the standard bonding of free cadmium ions and deprotonated fatty acids, the carboxylate ligands bonded somewhat weaker to the surface Cd ions.

It should be pointed out that, for reaction with amine in place, the concentration of the fatty amines could be several times higher than that of fatty acids. However, after careful purification, there was no sign of fatty amines in the IR spectrum of the colloidal quantum disks samples (See Figure 3-14), although it is well-known that both amines and fatty acids are common ligands for CdSe nanocrystals. This strongly supports the hypothesis that the negatively-charged carboxylate groups from the fatty acid ligands were needed to balance the charge of the CdSe quantum disks with an excess layer of Cd on one of the basal planes.

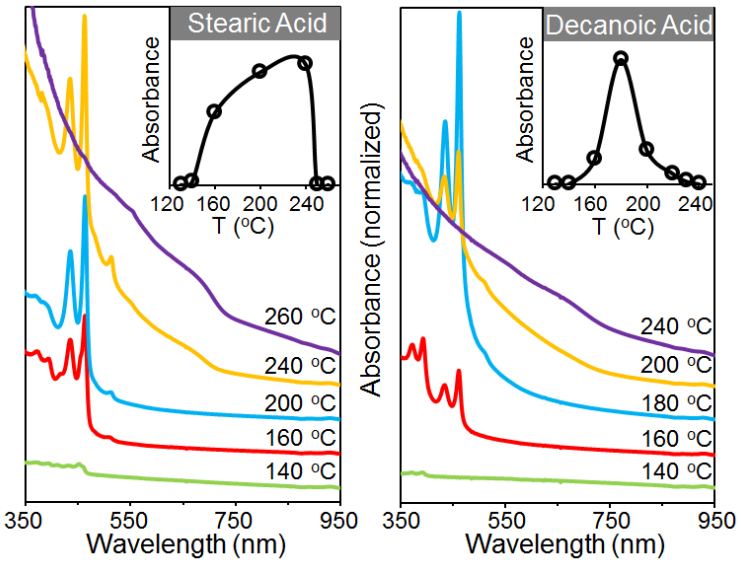

Figure 3-17. Temperature-dependent UV-Vis spectra of the nanocrystals synthesized using stearic acid (left) and decanoic acid (right). The reaction time for all cases was fixed to be 30 minutes, and the UV-Vis spectra were all normalized to the concentration. The inset in each series plots the absorbance of the first UV-Vis peak at 462 nm vs. the reaction temperature after background correction (see text for details).

Magic sized nanoclusters has been considered a possible explanation for the sharp UV-Vis and PL spectra similar to those shown in Figure 3-4 A, [51, 52] and to our understanding, the debate has not been well resolved. Based on the characterization results discussed above, magic sized nanoclusters could be excluded in our samples. For example, the x-ray diffraction patterns and the TEM images must be associated with quantum disks,

instead of those tiny magic sized nanoclusters. Especially, the x-ray powder diffraction was performed with ensemble of the products, which offers strong evidences to exclude magic sized nanoclusters. The size of the magic sized nanoclusters should be around 2 nm to yield UV-Vis and PL spectra similar to those in Figure 3-4 A. Such tiny nanoclusters should only show extremely broad diffraction peaks, [53] and it would thus be very difficult to explain the sharp diffraction features in Figure 3-6 (bottom panel).

To further exclude the contamination of magic sized nanoclusters, a systematic purification procedure was developed (see details in Experimental section). The general chemistry wisdom tells that molecular interaction for two molecules—in this case, nanoparticles—strongly depends on their size and the distance between the center of mass points of two molecules. Thus, the face-face interaction for quantum disks should be much stronger than that between magic sized nanoclusters. Similar to size selective precipitation for size sorting of spherical nanocrystals, [1] the quantum disks should be much easier to be precipitated out from their colloidal solution.

For the reasons described above, centrifugation of a stable quantum disks solution was designed as a central step in purification. The nanocrystals dispersed in the ODE could be precipitated by a regular benchtop centrifuge (at 3000 rpm for 5 minutes). The precipitate could be completely dispersed back into a non-polar solvent and form a stable colloidal solution. UV-Vis measurements (Figure 3-15) revealed that at least 99.9% of the optical density was recovered in the re-dispersed solution and the supernatant only showed negligible UV-Vis signal similar to those in Figure 3-4 A. According to the analysis in the above paragraph, this set of experiments indicate that the nanocrystals given the sharp UV-Vis and PL spectra were largely sized and could be reversibly precipitated from the colloidal solution, which should thus be the colloidal quantum disks.

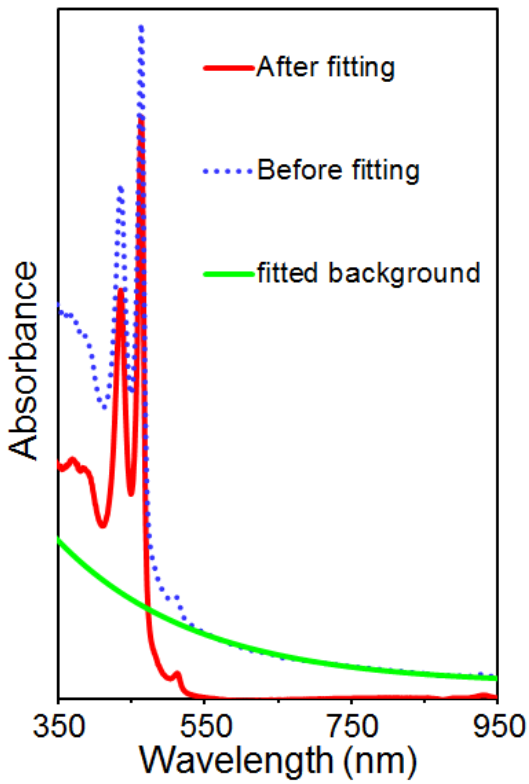

Figure 3-18. Background fitting of CdSe quantum disks UV-Vis absorption.

It should be further mentioned that all measurements discussed in this work except those mentioned specifically were all performed with the products purified using the procedure in the experimental section, which further support the conclusion that the resulting nanocrystals in this work were colloidal quantum disks without contamination of the magic sized nanoclusters. In fact, if the samples were not purified, some nanoparticles were often observed under TEM along with the two-dimensional nanostructures (Figure 3-16), which might cause some confusion in interpretation of the experimental results. However, those particulate impurities did not show any optical activities as mentioned above and could be removed readily using the purification procedure (see Experimental section).

Temperature-dependence for the formation of quantum disks was studied for fatty acids ligands with different chain length. Figure 3-17 shows two series of such reactions. The spectra series on the left is for the nanocrystals synthesized with stearic acid as ligands and the one on the right is for the nanocrystals synthesized using decanoic acid as the ligands. To illustrate the temperature effect directly, the absorbance at 462 nm of the quantum disks normalized with the reaction mixture volume was plotted as an inset for both series with the reaction temperature as the x-axis (Figure 3-17, insets). The normalized absorbance of the UV-Vis peak at 462 nm for a

sample was calculated by removing the background for those relatively high temperature reactions (See Figure 3-18).

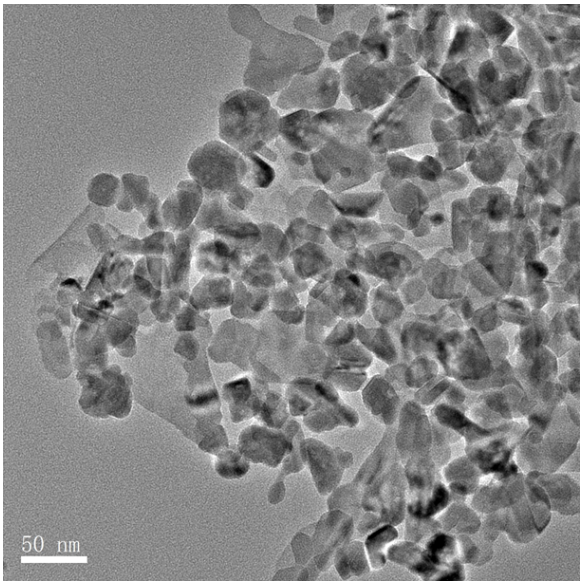

Figure 3-19. TEM image of CdSe after heating up to 260 ^{o}C for 30 minutes.

For both cases shown in Figure 3-17, the formation of the quantum disks did not appear when the temperature was 140 ^{o}C and below. The formation rate of the quantum disks picked up rapidly as the reaction temperature was higher than this low temperature limit, 140 ^{o}C. Simultaneously, as the reaction temperature was higher than a certain level, formation of regular nanocrystals—under TEM, they appeared to be irregular in shape and sizes—with broad absorption features started to show up (see 240 ^{o}C reaction for the stearic acid series and 180 ^{o}C reaction for the decanoic acid series in Figure 3-17). When temperature was higher than an up limit, the formation of those irregular nanocrystals dominated the formation of quantum disks (See the 260 ^{o}C reaction for the stearic acid case and the 240 ^{o}C reaction for decanoic acid case in Figure 3-17 and Figure 3-19), which gave the up limit temperature for each reaction series.

The low temperature limit shall be discussed separately later. As expected, the up temperature limit was found to increase as the chain length of the fatty acids increased (Figure 3-17). Consequently, the temperature for appearance of those irregular nanocrystals was significantly earlier for the decanoic acid series. In addition, the maximum absorbance for the quantum disks

was 180 °C for the decanoic acid series and 240 °C for the stearic acid one. This indicates that, although the hydrocarbon chain did not participate in the surface bonding, it greatly influenced the thermal stability of the two-dimensional nanostructures, which is consistent with "soft-template" growth mechanism as speculated in Introduction Section.

Though the temperature achieving the maximum absorbance of the colloidal quantum disks was found to be lower than the boiling point (b. p.) of corresponding fatty acid, it was substantially higher than its melting point (m. p.) temperature. On the contrary, formation of high quality CdSe quantum dots could be achieved in a temperature range slightly higher than the boiling point of a ligand. [30] This is again consistent with the "soft-template" mechanism proposed.

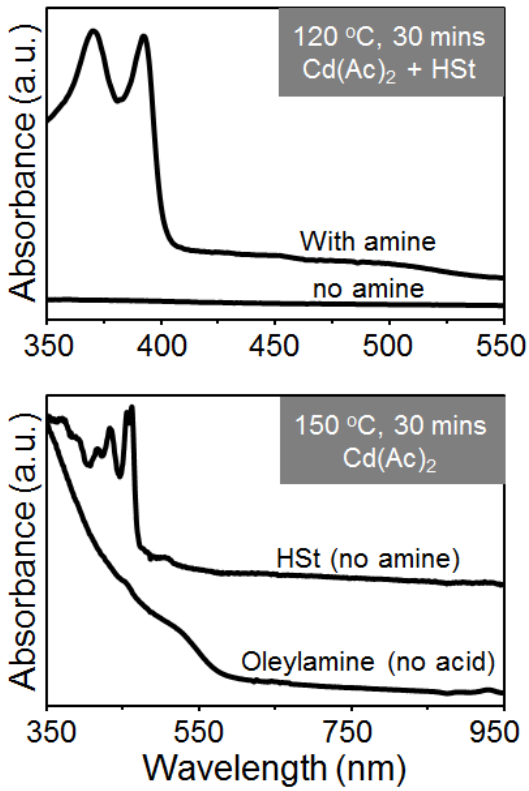

Figure 3-20. The effects of fatty amine on the low temperature limit for the formation of CdSe quantum disks (top), and demonstration of insufficiency of fatty amine on the formation CdSe quantum disks (bottom).

The low temperature limit for formation of the quantum disks was found to be related to the reactivity of the precursors under the reaction temperature range studied. As pointed out above, for the reaction series shown in Figure 3-17, the low temperature limit for both series was approximately the same, i.e., ~140 °C, although the temperature dependence pattern was sensitive to the chain length of the fatty acids.

Experiments were performed to confirm the relationship between the low temperature limit for the formation of the colloidal quantum disks and the reactivity of the precursors. Evidences revealed that fatty amines could activate the formation of chalcogenides nanocrystals when elemental chalcogens were used directly. [54] This led us to add fatty amines into the reaction system and inspect the response of the low temperature limit for formation of the colloidal quantum disks.

The results in Figure 3-20 (top) clearly indicate that formation of two-dimensional quantum disks was possible at 120 ^{o}C if a significant amount of oleylamine was added into the reaction system. On the contrary, under the same reaction conditions except no amine in the reaction system, the control experiment did not show any sign of reaction for the same reaction duration. It should be pointed out that, if no long chain fatty acids was in the reaction system, formation of quantum disks would not occur for the reactions with amine added (Figure 3-20, bottom). The experimental results revealed that, the resulting nanocrystals would be quantum dots for the reaction only with fatty amines but without any long chain fatty acids added. Furthermore, as described above (See Figure 3-13 and the related text), the surface ligands of the CdSe quantum disks were identified as pure fatty acids for the reactions with both fatty amines and fatty acids in place.

The experimental results shown in Figure 3-20 (bottom) not only excluded the possibility of fatty amines as ligands for the formation of CdSe quantum disks, but also imply that the existence of long chain fatty acids would be necessary for the formation of the quantum disks. On the contrary, given that the precursor for both reactions in Figure 3-20 (bottom) was cadmium acetate, acetates were likely too short to be the ligands for stabilization of the basal planes of the quantum disks. This observation is distinctively different from what reported by the

communication published by the Dubtret's group, which speculated that acetate group should be necessary for the formation of two-dimensional CdSe nanostructures. [25]

The thermal stability of the colloidal CdSe quantum disks was briefly examined in the reaction solutions to further identify the nature of up temperature limit for formation of quantum disks. To do so, a sample of CdSe quantum disks was synthesized using the typical procedure at 170 ^{o}C, and the reaction solution stayed at this temperature for 30 minutes in total. As expected, the formation of CdSe quantum disks occurred, indicated by the appearance of sharp absorption peaks as shown in Figure 3-21 (top). At this temperature, a gradual intensity increase of the UV-Vis absorption peaks associated with the quantum disks was also observed (Figure 3-21, bottom).

The reaction solution containing quantum disks was subsequently heated to 260 ^{o}C rapidly and held at this temperature for 30 minutes, which is slightly higher than the up temperature limit for this type of quantum disks (see Figure 3-17 left and the related text). As shown in Figure 3-21, the quantum disks formed at 170 ^{o}C was completely destroyed at 260 ^{o}C, indicated by the featureless absorption spectrum (Figure 3-21, top). In fact, the destruction of the quantum disks was rather fast at this temperature. As shown in Figure 3-21 (bottom), the absorbance of the first excitonic absorption peak of the quantum disks disappeared within five minutes of heating at 260 ^{o}C.

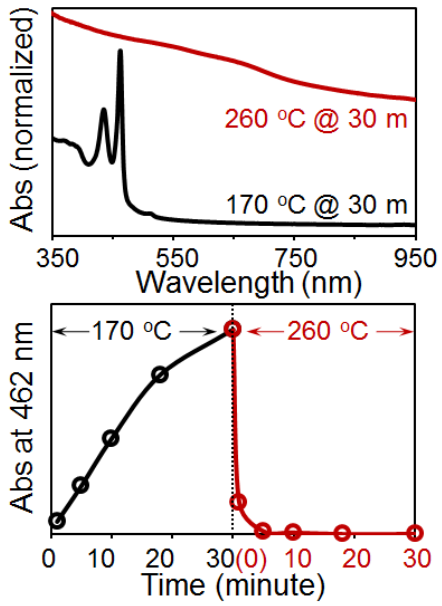

Figure 3-21. Thermal stability of the CdSe quantum disks at 170 ^{o}C and 260 ^{o}C.

The experimental results described in this sub-section indicate that the up temperature limit should be an intrinsic temperature limit for the stability of the quantum disks, instead of a kinetic temperature limit occurred in the growth of the quantum disks. One possible explanation would be that the fatty acid ligand monolayer on the basal planes became unstable at this temperature, which subsequently caused the destruction of the quantum disks.

3.4 Conclusions

The experimental results described above are consistent with the hypothesis that formation of colloidal CdSe quantum disks was a result of suppression of 1D-growth along the polar directions, i.e., either <111> or <001> direction, of the zinc blende lattice. These two directions are the polar axes for the structure, which enabled an alternating packing pattern of Cd and Se layers along the short axis of the quantum disks (Figure 3-10). Suppression of 1D-growth was made possible by terminating both basal planes of the quantum disks with a layer of Cd ions, which were passivated with deprotonated fatty acid ligands. The positive charges caused by the excess layer of Cd ions on the basal planes of each quantum disk were compensated with the negatively-charged carboxylate groups of fatty acid ligands (Figure 3-22).

The thermal stability of such an inorganic-organic assembled nanostructure should be dominated by the relatively weak part of the entire structure, namely, the hydrocarbon monolayer of the fatty acids on both basal planes of a quantum disk. As a result, the growth of colloidal quantum disks would not occur if the temperature was above the up temperature limit for the close packing (Figure 3-22), which is consistent with "soft template" growth mechanism. [30]

The bonding geometry between the fatty acid ligands and the surface Cd ions on the basal planes of the colloidal quantum disks, as described above, was the common "bridging" coordination between two Cd ions and a carboxylate group of deprotonated fatty acids (Figure 3-22). This bonding could have several different functions for the inorganic-organic assembly. Firstly, it helped to saturate the surface dangling bonds of the Cd ions, which resulted in good PL

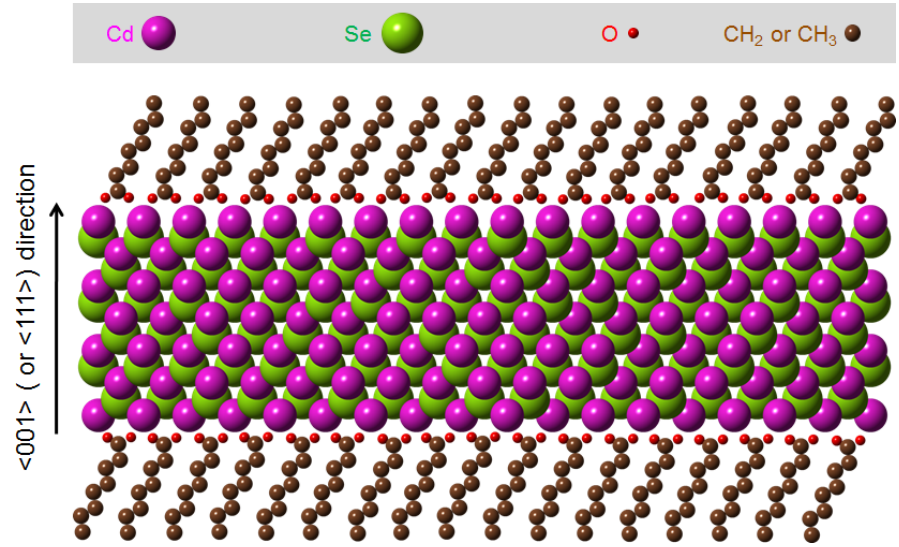

Figure 3-22. Schematic illustration of the colloidal CdSe quantum disk formed through the synthetic scheme shown in Figure 3-1.

properties of the quantum disks in solution (Figure 3-4 A). Secondly, it could balance the positive charges of the excess Cd ions on a CdSe quantum disk with the negative charges of the carboxylate groups of the deprotonated fatty acid ligands. Thirdly, it anchored the surface fatty acid ligands onto the relatively flat basal planes of the colloidal quantum disks, which in turn resulted in a reasonable spatial arrangement for an enhanced packing of the hydrocarbon chains of the fatty acid ligands needed for stability of the inorganic-organic nanostructures.

3.5 References

1. Murray, C. B.; Norris, D. J.; Bawendi, M. G. Synthesis And Characterization Of Nearly Monodisperse CdE (E = S, Se, Te) Semiconductor Nanocrystallites. *Journal of the American Chemical Society* **1993**, *115*, 8706-8715.

2. Peng, Z. A.; Peng, X. G. Formation of high-quality CdTe, CdSe, and CdS nanocrystals using CdO as precursor. *Journal of the American Chemical Society* **2001**, *123*, 183-184.

3. Peng, X. G.; Manna, L.; Yang, W. D.; Wickham, J.; Scher, E.; Kadavanich, A.; Alivisatos, A. P. Shape control of CdSe nanocrystals. *Nature* **2000**, *404*, 59-61.

4. Murray, C. B.; Kagan, C. R.; Bawendi, M. G. Synthesis and characterization of monodisperse nanocrystals and close-packed nanocrystal assemblies. *Annual Review of Materials Science* **2000**, *30*, 545-610.

5. Yin, Y.; Alivisatos, A. P. Colloidal nanocrystal synthesis and the organic-inorganic interface. *Nature* **2005**, *437*, 664-670.

6. Peng, X. G. An essay on synthetic chemistry of colloidal nanocrystals. *Nano Research* **2009**, *2*, 425-447.

7. Bruchez, M.; Moronne, M.; Gin, P.; Weiss, S.; Alivisatos, A. P. Semiconductor nanocrystals as fluorescent biological labels. *Science* **1998**, *281*, 2013-2016.

8. Chan, W. C. W.; Nie, S. M. Quantum dot bioconjugates for ultrasensitive nonisotopic detection. *Science* **1998**, *281*, 2016-2018.

9. Greenham, N. C.; Peng, X. G.; Alivisatos, A. P. Charge separation and transport in conjugated-polymer/semiconductor-nanocrystal composites studied by photoluminescence quenching and photoconductivity. *Physical Review B* **1996**, *54*, 17628-17637.

10. Huynh, W. U.; Dittmer, J. J.; Alivisatos, A. P. Hybrid nanorod-polymer solar cells. *Science* **2002**, *295*, 2425-2427.

11. Colvin, V. L.; Schlamp, M. C.; Alivisatos, A. P. Light-Emitting-Diodes Made From Cadmium Selenide Nanocrystals And A Semiconducting Polymer. *Nature* **1994**, *370*, 354-357.

12. Coe, S.; Woo, W. K.; Bawendi, M.; Bulovic, V. Electroluminescence from single monolayers of nanocrystals in molecular organic devices. *Nature* **2002**, *420*, 800-803.

13. Joo, J.; Son, J. S.; Kwon, S. G.; Yu, J. H.; Hyeon, T. Low-temperature solution-phase synthesis of quantum well structured CdSe nanoribbons. *Journal of the American Chemical Society* **2006**, *128*, 5632-5633.

14. Tang, Z. Y.; Zhang, Z. L.; Wang, Y.; Glotzer, S. C.; Kotov, N. A. Self-assembly of CdTe nanocrystals into free-floating sheets. *Science* **2006**, *314*, 274-278.

15. Son, J. S.; Wen, X. D.; Joo, J.; Chae, J.; Baek, S. I.; Park, K.; Kim, J. H.; An, K.; Yu, J. H.; Kwon, S. G.; Choi, S. H.; Wang, Z. W.; Kim, Y. W.; Kuk, Y.; Hoffmann, R.; Hyeon, T. Large-Scale Soft Colloidal Template Synthesis of 1.4 nm Thick CdSe Nanosheets. *Angewandte Chemie-International Edition* **2009**, *48*, 6861-6864.

16. Ouyang, J. Y.; Kuijper, J.; Brot, S.; Kingston, D.; Wu, X. H.; Leek, D. M.; Hu, M. Z.; Ripmeester, J. A.; Yu, K. Photoluminescent Colloidal CdS Nanocrystals with High Quality via Noninjection One-Pot Synthesis in 1-Octadecene. *Journal of Physical Chemistry C* **2009**, *113*, 7579-7593.

17. Srivastava, S.; Santos, A.; Critchley, K.; Kim, K. S.; Podsiadlo, P.; Sun, K.; Lee, J.; Xu, C. L.; Lilly, G. D.; Glotzer, S. C.; Kotov, N. A. Light-Controlled Self-Assembly of Semiconductor Nanoparticles into Twisted Ribbons. *Science* **2010**, *327*, 1355-1359.

18. Schliehe, C.; Juarez, B. H.; Pelletier, M.; Jander, S.; Greshnykh, D.; Nagel, M.; Meyer, A.; Foerster, S.; Kornowski, A.; Klinke, C.; Weller, H. Ultrathin PbS Sheets by Two-Dimensional Oriented Attachment. *Science* **2010**, *329*, 550-553.

19. Xia, X.; Liu, Z.; Du, G.; Li, Y.; Ma, M. Structural Evolution and Photoluminescence of Zinc-Blende CdSe-Based CdSe/ZnS Nanocrystals. *Journal of Physical Chemistry C* **2010**, *114*, 13414-13420.

20. Sigman, M. B.; Ghezelbash, A.; Hanrath, T.; Saunders, A. E.; Lee, F.; Korgel, B. A. Solventless synthesis of monodisperse Cu2S nanorods, nanodisks, and nanoplatelets. *Journal of the American Chemical Society* **2003**, *125*, 16050-16057.

21. Park, K. H.; Jang, K.; Son, S. U. Synthesis, optical properties, and self-assembly of ultrathin hexagonal In2S3 nanoplates. *Angewandte Chemie-International Edition* **2006**, *45*, 4608-4612.

22. Acharya, S.; Sarma, D. D.; Golan, Y.; Sengupta, S.; Ariga, K. Shape-Dependent Confinement in Ultrasmall Zero-, One-, and Two-Dimensional PbS Nanostructures. *Journal of the American Chemical Society* **2009**, *131*, 11282-+.

23. Choi, J.; Kang, N.; Yang, H. Y.; Kim, H. J.; Son, S. U. Colloidal Synthesis of Cubic-Phase Copper Selenide Nanodiscs and Their Optoelectronic Properties. *Chemistry of Materials* **2010**, *22*, 3586-3588.

24. Wang, Y.; Hu, Y. X.; Zhang, Q. A.; Ge, J. P.; Lu, Z. D.; Hou, Y. B.; Yin, Y. D. One-Pot Synthesis and Optical Property of Copper(I) Sulfide Nanodisks. *Inorganic Chemistry* **2010**, *49*, 6601-6608.

25. Ithurria, S.; Dubertret, B. Quasi 2D Colloidal CdSe Platelets with Thicknesses Controlled at the Atomic Level. *Journal of the American Chemical Society* **2008**, *130*, 16504-+.

26. Manna, L.; Scher, E. C.; Alivisatos, A. P. Synthesis of soluble and processable rod-, arrow-, teardrop-, and tetrapod-shaped CdSe nanocrystals. *Journal of the American Chemical Society* **2000**, *122*, 12700-12706.

27. Peng, Z. A.; Peng, X. G. Mechanisms of the shape evolution of CdSe nanocrystals. *Journal of the American Chemical Society* **2001**, *123*, 1389-1395.

28. Qu, L. H.; Yu, W. W.; Peng, X. P. In situ observation of the nucleation and growth of CdSe nanocrystals. *Nano Letters* **2004**, *4*, 465-469.

29. Xie, R. G.; Li, Z.; Peng, X. G. Nucleation Kinetics vs Chemical Kinetics in the Initial Formation of Semiconductor Nanocrystals. *Journal of the American Chemical Society* **2009**, *131*, 15457-15466.

30. Pradhan, N.; Reifsnyder, D.; Xie, R. G.; Aldana, J.; Peng, X. G. Surface ligand dynamics in growth of nanocrystals. *Journal of the American Chemical Society* **2007**, *129*, 9500-9509.

31. Jones, G.; Jackson, W. R.; Choi, C.; Bergmark, W. R. Solvent Effects On Emission Yield And Lifetime For Coumarin Laser-Dyes - Requirements For A Rotatory Decay Mechanism. *Journal of Physical Chemistry* **1985**, *89*, 294-300.

32. Yu, W. W.; Peng, X. G. Formation of high-quality CdS and other II-VI semiconductor nanocrystals in noncoordinating solvents: Tunable reactivity of monomers. *Angewandte Chemie-International Edition* **2002**, *41*, 2368-2371.

33. Yang, Y. A.; Wu, H. M.; Williams, K. R.; Cao, Y. C. Synthesis of CdSe and CdTe nanocrystals without precursor injection. *Angewandte Chemie-International Edition* **2005**, *44*, 6712-6715.

34. Peng, Z. A.; Peng, X. G. Nearly monodisperse and shape-controlled CdSe nanocrystals via alternative routes: Nucleation and growth. *Journal of the American Chemical Society* **2002**, *124*, 3343-3353.

35. Li, Z.; Cheng, L. N.; Sun, Q.; Zhu, Z. H.; Riley, M. J.; Aljada, M.; Cheng, Z. X.; Wang, X. L.; Hanson, G. R.; Qiao, S. Z.; Smith, S. C.; Lu, G. Q. Diluted Magnetic Semiconductor Nanowires Prepared by the Solution-Liquid-Solid Method. *Angewandte Chemie-International Edition* **2010**, *49*, 2777-2781.

36. McDaniel, H.; Zuo, J. M.; Shim, M. Anisotropic Strain-Induced Curvature in Type-II CdSe/CdTe Nanorod Heterostructures. *Journal of the American Chemical Society* **2010**, *132*, 3286-+.

37. Teranishi, T.; Miyake, M. Size control of palladium nanoparticles and their crystal structures. *Chemistry of Materials* **1998**, *10*, 594-600.

38. Tsunekawa, S.; Ishikawa, K.; Li, Z. Q.; Kawazoe, Y.; Kasuya, A. Origin of anomalous lattice expansion in oxide nanoparticles. *Physical Review Letters* **2000**, *85*, 3440-3443.

39. Baumgardner, W. J.; Choi, J. J.; Lim, Y. F.; Hanrath, T. SnSe Nanocrystals: Synthesis, Structure, Optical Properties, and Surface Chemistry. *Journal of the American Chemical Society* **2010**, *132*, 9519-9521.

40. David, W. I. F. Powder Diffraction Peak Shapes - Parameterization Of The Pseudo-Voigt As A Voigt Function. *Journal of Applied Crystallography* **1986**, *19*, 63-64.

41. Dudka, A. Refinement of the lambda/2 contribution to CCD detector data. *Journal of Applied Crystallography* **2010**, *43*, 27-32.

42. Jenkins, R.; Snyder, R. L., *Introduction to X-ray powder diffractometry*. Wiley: New York, 1996. p. 132.

43. Kirschbaum, K.; Martin, A.; Pinkerton, A. A. lambda/2 Contamination in charge-coupled-device area-detector data. *Journal of Applied Crystallography* **1997**, *30*, 514-516.

44. Porter, D. A.; Easterling, K. E., *Phase transformations in metals and alloys*. Chapman & Hall: London, 1992. p. 112.

45. Ding, Y.; Wang, Z. L. Structure analysis of nanowires and nanobelts by transmission electron microscopy. *Journal of Physical Chemistry B* **2004**, *108*, 12280-12291.

46. Fang, C. M.; van Huis, M. A.; Vanmaekelbergh, D.; Zandbergen, H. W. Energetics of Polar and Nonpolar Facets of PbSe Nanocrystals from Theory and Experiment. *Acs Nano* **2010**, *4*, 211-218.

47. Goldstein, J., *Scanning electron microscopy and x-ray microanalysis*. Kluwer Academic/Plenum Publishers: New York, 2003.

48. Nakamoto, K., *Infrared and raman spectra of inorganic and coordination compounds Part B, Applications in coordination, organometallic, and bioinorganic chemistry*. John Wiley and Sons: Hoboken, N. J., 2009. p. 64-67.

49. Bronstein, L. M.; Huang, X. L.; Retrum, J.; Schmucker, A.; Pink, M.; Stein, B. D.; Dragnea, B. Influence of iron oleate complex structure on iron oxide nanoparticle formation. *Chemistry of Materials* **2007**, *19*, 3624-3632.

50. He, J. B.; Kanjanaboos, P.; Frazer, N. L.; Weis, A.; Lin, X. M.; Jaeger, H. M. Fabrication and Mechanical Properties of Large-Scale Freestanding Nanoparticle Membranes. *Small* **2010**, *6*, 1449-1456.

51. Ouyang, J.; Zaman, M. B.; Yan, F. J.; Johnston, D.; Li, G.; Wu, X.; Leek, D.; Ratcliffe, C. I.; Ripmeester, J. A.; Yu, K. Multiple families of magic-sized CdSe nanocrystals with strong bandgap photoluminescence via noninjection one-pot syntheses. *Journal of Physical Chemistry C* **2008**, *112*, 13805-13811.

52. Wang, R. B.; Ouyang, J. Y.; Nikolaus, S.; Brestaz, L.; Zaman, M. B.; Wu, X. H.; Leek, D.; Ratcliffe, C. I.; Yu, K. Single-sized colloidal CdTe nanocrystals with strong bandgap photoluminescence. *Chemical Communications* **2009**, 962-964.

53. Vossmeyer, T.; Katsikas, L.; Giersig, M.; Popovic, I. G.; Diesner, K.; Chemseddine, A.; Eychmuller, A.; Weller, H. CdS Nanoclusters - Synthesis, Characterization, Size-

Dependent Oscillator Strength, Temperature Shift Of The Excitonic-Transition Energy, And Reversible Absorbency Shift. *Journal of Physical Chemistry* **1994**, *98*, 7665-7673.

54. Li, Z.; Ji, Y.; Xie, R.; Grisham, S. Y.; Peng, X. Correlation of CdS Nanocrystal Formation with Elemental Sulfur Activation and Its Implication in Synthetic Development. *Journal of the American Chemical Society* **2011**, *133*, 17248-17256.

Chapter 4 Thickness-Pure and Colloidal-Stable CdS Quantum Disks with Tunable Thickness: Synthesis and Properties

Thickness-pure and colloidal-stable CdS quantum disks were reproducibly prepared using cadmium acetate, elemental S, fatty acids and octadecene as the starting materials without any size/shape sorting. The thickness was varied between 1.2 and 2.2 nm, i.e, 4.5, 5.5, 6.5 and 7.5 monolayers of CdS unit along the thickness direction. These single crystalline disks with lateral dimensions between 20 and 100 nm were found in zinc-blende crystal structure and with <100> (possibly mixed with <111> direction) as the thickness direction. The basal planes and side facets were terminated with cadmium carboxylates, which dictated the thicknesses to be half a monolayer more than an integer number. Formation of CdS quantum disks was likely through "nucleation-growth" mechanism, instead of aggregation of pre-formed magic clusters. Completion of a full monolayer along lateral direction was found to be rather fast if two-dimensional nucleation was initiated on existing disks, which helped formation of atomic-flat and thickness-controlled disks. As disk thickness decreased, the crystal lattice was found to dilate gradually, which was not observed with CdS quantum dots. Compared with CdS quantum dots and rods, the disks displayed weakened quantum confinement and their photoluminescence lifetime (tens of picoseconds) was about 2-order of magnitude faster.

4.1 Introduction

Synthesis of colloidal semiconductor nanocrystals has achieved substantial success in the recent twenty years. [1, 2] Dot- [3, 4] and rod-shaped [5, 6] semiconductor nanocrystals (quantum dots and quantum rods) can be synthesized with reasonable size- and shape-control within their quantum

confinement size regime for many types of compound semiconductors. The existing synthetic schemes for quantum dots and quantum rods are not only relatively safe and inexpensive ("greener" synthesis), [1, 2] but also don't require any additional size- and shape-sorting to achieve high optical quality. Conversely, synthesis of semiconductor nanocrystals with quantum confinement only along one dimension (colloidal 2D nanocrystals) in the shape of sheets, [7, 8] platelets, [9, 10] belts, [11-14] and disks [15] with ultra-thin thickness falls far behind, especially when one considers necessary colloidal stability for solution-based manipulation. Although colloidal 2D nanocrystals are not readily accessible at present, their properties are found to be unique in comparison to both quantum dots and quantum rods. For instance, the band-edge photoluminescence (PL) peaks of CdSe 2D nanocrystals were found to be extremely narrow (full width at half maximum is less than 10 nm), which is less than half of corresponding narrowest band-edge PL of CdSe quantum dots reported so far. [16] As one of the most promising new class of emitters, such narrow emission peaks are not only fundamentally interesting but also advantageous versus organic dyes for bio-medical labeling at multiple-target detections, [17, 18] flexible light-emitting-diodes (LEDs) with high color purity, [19, 20] etc.

At present, even for the best developed system—CdSe ones, at most two different thicknesses of colloidal CdSe 2D nanocrystals have been reported with substantial purity in thickness without size sorting. [14, 15] In preparation of this chapter, we noticed that the Dubertret's group reported preparation of CdS and CdTe nanoplatelets along with CdSe ones. [21] In their report, though size- and shape-sorting did yield CdSe nanoplatelets with four different thicknesses, the CdS and CdTe ones were unfortunately mixtures of different thicknesses even after size- and shape-sorting. Thus, one motivation of this work was, using CdS thickness-pure quantum disks covering the entire quantum confinement window as a model system, to demonstrate synthesis of

quantum disks at the level of standard "greener approach" for quantum dots and quantum rods established in literature. Such greener approaches should be simple, with inexpensive shelf chemicals, reproducible, without size- and shape-sorting, and yields colloidal-stable nanocrystals.

Difficulties on synthesizing thickness-pure quantum disks with tunable thickness are at least partially due to lack of understanding on their formation mechanisms. The Weller's research group reported an "oriented attachment" mechanism for formation of PbS nanosheets with their thickness in quantum confinement regime. [8] For the most developed CdSe 2D nanocrystals, there are two competitive mechanisms proposed. The Dubertret's group suggested a typical "nucleation-growth" mechanism. [10] Our results indicated a similar nucleation-growth pathway for CdSe quantum disks and further revealed that the charged carboxylate ligands likely played a key role as soft-templates. [15] Conversely, the Buhro's research group recently suggested a general mechanism which involves oriented attachment of CdSe magic sized clusters as a necessary step ("clusters-attachment" mechanism). [14] Prior to the detailed studies carried out by the Buhro's group, the Hyeon's group suggested that self-assembly of cadmium precursors into lamellar structures might have played a key role. [12] Meanwhile, our group showed oriented attachment indeed occurred in a synthetic system similar to the one used by the Buhro's group although we failed to recognize the one-dimensional quantum confinement nature of the resulting nanostructures and assigned the resulting nanostructures as quantum wires with two-dimensional quantum confinement. [22] With these facts in mind, our second motivation of this work was to combine the growth mechanisms study with development of synthetic strategy. The results shown below shall reveal that formation of CdS quantum disks followed a nucleation-growth mechanism, instead of clusters-attachment mechanism. In addition, the results further

suggested that a two-dimensional nucleation process might have played an important role in controlling the thickness purity of the disks.

Success on synthesizing a series of quantum disks with pure thicknesses in the entire quantum confinement regime allowed us to compare the quantum confinement of quantum disks with the corresponding quantum dots. As expected, the CdS quantum disks with a given thickness showed a significantly weaker quantum confinement in comparison to the quantum dots with the same dimension in size. This series of quantum disks further enabled us to study an interesting lattice dilation effect, which was identified to be thickness dependent. Conversely, CdS quantum dots coated with the same type of ligands did not show such lattice dilation, even for those relatively small quantum dots with their sizes similar to the thickness of the quantum disks. In addition to these two thickness-dependent properties, availability of a series of high quality quantum disks further allowed us to study the cation to anion ratio (Cd to S ratio) in the disks, which were found to increase significantly as the thickness of quantum disks decreased. This indicates that the surface of the disks was terminated with Cd ions. To understand the unique optical properties of the quantum disks, some preliminary time-resolved spectroscopy studies of the CdS quantum disks were carried out.

4.2 Experimental

Chemicals. Cadmium acetate dihydrate (99.999%, Alfa), melissic acid (TCI), myristic acid (98%, Alfa), oleic acid (90%, Aldrich), oleylamine (80-90%, Aldrich), stearic acid (90%, Alfa), sulfur (99.5%, Alfa), 1-octadecene (90%, ODE, Alfa), tributylphosphine (95%, TBP, Alfa), CdS (Aldrich), erythrosin B (Alfa), stilbene 420 (Exciton), coumarin 545 (Exciton), chloroform (EM

Science), ethanol (EtOH, Pharmco), hexanes (EM Science), methanol (EM Science), toluene (Mallinchrodt) were used without further purification.

Synthesis of disks. S in ODE solution was prepared by dissolving 0.0320 g Sulfur (1.0 mmol) in 20 g ODE by gentle sonication and stored in closed vial for use. Except the thinnest one with oleylamine added as the activation reagent for S at a relatively low reaction temperature (see below), the other three thicknesses could all be synthesized with cadmium acetate dihydrate, sulfur, fatty acids, and ODE as the starting materials. Among all fatty acids tested, myristic acid and stearic acid could only yield disks with two thinner ones, oleic acid worked for three thin ones but not the thickest one, and melissic acid was the only ligand which could yield all four types of disks. Considering the cost of fatty acids, typical synthesis for a specific thickness would be mostly with less expensive oleic acid as the ligands.

Synthesis of CdS quantum disks with the first absorption peak at 328 nm: cadmium acetate dihydrate (0.0533 g, 0.20 mmol), S in ODE solution (1.0016 g, 0.05 mmol S) prepared using the method described above, oleic acid (0.0565 g, 0.20 mmol), oleylamine (0.05 g, 0.19 mmol), and 2.95 g ODE was bubbled with Ar for 10 minutes, then heated to 170 ^{o}C in 9 minutes from room temperature under Ar flow, and kept under 170 ^{o}C for 5 minutes, small aliquots were taken out at different time intervals, diluted in chloroform and measured by UV-Vis to monitor the reaction.

Synthesis of CdS quantum disks with the first absorption peak at 374 nm: cadmium acetate dihydrate (0.0533 g, 0.20 mmol), S in ODE solution (1.0016 g, 0.05 mmol S), myristic acid (0.0457 g, 0.20 mmol), and 3.0 g ODE was bubbled with Ar for 10 minutes, then heated to 180 ^{o}C in 8 minutes from room temperature under Ar flow, and kept under 180 ^{o}C for 30 minutes,

small aliquots were taken out at different time intervals, diluted in toluene and measured by UV-Vis to monitor the reaction.

Synthesis of CdS quantum disks with the first absorption peak at 407 nm: cadmium acetate dihydrate (0.0533 g, 0.20 mmol), S in ODE solution (1.0016 g, 0.05 mmol S), oleic acid (0.0565 g, 0.20 mmol), and 3.0 g ODE was bubbled with Ar for 10 minutes, then heated to 260 ^{o}C in 15 minutes from room temperature under Ar flow, and kept under 260 ^{o}C for 1 minute, small aliquots were taken out at different time intervals, diluted in toluene and measured by UV-Vis to monitor the reaction.

Synthesis of CdS quantum disks with the first absorption peak at 431 nm: cadmium acetate dihydrate (0.0533 g, 0.20 mmol), S in ODE solution (1.0016 g, 0.05 mmol S), melissic acid (0.0226 g, 0.05 mmol), and 3.0 g ODE was bubbled with Ar for 10 minutes, then heated to 250 ^{o}C in 14 minutes from room temperature under Ar flow, and kept under 250 ^{o}C for 15 minutes, small aliquots were taken out at different time intervals, diluted in toluene and measured by UV-Vis to monitor the reaction. Caution: Special care needed to be paid for the synthesis apparatus airtightness to avoid the possible formation of cadmium oxide for this specific reaction because of its relatively low fatty acid concentration.

Purification of CdS quantum disks. For TEM measurements, purification of CdS quantum disks was generally carried out by following procedure. TBP and EtOH mixture (10% volume ratio of TBP) was added into the final products, sonicated, then centrifugated at 4,000 RPM for 5 minutes. The precipitate was preserved, and repeated for another 2 times. Purified samples were dissolved into toluene or hexanes forming clear solution. For the HRTEM studies carried out in Figure 4-3, special care was taken to avoid the unintentional removal of small CdS quantum

disks seeds, the purification was carried out by adding methanol to the CdS quantum disks in hexanes solution, sonication and analog vortex was used to promote extraction efficiency. The solution was centrifugated at 4,000 RPM for 15 minutes, then set aside until clear phase separation appeared. The top hexanes layer was then carefully collected for HRTEM studies.

Purification of CdS quantum disks for XRD and EDX characterization was similar with the aforementioned procedure except that centrifugation was carried out at 3,000 RPM for 15 minutes. In addition, EtOH was used to wash the precipitate one more time and the final precipitate was preserved and dried in vacuum oven overnight before grinding in mortar for XRD analysis or applied to the conducting tape for EDX analysis.

Optical Measurements. UV-vis spectra were taken on an HP 8453 UV-visible spectrophotometer. Photoluminescence spectra were measured using a Spex Fluorolog-3 fluorometer. The quantum yield data reported in this work were obtained using stilbene 420 in methanol (95%), [23] coumarin 545 in EtOH (90%) [24] as the standard.

Time-resolved photoluminescence (TRPL) on the picosecond scale were performed by using a Ti : sapphire mode-locked laser delivering 3 ps pulses at 76 MHz repetition rate with the samples dissolved in toluene at room temperature. The excitation wavelength was tuned to 375 nm which was provided by a second harmonic generator (1 mm thick beta barium borate). The luminescence was dispersed by a 0.24 m single monochromator coupled with a Streak Camera (Hamamatsu) operating in synchron scan mode, equipped with a two-dimensional charge-coupled device. The system provided an overall time resolution of about 15 ps and an energy resolution of about 1 meV. The nanosecond time-resolved emission decay of the CdS quantum dot solution was measured using a FLS 920 photocounting system (Edinburgh Instruments Ltd., UK) at room temperature. The excitation light source was a 405 nm pump laser at 2 MHz.

Transmission Electron Microscopy (TEM) and High-resolution TEM (HRTEM). TEM and HRTEM images were taken on FEI Titan 80-300 microscope with an accelerating voltage of 300 kV. Purified CdS quantum disks were dispersed into toluene or hexanes, then several drops of the solution were added onto a carbon coated copper grid and the grid with the nanocrystals was dried in air.

X-ray powder diffraction (XRD) patterns were acquired using Rigaku MiniFlex II X-ray diffractometer operating at 30kV/15mA.

Energy-dispersive X-ray spectroscopy (EDX) was used for elemental analysis using a Philips ESEM XL30 scanning electron microscope equipped with a field emission gun and operated at 30 kV.

4.3 Results and Discussions

Choice of synthetic system. Although our recent work on synthesis of CdSe quantum disks only yielded one pure thickness, [15] the results provided us some hints on rational design of synthetic schemes for CdS quantum disks. The structural characterization of the CdSe quantum disks revealed that both basal planes of the disks were terminated with a monolayer of Cd ions. If CdS quantum disks to be synthesized possessed the same structure, the organic ligands should be negatively charged. This hypothesis indicates two key design parameters for the synthetic system of CdS quantum disks. The first implication is that fatty acids commonly used in nanocrystals synthesis should be a reasonable choice as the ligands and cadmium carboxylate salts could be used as the Cd precursor. The second implication is that the synthetic system should have a relatively high Cd to S precursor ratio.

Previous experiences on synthesis of high quality CdS quantum dots told us that non-coordinating solvents could offer us tunable reactivity of the precursors, [25] which should be much needed for synthesizing thickness-tunable CdS quantum disks. A recent study indicates that elemental S dissolved in octadecene (ODE)—the most commonly used non-coordinating solvent in synthesis of colloidal nanocrystals—became substantially reactive at around 180 ^{o}C in a simple reaction system with ODE, cadmium fatty acid salts, fatty acid, and elemental S. [26] For such a reaction system, if the reaction needed to be carried out significantly below 180 ^{o}C, fatty amines could be used as activation reagents for elemental S. [26]

As mentioned above, our previous method could only yield CdSe quantum disks with one pure thickness. Some preliminary results on that system indicated that a higher reaction temperature would benefit the growth along the thickness direction. However, results on CdSe quantum disks revealed that those very thin quantum disks were thermally unstable under elevated temperatures, and thermal stability of the CdSe quantum disks was found to be associated with the chain length of the fatty carboxylate ligands. The longer the hydrocarbon chain, the more stable the CdSe quantum disks were. [15] This means that fatty acid ligands with long hydrocarbon chain might be needed to obtain thickness-pure CdS quantum disks within the entire quantum confinement window.

It should be pointed out that the hypothesis mentioned in the above paragraph was partially supported by the results reported by the Yu's group. [27, 28] They reported several sets of CdSe and CdS nanocrystals samples with sharp absorption spectra, which could be quantum disks although the Yu's group considered them as "magic sized clusters". Specifically for CdS system, they reported two sets of sharp absorption spectra, with the lowest absorption peak respectively at 324 nm and 378 nm, although they used complex and expensive bis(trimethylsilyl)sulfide as the S

precursor. [28] If these two spectra were indeed from CdS quantum disks, they should be two relatively thin CdS disks within the series to be discussed below.

Thickness control of CdS quantum disks.

As shown in Figure 4-1, CdS quantum disks with four distinguishable thicknesses were synthesized without any size- and shape-sorting, which covered most part of the quantum confinement regime for CdS nanocrystals. It is well known that CdS quantum dots are typically with their first excitonic absorption peak between 320 nm and 450 nm. [25] The thickness of each sample was determined by measuring the disks with appropriate orientation under High Resolution Transmission Electron Microscope (HRTEM). Based on the structural parameters of zinc-blende CdS and composition analysis to be described below, these four samples corresponded to CdS with 4.5, 5.5, 6.5, and 7.5 monolayers of CdS units along thickness direction. Further confirmation of the thickness will be discussed together with the structural analysis and quantum confinement calculations.

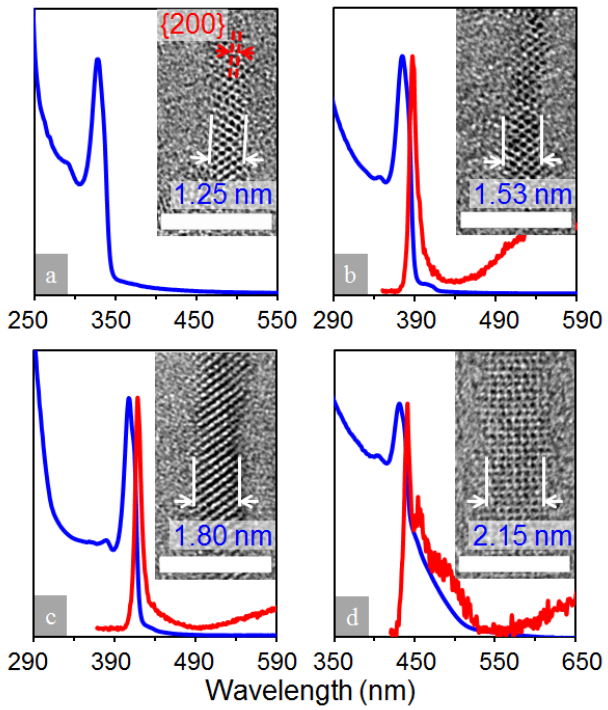

Figure 4-1. UV-Vis (blue curve) and PL (red curve) of four CdS quantum disk samples with a typical HRTEM image of a side-on disk (inset, scale bar: 5nm, see corresponding full-scale HRTEM images in Figure 4-2) for each sample.

It was found that, with melissic acid ($CH_3(CH_2)_{28}COOH$) as the ligands, the whole series of the thickness-pure CdS disks shown in Figure 4-1 could be synthesized without any size- and shape-sorting. Evidently, its unusually long hydrocarbon chain rendered the reaction temperature to a desired range, between 170 ^oC and 260 ^oC (see details in experimental section). Experimental results further revealed that myristic acid and stearic acid could only yield disks with two thinner thicknesses, oleic acid worked for three thin ones but not the thickest one. The thickness purity of the CdS quantum disks with stearic acid and myristic acid as ligands would be compromised as the reaction temperature approached 240 ^oC. With these results, one could safely conclude that there is no direct correlation between the chain length of fatty acids and the thickness of the CdS disks. Instead, as long as a fatty acid could retain necessary stability for CdS disks under the reaction temperature necessary for growth of thicker disks, the fatty acid ligand could be used for growth of thinner ones.

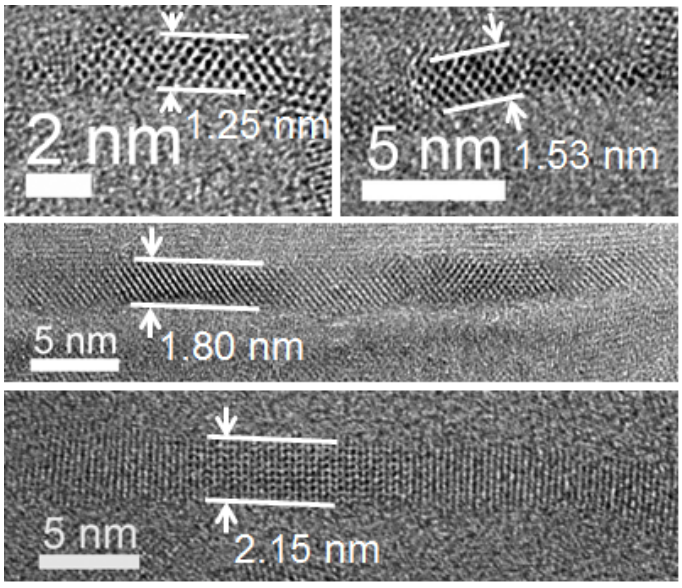

Figure 4-2. Full scale HRTEM image of CdS quantum disks in Figure 4-1.

It was found that the thinnest one could only be synthesized with addition of fatty amine as the activation reagent for S. [26] This is so because the thinnest ones (Figure 4-1a) could be stable only when the reaction temperature was 170 ^oC or below. At this temperature, our recent report revealed that elemental S is not sufficiently active and addition of amine can enhance its

reactivity. [26] As shown below and demonstrated in the case of CdSe disks, [15] although amines were added into the reaction system, the resulting disks were still significantly Cd rich and coated with carboxylate ligands.

Formation mechanism: "nucleation-growth" versus "clusters-attachment". For zinc-blende CdSe system, as discussed in the introduction, previous results indicate that nanoplatelets or quantum disks were formed by growth of molecular unites onto pre-formed nuclei, namely a "nucleation-growth" mechanism. [10, 15] Conversely, wurtzite CdSe [14] and cubic PbS system [8] (galena) 2D nanostructures were found to be formed by oriented-attachment of pre-formed magic sized clusters, to be called as "clusters-attachment" mechanism. The mechanism proposed by the Hyeon's group was somewhat different from a pure clusters-attachment mechanism, which suggested that cadmium-amine complexes formed lamellar structure and Se precursors diffused into such lamellar structure and generated CdSe wurtzite nano-sheets. [12] Despite the difference, this mechanism and clusters-attachment mechanism had one feature in common, that is the formation of large sized aggregates to show substantial light scattering. Conversely, under controlled nucleation-growth mechanism for formation of high quality colloidal quantum dots and disks, largely size aggregates should not present.

If the two-dimensional nanostructures were formed by clusters-attachment mechanism, in addition to light scattering in their UV-Vis spectra, one should also observe a noticeable spectral shift of absorption peaks. Because of the relatively strong three-dimensional quantum confinement, magic sized clusters with their sizes similar to the thickness of 2D nanocrystals should possess a substantially blue-shifted absorption spectrum [29] (see more discussions below). In the report by the Buhro's group, the clusters-attachment in the wurtzite CdSe system studied did show some evidences of spectral shift. [14] In the system similar to that studied by the Buhro's

group, we reported a significant red-shift in the temporal evolution of absorption spectra during the clusters-attachment process. [22]

Based on the spectral features discussed in the above two paragraphs, a significant red-shift and a scattering tail, were used as two initial guidelines in identification of the formation mechanism in the current system. UV-vis absorption spectroscopy coupled with HRTEM was used as the main experimental tools.

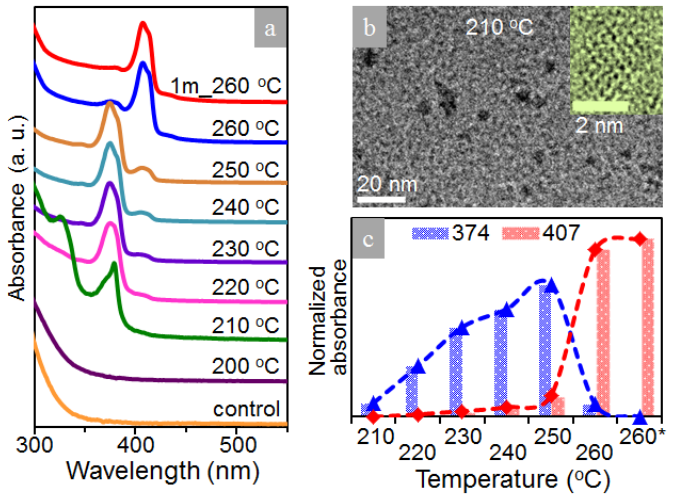

Figure 4-3. a: UV-vis absorption spectra of growth process for CdS quantum disks with the first absorption peak at 407 nm. b: TEM and HRTEM (inset) images of the sample at the early growth stage of 210 °C. c: Normalized UV-vis absorption peak intensity during the growth process. 260 corresponds to the spectrum of 1 minute at 260 °C in figure 4-3a.*

Figure 4-3 a illustrates evolution of absorption spectra of a typical reaction as the reaction increased from 200 °C to 260 °C (about 8 °C/minute). Figure 4-3 b shows a TEM picture of the sample taken at 210 °C with a false colored HRTEM image as inset. As shown in Figure 4-3 a, there was no noticeable spectral shift in the early formation stage of the quantum disks for this typical reaction and any other reactions studied. This indicates that clusters-attachment is unlikely associated with the current system. Consistent with this conclusion, TEM studies of early aliquots (Figure 4-3 b) revealed nanocrystals with their sizes in the range between ~2-12 nm. These nanocrystals should be CdS

quantum disks with small lateral dimensions because quantum dots with such sizes should possess a much red-shifted UV-Vis spectrum in comparison to the one shown in Figure 4-3 a (marked as "210 ^{o}C").

The exclusion of clusters-attachment mechanism was further supported by no significant scattering tail in the absorption spectra (Figure 4-3 a). It should be mentioned that, under certain conditions, reactions after a long time could yield crystalline CdS nanosheets with a significant scattering tail in the UV-Vis spectra. However, such scattering was considered to be different from that associated with clusters-attachment mechanism [14] and template mechanism. [12] In the clusters-attachment mechanism and template mechanism, scattering tail should appear early on, instead of appearing at the end of the reaction. Importantly, as we were targeting colloidal-stable quantum disks, our samples discussed in this chapter are all without a significant scattering tail except those stated specifically.

The evidences discussed above are apparently consistent with nucleation-growth mechanism. If the reaction temperature was set at a specific value for the growth of CdS quantum disks with a relatively thin thickness, for instance at 180 ^{o}C for the quantum disks with its absorption peak at 374 nm, one would observe a continuous increase of absorption peak intensity of the existing CdS quantum disks normalized to the reaction volume, which is similar to the case of CdSe ones. [10] For the relatively thick ones, careful studies revealed a different mode of growth.

Growth mechanism: thickness growth. As shown in Figure 4-3 a, the thicker CdS quantum disks with their UV-Vis peak at 407 nm appeared after the formation of the next thinner ones with their absorption peak at 374 nm along with the increase of reaction temperature. Quantitatively, at 260 ^{o}C, while the volume-normalized intensities at 407 nm increased sharply, the volume-normalized intensity at 374 nm decreased simultaneously (Figure 4-3 c). Based on the results shown in

Figure 4-1, this corresponded to one-monolayer addition along the thickness direction. It should be pointed out that the Buhro's group also observed growth of thicker CdSe wurtzite nanobelts from relatively thin ones in a similar manner although, as discussed above, the general growth mechanism was identified as clusters-attachment.

The results shown in Figure 4-3 a and 4-3 c imply that the addition of one monolayer of CdS to the existing thin quantum disks was rather rapid. This is quite reasonable. According to existing crystallization theories, [30] when growth on a flat surface was initiated (often called two-dimensional nucleation), the following completion of the monolayer would usually be quite fast. Furthermore, this phenomenon is probably playing a determining role in formation of high quality quantum disks. Presumably, if a suited two-dimensional seed (or nucleus) was formed in the solution, the extension along the lateral dimensions could become the dominating growth mode, given that the difficult initiation and fast completion of a monolayer on the

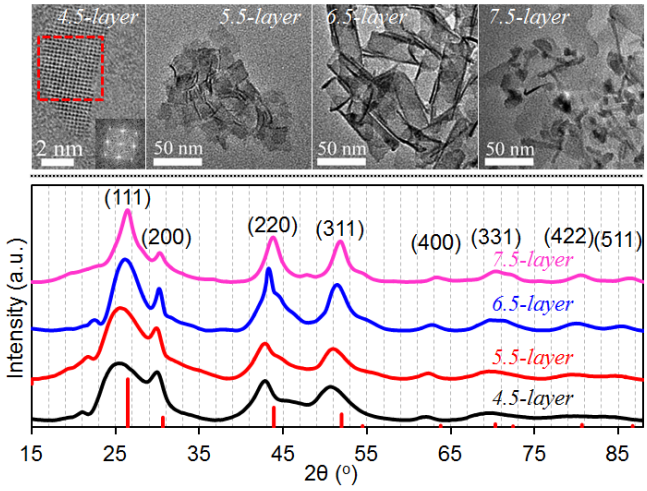

Figure 4-4. Top: from left to right are HRTEM image and FFT of 4.5-layer thick CdS disks, and TEM images of 5.5, 6.5, and 7.5-layer thick CdS quantum disks. Bottom: X-ray diffraction patterns of CdS quantum disks (thickness increases from bottom to top). The standard diffraction peaks of zinc blende structure (JCPDS card no. 89-0440) are inserted as red lines for reference.

basal planes. For the same reason, the resulting disks could readily be atomic flat on the basal planes.

Above mechanism implies "addition" of solution monomers onto the top of existing thin disks in a layer-by-layer fashion. Consistent with this thickness growth model, if the reaction system was held at a lower growth temperature for a long time to allow the full growth of the thinner disks, conversion of thin disks to the next thickness in the series would become difficult. Presumably, full growth of the thin ones consumed reactive precursors in the system and the system could no longer offer sufficient amounts of precursors for the thickness growth.

Lateral dimensions and colloidal-stability. The lateral dimensions of the CdS quantum disks could be controlled by the reaction time at a designated reaction temperature. By varying the reaction temperatures within the range for formation of the targeted thickness, the lateral dimensions could also be varied to a certain degree. Our aim was to obtain quantum disks with thickness-tunable and thickness-pure yet possessing good colloidal-stability. The typical lateral dimensions were thus controlled in the range between 20 and 100 nm (Figure 4-4, top panel). The TEM images in Figure 4-4 (top panel) further reveal that control of lateral dimensions still has significant room to improve, which is generally true at this stage for all two-dimensional semiconductor nanostructures with thickness in corresponding quantum confinement size regime.

The morphology of the CdS quantum disks were found to be approximately rectangular as shown in Figure 4-4 (top panel). Similar to what observed in CdSe quantum disks, [15] some curved edges along one direction was observed (Figure 4-4, top panel) if the lateral dimensions of the colloidal-stable disks was relatively large. For the thickest disks in the current series, TEM measurements reproducibly revealed some relatively high contrast spots on the disks (Figure 4-4,

top panel) and could not be removed by all purification methods tested. This could be due to partial folding of the disks caused by the relatively high reaction temperature.

CdS quantum disks within their lateral dimensions in the range between 20 and 100 nm synthesized using the current synthetic scheme were found to be generally colloidal-stable. For instance, the disks solution in $CHCl_3$ was found to possess colloidal stability even with 4000 rpm centrifugation.

Crystal structure and composition. The X-ray powder diffraction (XRD) patterns of the CdS quantum disks with different thicknesses are shown in Figure 4-4 (bottom panel). Similar to CdSe quantum disks, these diffraction patterns are consistent with a zinc-blende structure. A sharp peak superimposed on top of a broad feature for (111), (220), and (400) diffraction peaks is consistent with polar directions of the zinc-blende lattice as the thickness directions. This means that, as verified in our previous report for CdSe quantum disks, the thickness directions for CdS quantum disks should be <100> and (or) <111> of the zinc-blende lattice.

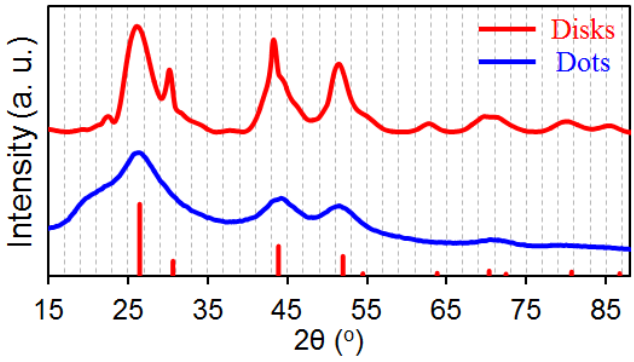

Figure 4-5. XRD patterns of CdS quantum disks (red) and quantum dots (blue) with the same PL peak positions for comparison purpose. The standard diffraction peaks of zinc blende structure (JCPDS card no. 89-0440) are inserted as red lines for reference.

Based on XRD results, it was difficult to distinguish <111> axis from <100> axis as the thickness direction of the disks. However, there was evidence suggesting that <111> axis was at least not the dominating thickness orientation. The first

evidence was HRTEM results. As shown in Figure 4-1 and Figure 4-4, only lattice fringes matching <100> direction as the thickness direction were successfully observed under HRTEM with a limited number of disks measured. The second evidence was that thicknesses determined by quantum confinement calculations (to be discussed in details below) matched very well with the expected values for the thicknesses along <100> direction for all four disk samples (Table 4-1), which were 4.5, 5.5, 6.5, 7.5 monolayers along <100> axis as revealed by HRTEM images in Figure 4-1. Again, the extra monolayer of Cd ions on one of two basal planes will be discussed below.

The HRTEM image and the corresponding FFT (Fast Fourier Transform) in the red-dotted area (inset) of a quantum disk lying flat on the substrate are shown in Figure 4-4 (the first image in top panel). The results confirmed its zone axes as <001>, which is consistent with the growth direction identified by HRTEM with the side-on disk (Figure 4-1). However, two relatively thick samples were found to be difficult to obtain clear phase contrast for the lying flat disks. It should be pointed out that the lattice plane distance along thickness direction (Figure 4-1a) gave us a value of 0.299 nm, which is 2.4% greater than that for the {200} lattice planes of bulk zinc blende CdS (0.292 nm), and shall be discussed in details below.

Monolayer	200 (nm)	HRTEM (nm)	Calculation (nm)
4.5	1.17	1.25	1.22
5.5	1.46	1.53	1.53
6.5	1.75	1.80	1.87
7.5	2.04	2.15	2.25

Table 4-1. Thickness calculation results along <200> direction and corresponding HRTEM measurement, theoretical calculation results based on heavy hole position.

It was interesting to notice that the lattice of CdSe 2D nanostructures could be either compressed or expanded dependent on the crystal structure. The

Buhro's group observed a noticeable lattice contraction for wurtzite CdSe nanobelts, [14] and our group reported lattice expansion for zinc-blende CdSe quantum disks. [15] Unfortunately, in both cases, the thickness-pure samples were limited to one or two thicknesses.

A qualitative inspection of the XRD patterns in Figure 4-4 (bottom panel) told us that all four samples showed significant lattice dilation in comparison to the bulk values. Furthermore, CdS quantum dots with their size similar to the thicknesses of quantum disks did not show such dilation (Figure 4-5). Table 4-2 summarizes observed dilations determined by the XRD patterns in Figure 4-4 (bottom panel). To further illustrate this interesting phenomenon, the results for the (111) peak was plotted in Figure 4-6 (left). In comparison to the bulk value, as the thickness increased in the series, the lattice dilation value of 3.97%, 3.51%, 1.29%, and 0.07% from the thinnest to thickest sample was determined, with the thickest one very close to the bulk value.

The lattice expansion and its thickness-dependence seemed to be reasonable, provided that the top and bottom basal planes were both terminated with Cd ions (see details below). The excess layer of Cd ions could offer significant lattice strain and such strain would increase as the

Peak	Standard (Å)	4.5-layer (Å)	Dilation (%)	5.5-layer (Å)	Dilation (%)	6.5-layer (Å)	Dilation (%)	7.5-layer (Å)	Dilation (%)
111	3.366	3.500	3.97	3.484	3.51	3.409	1.29	3.368	0.07
200	2.915	2.979	2.19	2.987	2.48	2.956	1.42	2.951	1.22
220*	2.061	2.108	2.27	2.109	2.35	2.088	1.32	2.064	0.17
311	1.758	1.800	2.40	1.791	1.88	1.775	0.95	1.762	0.23
400	1.458	1.494	2.50	1.488	2.07	1.478	1.38	1.467	0.65

Table 4-2. Comparison of d-values for different diffraction peaks between CdS quantum disks and bulk. For (220) peak, the sharp peak position was taken to calculate the corresponding lattice value.

thickness of the quantum disks decreased.

It should be noticed that, by comparing the positions of the sharp peak to the broad feature of (220) diffraction, one would conclude that the lattice dilation along thickness direction differed from that along the lateral direction. The same trend could also be identified for the CdSe quantum disks studied previously. More studies are needed to fully understand this interesting phenomenon.

As discussed above, the thickness directions of CdS quantum disks were polar directions, namely, most likely <100> direction but with small possibilities mixed with <111> direction. Furthermore, the basal planes of quantum disks should be close to atomic flat, given their sharp optical spectra and fast completion of a monolayer along lateral directions as discussed above (see Figure 4-3 and the related text). In addition, the ligands of the CdS quantum disks were carboxylates. All these facts imply that both basal planes of CdS quantum disks should be terminated with a monolayer of Cd ions, which in turn should be bound by deprotonated fatty acid ligands. [15] To confirm this, the Cd to S atomic ratio (Cd/S ratio) of carefully purified CdS quantum disks was determined using quantitative Energy-Dispersive X-ray (EDX) analysis.

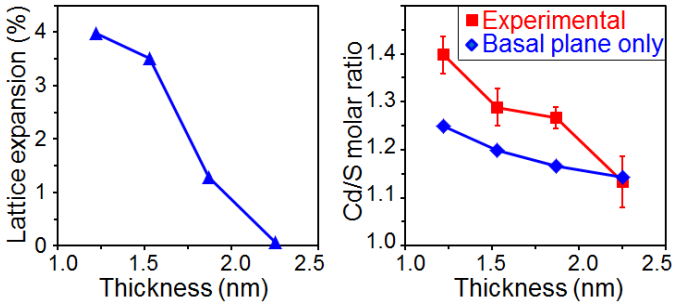

Figure 4-6. Left: Lattice expansion of the (111) peak in CdS quantum disks with different thickness. Right: Cd/S molar ratio of CdS quantum disks with different thickness. The blue diamonds linked by a blue line were calculated values considering one-monolayer of Cd ions on both basal planes.

Results in Figure 4-6 (right) indicate that all four samples were indeed Cd-rich (See Table 4-3 for more details). Though similar composition feature was observed for one thickness of CdSe quantum disks previously, [15] availability of a full series of thickness-pure CdS quantum disks allowed us to examine the thickness-dependence of the Cd/S ratio. Results in Figure 4-6 (right) revealed that the Cd/S ratio increased substantially as the thickness decreased, which seemed to be consistent with one-monolayer of extra Cd ions on one of the basal planes suggested for CdSe quantum disks. With these facts, one could reasonably conclude that the thicknesses of the disks could not be integer numbers of CdS repeating units. This is the reason we assigned the thicknesses of the disks to be 4.5, 5.5, 6.5, and 7.5 monolayers of CdS repeating unit along the

Quantum discs	Cd % (molar ratio)								Mean	Calculation considered basal planes only
328	59.44	58.26	58.83	57.16	58.45	58.42	57.62	58.15	58.29 ± 0.70 [a]	~ 55.6
374	56.03	56.85	57.63	55.88	56.11	56.79	55.15	55.98	56.30 ± 0.76	~ 54.5
408	56.37	56.41	55.12	56.01	56.03	55.43	55.96	55.89	55.90 ± 0.44	~ 53.8
431	52.07	53.82	54.73	52.10	51.23	53.38	53.65	54.11	53.14 ± 1.20	~ 53.3
Standard	Cd % (molar ratio)								Mean	Theoretical value
	49.66	49.83	49.47	49.86	50.25	50.60	51.19	49.14	50.00 ± 0.66	50.0

Table 4-3. EDX analysis results of CdS standard and the purified CdS quantum disks. a: standard deviation. Four batches of carefully purified colloidal quantum disks samples were analyzed parallel with a commercial CdS bulk powder and each sample were measured 8 times at random location. In order to further eliminate possible cadmium precursor pollution, control was carried out with pure cadmium stearate following exactly the same purification process, nothing but transparent colorless solution was observed even just after first time of three repeating purification and centrifugation processes.

thickness direction.

If only considering one excess layer of Cd ions on one of the basal planes of the disks, however, the calculated Cd/S ratio was found to be generally lower than the experimental values (Figure 4-6, right), especially for the relatively thin ones that were generally small in lateral dimensions. This discrepancy suggests that the side facets of the disks were also terminated with Cd, which ended up a higher Cd/S ratio than that calculated by only considering the basal planes. This explanation is reasonable as all facets of quantum disks should be bound by negatively-charged carboxylate ligands.

Quantum confinement of quantum disks versus quantum dots. The one dimensional quantum confinement of CdS quantum disks was confirmed by their very sharp and significantly blue-shifted UV-Vis absorption and photoluminescence (PL) peaks (Figure 4-1) in comparison to the bandgap of bulk CdS. The thickest one with its UV-Vis peak at 431 showed an interesting tail from the main peak to CdS bulk bandgap in both UV-Vis and PL spectra (Figure 4-1d), which could not be removed by all separation procedures applied. The origin of this tail is not clear at this moment. One possible reason could be the sharp

λ (hh, nm)	d (hh, nm)	λ (lh, nm)	d (lh, nm)
328	1.22	292	1.20
374	1.53	347	1.53
407	1.87	379	1.81
431	2.25	404	2.11

Table 4-4. Thickness calculation results based on corresponding heavy hole and light hole absorption. λ: exciton absorption peak position; d: thickness; hh: heavy hole; lh: light hole.

excitonic absorption and PL peaks for this specific thickness were very close to the bulk bandgap of CdS.

Except the thinnest one with its absorption peak at 328 nm, the other three thicknesses (with their UV-Vis peak at 374 nm, 407 nm, and 431 nm) showed band-edge PL peak with a significant surface-trap emission tail to the low energy side of the band-edge PL. The Full Width at Half Maximum (FWHM) of the band-edge PL peaks was small, 0.06-0.08 eV (or 9-10 nm). Though their UV-Vis and band-edge PL peaks were as sharp as those observed for CdSe quantum disks, [15] it is interesting to notice that the absorbance ratio between the main UV-Vis peak (supposedly from heavy hole-electron exciton) and the secondary peak (light hole-electron exciton) was more than ten times higher than that observed for the typical CdSe quantum disks with similar lateral dimensions. During the preparation of this chapter, we noticed that a report made a different assignment of the absorption peaks. [21] However, the calculations shown below indicate that this tentative assignment is consistent with a simple quantum confinement model proposed by the same group. [9]

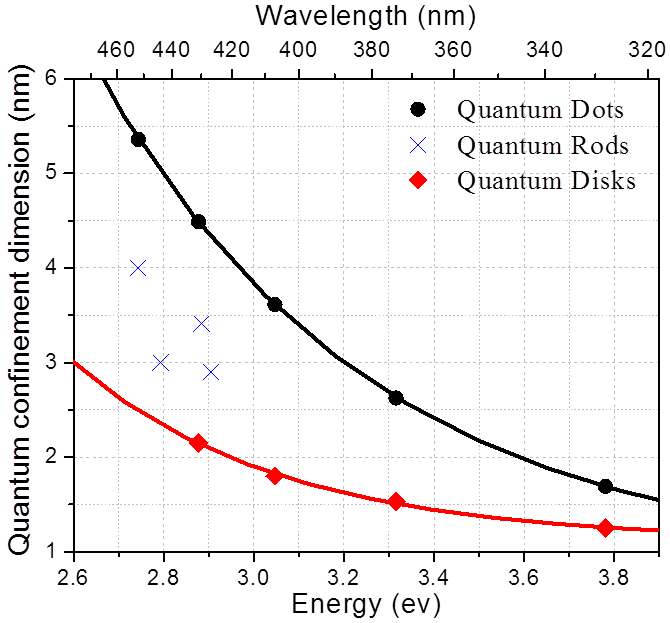

Figure 4-7. Quantum confinement dimension versus the first excitonic peak for CdS quantum dots, rods, and disks.

Thickness calculation was carried out using the equation proposed by the Dubertret group. [9] The necessary parameters were found from literature and listed as following,

CdS bandgap = 2.50 eV, [31, 32] electron effective mass = 0.205 m_0 with m_0 as the mass of free-electron, heavy hole effective mass = 5.00 m_0, and light hole effective mass = 0.54 m_0. [33] Calculations gave us the thickness values as following: 1.22 nm (UV-Vis peak at 328 nm), 1.53 nm (UV-Vis peak at 374 nm), 1.87 nm (UV-Vis peak at 407 nm), and 2.25 nm (UV-Vis peak at 431 nm), respectively. These values were reasonably close to the values determined by HRTEM (Figure 4-1). The thickness values calculated using the light hole and heavy hole absorption peaks were quite consistent (see Table 4-4).

Figure 4-7 plots the first excitonic absorption peak energy versus the thickness of the CdS quantum disks, together with CdS quantum rods [34, 35] and quantum dots. [29] For convenience, we defined "quantum confinement dimension" as the diameter of a dot, the short-axis dimension of a rod, and the thickness dimension of a disk.

Due to lack of appropriate control and data on CdS quantum rods, we were only able to get

UV peak (nm)	Thickness/ size (nm)	A_1	τ_1 (ps)	f_1	A_2	τ_2 (ps)	f_2	$\bar{\tau}$ (ps)	QY (%)	τ_n (ps)	k_r (s^{-1})	k_{nr} (s^{-1})
405_CdS dots	3.55	786	4439	0.192	566	26003	0.808	21870	13.44	162712	6.15E+06	3.96E+07
374_CdS disks	1.53	68852	49	0.986	126	391	0.014	54	0.44	12350	8.10E+07	1.84E+10
407_CdS disks	1.80	2000	47	0.616	164	358	0.384	167	0.59	28400	3.52E+07	5.97E+09
431_CdS disks	2.15	1844630	46	0.999	291	371	0.001	46	0.25	18269	5.47E+07	2.17E+10
513_CdSe disks	1.82	1234	143	0.216	1170	547	0.784	460	38.07	1208	8.28E+08	1.35E+09

Table 4-5. TRPL analysis results of CdS quantum dots together with three different thickness CdS quantum disks and one CdSe quantum disk. A_1, A_2: amplitudes of the components; τ_1, τ_2: decay times; f_1, f_2: fractional contribution; $\bar{\tau}$: average lifetime; QY: quantum yield; τ_n: natural lifetime; k_r, k_{nr}: radiative, nonradiative recombination rate.

several points from the current literature, [34, 35] which cannot generate a reasonable trendline although the data points are generally between the trendlines of quantum dots and disks. This means that, with limited data points, quantum rods exhibit medium strength of quantum confinement. Comparing to the CdS quantum dots and quantum rods, quantum disks possess much weaker quantum confinement because the exciton in a quantum disk could only be confined along the thickness direction. [36, 37]

PL decay lifetime of quantum disks versus quantum dots. Time-resolved Photoluminescence study was carried out on CdS quantum disks, which revealed a two-order of magnitude faster decay process for the CdS quantum disks in comparison to the quantum dots (Figure 4-8). The CdS quantum disks and quantum dots used for recording the data in Figure 4-8 had a similar PL emission peak position at around 418 nm. The measurements were firstly carried out using a streak camera. As shown in Figure 4-8 a, after the laser pulse, the CdS quantum disks showed a strong and sharp PL emission, then decayed to the background level completely in several hundreds picosecond. Conversely, CdS quantum dots showed continuous emission up to the scan time limit of the streak camera (Figure 4-8 b).

Figure 4-8 c plots the PL decay profile of the CdS quantum disks obtained from Figure 4-8 a. In order to accurately measure the relatively slow PL decay process of the CdS quantum dots, we also carried out measurements for the CdS quantum dots on an FLS 920 spectrometer (Figure 4-8 d) in addition to that using streak camera (Figure 4-8 b). The decay profiles of the CdS quantum disks and dots could both be fitted into double exponential decay, with average lifetime of CdS quantum disks at around 170 ps, and CdS quantum dots around 22 ns (See Table 4-5). The lifetime of CdS quantum dots agreed pretty well with results reported in literature. [38, 39]

In the multi-exponential model, the intensity is assumed to decay as the sum of individual single

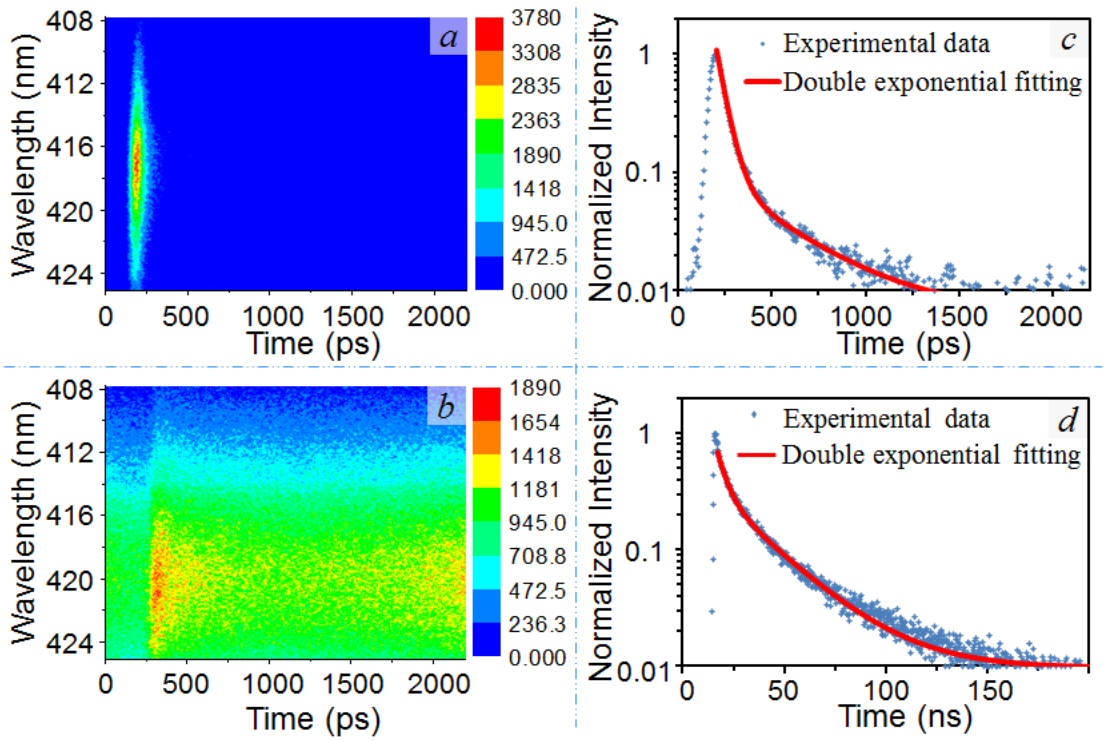

Figure 4-8. Streak camera images of fluorescence from (a) CdS quantum disks and (b) CdS quantum dots solutions. The temporal decay profile of CdS quantum disk (c) was obtained using the Streak camera data in (a). The fluorescence decay profile of CdS quantum dot (d) was measured by an FLS 920 spectrometer.

exponential decays:

$$\mathrm{I}(t) = I_0 + \sum_{i=1}^{n} A_i exp\left(-{}^{t}/_{\tau_i}\right) \tag{4-1}$$

here I_0 is the background signal, A_i are the amplitudes of the components at t = 0, τ_i are the decay times, and n is the number of decay channels.

The average lifetime $\bar{\tau}$ and the fractional contribution f_i of each decay time are given as:

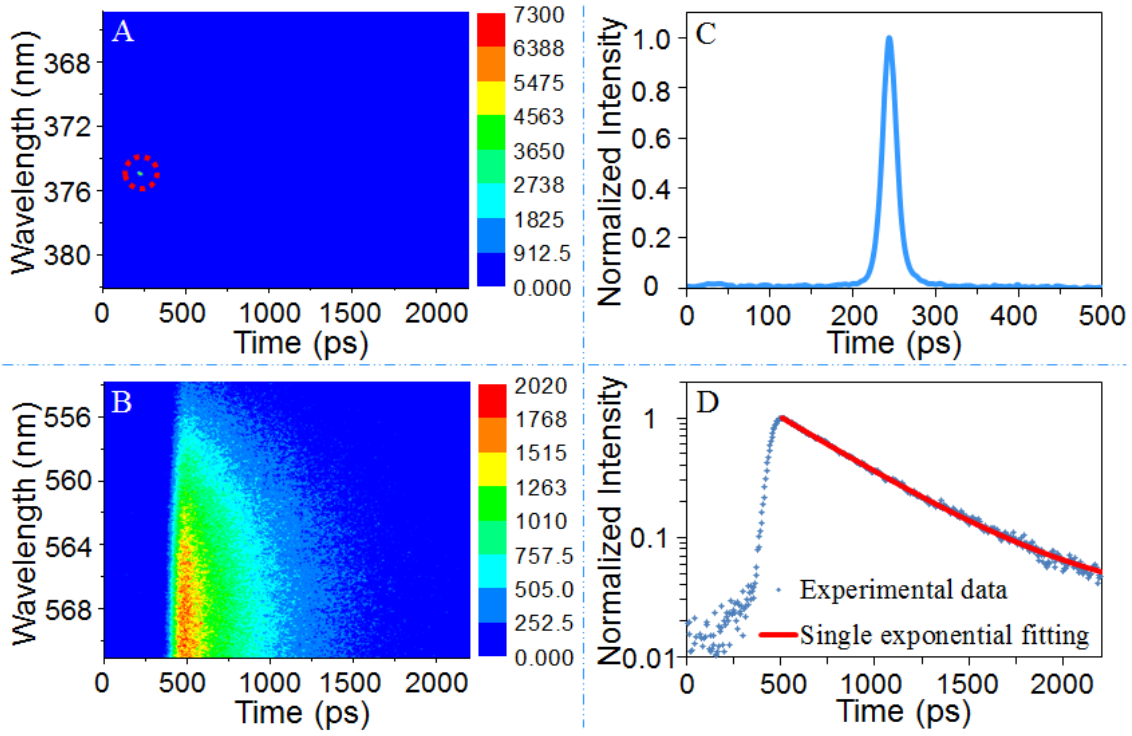

Figure 4-9. Streak camera images of (A) the 375 nm picosecond pump laser highlighted in red dashed circle and (B) fluorescence from erythrosin B in MeOH, and corresponding temporal decay profiles (C) and (D).

$$\bar{\tau} = \frac{\sum_{i=1}^{n} A_i\tau_i^2}{\sum_{i=1}^{n} A_i\tau_i} = \sum_{i=1}^{n} f_i\tau_i,\ f_i = \frac{A_i\tau_i}{\sum_{i=1}^{n} A_i\tau_i},\ \textit{and}\ \sum f_i = 1. \quad (4\text{-}2)$$

Natural lifetime, radiative/nonradiative recombination rate could be calculated based on following equations: [40, 41]

$\tau_n = \bar{\tau}/QY$ (τ_n: natural lifetime, $\bar{\tau}$: average lifetime, QY: quantum yield) (4-3a)

$k_r = 1/\tau_n$ (k_r: radiative recombination rate) (4-3b)

$k_{nr} = 1/\bar{\tau} - k_r$ (k_{nr}: nonradiative recombination rate) (4-3c)

Control was carried out on the streak camera with the same setup (Figure 4-9) and the 375 nm laser pulse width (FWHM) are on the 20 ps scale, excluding the effect of system response and

laser width on the lifetime measurements for CdS quantum disks. Besides, erythrosin B in methanol was used as the standard to test streak camera response, which gave a single-exponential decay with lifetime of 455 ps, within the error range of reported value as 470 ± 20 ps for erythrosine B. [42]

CdS quantum disks samples with their first absorption peaks at 374 and 431 nm were also measured using the same setup on streak camera (Figure 4-10), with corresponding average lifetime as 54 and 46 ps (Table S4), in the same order of magnitude as the CdS quantum disks with their first absorption peak at 407 nm mentioned above. To further confirm the much faster lifetime of quantum disks, measurements using a CdSe quantum disks with quantum yield at about 40% were carried out using the same streak camera, which yielded a lifetime as 460 ps, which is also about two orders of magnitude faster than the typical values (~ 20 ns) reported for CdSe quantum dots in literature. [43, 44]

The faster PL decay process of the CdS quantum disks compared to CdS quantum dots could possibly be explained by referencing each to the bulk CdS, respectively. At present, the relatively long PL lifetime of II-VI quantum dots (around tens of naonsecond) [38, 39] in comparison to the bulk [45] was successfully explained using the "dark exciton" states in quantum dots structure. [46-48] Although "bright exciton" could decay to the lowest energy dark exciton states in sub-picosecond time scale, the radiative recombination of optical passive dark exciton back to the ground state requires phonon-assistance. As a result, this three-particle process is generally inefficient, which in turn caused a relative long lifetime in quantum dots.

For the case of one-dimensional quantum confined nanostructures, there are possibly partial mixing between bright and dark exciton states. Accordingly, this should induce faster radiative recombination rate (See Table S4). [49, 50] Consistent with this explanation, in some cases, very

small stokes shift close to 4 meV or even zero between ensemble quantum disks UV-Vis and PL peaks was observed.

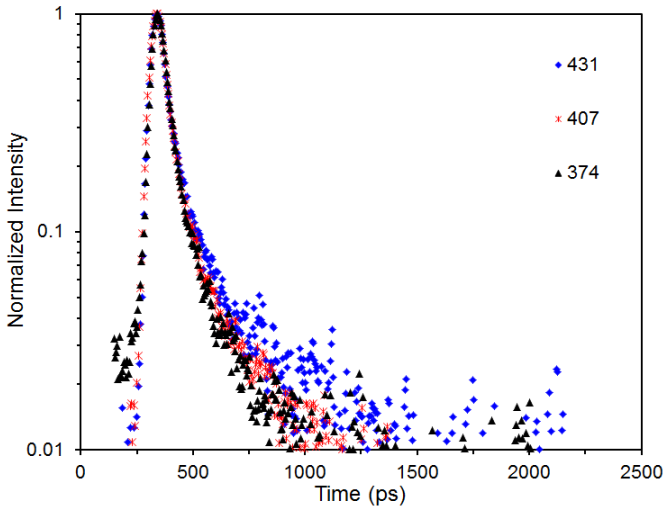

Figure 4-10. Temporal decay profiles for three different thickness CdS quantum disks. The number in the legend corresponds to the sample first absorption peak position.

Another possible explanation for the short PL lifetime of quantum disks could be formation of so-called "free exciton". [51, 52] It was reported that GaAs quantum wells grown by MBE (Molecular Beam Epitaxy) could possess PL lifetime on the picosecond scale, which was ascribed to the formation of free exciton. Interestingly, two characteristic features of free exciton, [53] namely a Lorentzian lineshape of PL and the mobility of exciton along the plane of quantum well, were both observed from independent reports on colloidal 2D nanocrystals. The Dubertret's group reported that the PL lineshape of CdSe nanoplatelets could be better fitted into Lorentzian instead of Gaussian, [10] and our results indicate similar fitting trend. The Buhro's group found out that the exciton in CdSe ultra-thin nanobelts could effectively delocalize on a μm-scale along their lateral dimensions under epifluorescence studies with position-selective excitation. [13]

The above two explanations are only tentative. This interesting phenomenon deserves further detailed spectroscopic and theoretical studies to investigate its origin. In addition to its fundamental significance, the short PL lifetime of quantum disks compared to the corresponding

quantum dots would benefit several potential applications, such as time-gated luminescence microscopy, [54, 55] flow cytometry, [56] etc., since it offers orders of magnitude smaller radiation decay time and shorter cycle time from excited state to the ground state. Coupled with its better color purity, it might also benefit applications in biological labeling for multiple targets [17, 18] and light source based on LEDs. [19, 20]

4.4 Conclusions

In summary, a series of thickness-pure colloidal CdS quantum disks covering nearly the entire quantum confinement optical window were synthesized using a simple approach with generic starting materials. Results support that formation of CdS quantum disks was most likely through "nucleation-growth" mechanism, instead of "clusters-attachment" mechanism. Thickness growth was found to be rather abrupt likely because of "two-dimensional nucleation", which probably offered a pathway for obtaining thickness-pure and atomically-flat disks. All experimental results indicate that the CdS quantum disks were grown with the polar axes (most likely <100> direction with a small chance of some disks in <111> direction) as the thickness direction. The basal planes and side facets were likely all terminated with Cd ions that were in turn passivated with the carboxylate group of the deprotonated fatty acid ligands. The disks were confirmed in zinc-blende lattice of CdS but the lattice constants were found to increase as the thickness decreased. This full series of CdS quantum disks rendered us an opportunity to compare quantum confinement between colloidal CdS quantum dots, rods, and disks. Time resolved PL decay results discovered about two-order of magnitude shorter PL lifetime for the quantum disks compared to the corresponding quantum dots, partial mixing between bright and dark exciton states and formation of free exciton were proposed as the possible explanations.

4.5 References

1. Murray, C. B.; Kagan, C. R.; Bawendi, M. G. Synthesis and characterization of monodisperse nanocrystals and close-packed nanocrystal assemblies. *Annual Review of Materials Science* **2000**, *30*, 545-610.

2. Peng, X. G. An essay on synthetic chemistry of colloidal nanocrystals. *Nano Research* **2009**, *2*, 425-447.

3. Murray, C. B.; Norris, D. J.; Bawendi, M. G. Synthesis And Characterization Of Nearly Monodisperse CdE (E = S, Se, Te) Semiconductor Nanocrystallites. *Journal of the American Chemical Society* **1993**, *115*, 8706-8715.

4. Peng, Z. A.; Peng, X. G. Formation of high-quality CdTe, CdSe, and CdS nanocrystals using CdO as precursor. *Journal of the American Chemical Society* **2001**, *123*, 183-184.

5. Peng, X. G.; Manna, L.; Yang, W. D.; Wickham, J.; Scher, E.; Kadavanich, A.; Alivisatos, A. P. Shape control of CdSe nanocrystals. *Nature* **2000**, *404*, 59-61.

6. Peng, Z. A.; Peng, X. G. Nearly monodisperse and shape-controlled CdSe nanocrystals via alternative routes: Nucleation and growth. *Journal of the American Chemical Society* **2002**, *124*, 3343-3353.

7. Tang, Z. Y.; Zhang, Z. L.; Wang, Y.; Glotzer, S. C.; Kotov, N. A. Self-assembly of CdTe nanocrystals into free-floating sheets. *Science* **2006**, *314*, 274-278.

8. Schliehe, C.; Juarez, B. H.; Pelletier, M.; Jander, S.; Greshnykh, D.; Nagel, M.; Meyer, A.; Foerster, S.; Kornowski, A.; Klinke, C.; Weller, H. Ultrathin PbS Sheets by Two-Dimensional Oriented Attachment. *Science* **2010**, *329*, 550-553.

9. Ithurria, S.; Dubertret, B. Quasi 2D Colloidal CdSe Platelets with Thicknesses Controlled at the Atomic Level. *Journal of the American Chemical Society* **2008**, *130*, 16504-+.

10. Ithurria, S.; Bousquet, G.; Dubertret, B. Continuous Transition from 3D to 1D Confinement Observed during the Formation of CdSe Nanoplatelets. *Journal of the American Chemical Society* **2011**, *133*, 3070-3077.

11. Joo, J.; Son, J. S.; Kwon, S. G.; Yu, J. H.; Hyeon, T. Low-temperature solution-phase synthesis of quantum well structured CdSe nanoribbons. *Journal of the American Chemical Society* **2006**, *128*, 5632-5633.

12. Son, J. S.; Wen, X. D.; Joo, J.; Chae, J.; Baek, S. I.; Park, K.; Kim, J. H.; An, K.; Yu, J. H.; Kwon, S. G.; Choi, S. H.; Wang, Z. W.; Kim, Y. W.; Kuk, Y.; Hoffmann, R.; Hyeon, T. Large-Scale Soft Colloidal Template Synthesis of 1.4 nm Thick CdSe Nanosheets. *Angewandte Chemie-International Edition* **2009**, *48*, 6861-6864.

13. Liu, Y. H.; Wayman, V. L.; Gibbons, P. C.; Loomis, R. A.; Buhro, W. E. Origin of High Photoluminescence Efficiencies in CdSe Quantum Belts. *Nano Letters* **2010**, *10*, 352-357.

14. Liu, Y. H.; Wang, F.; Wang, Y.; Gibbons, P. C.; Buhro, W. E. Lamellar assembly of cadmium selenide nanoclusters into quantum belts. *Journal of the American Chemical Society* **2011**, *133*, 17005-17013.

15. Xie, J.; Liu, W.; MacEwan, M. R.; Yeh, Y.-C.; Thomopoulos, S.; Xia, Y. Nanofiber Membranes with Controllable Microwells and Structural Cues and Their Use in Forming Cell Microarrays and Neuronal Networks. *Small* **2011**, *7*, 293-297.

16. Qu, L. H.; Peng, X. G. Control of photoluminescence properties of CdSe nanocrystals in growth. *Journal of the American Chemical Society* **2002**, *124*, 2049-2055.

17. Bruchez, M.; Moronne, M.; Gin, P.; Weiss, S.; Alivisatos, A. P. Semiconductor nanocrystals as fluorescent biological labels. *Science* **1998**, *281*, 2013-2016.

18. Chan, W. C. W.; Nie, S. M. Quantum dot bioconjugates for ultrasensitive nonisotopic detection. *Science* **1998**, *281*, 2016-2018.

19. Colvin, V. L.; Schlamp, M. C.; Alivisatos, A. P. Light-Emitting-Diodes Made From Cadmium Selenide Nanocrystals And A Semiconducting Polymer. *Nature* **1994**, *370*, 354-357.

20. Coe, S.; Woo, W. K.; Bawendi, M.; Bulovic, V. Electroluminescence from single monolayers of nanocrystals in molecular organic devices. *Nature* **2002**, *420*, 800-803.

21. Ithurria, S.; Tessier, M. D.; Mahler, B.; Lobo, R. P.; Dubertret, B.; Efros, A. L. Colloidal nanoplatelets with two-dimensional electronic structure. *Nature materials* **2011**, *10*, 936-941.

22. Pradhan, N.; Xu, H. F.; Peng, X. G. Colloidal CdSe quantum wires by oriented attachment. *Nano Letters* **2006**, *6*, 720-724.

23. Smit, K. J.; Ghiggino, K. P. Flash-Photolysis Studies Of A Sulfonated Bis-Styryl Biphenyl Fluorescent Dye. *Dyes and Pigments* **1990**, *13*, 45-53.

24. Fletcher, A. N.; Bliss, D. E.; Kauffman, J. M. Lasing And Fluorescent Characteristics Of 9 New, Flashlamp-Pumpable, Coumarin Dyes In Ethanol And Ethanol - Water. *Optics Communications* **1983**, *47*, 57-61.

25. Yu, W. W.; Peng, X. G. Formation of high-quality CdS and other II-VI semiconductor nanocrystals in noncoordinating solvents: Tunable reactivity of monomers. *Angewandte Chemie-International Edition* **2002**, *41*, 2368-2371.

26. Li, Z.; Ji, Y.; Xie, R.; Grisham, S. Y.; Peng, X. Correlation of CdS Nanocrystal Formation with Elemental Sulfur Activation and Its Implication in Synthetic Development. *Journal of the American Chemical Society* **2011**, *133*, 17248-17256.

27. Ouyang, J.; Zaman, M. B.; Yan, F. J.; Johnston, D.; Li, G.; Wu, X.; Leek, D.; Ratcliffe, C. I.; Ripmeester, J. A.; Yu, K. Multiple families of magic-sized CdSe nanocrystals with strong bandgap photoluminescence via noninjection one-pot syntheses. *Journal of Physical Chemistry C* **2008**, *112*, 13805-13811.

28. Li, M. J.; Ouyang, J. Y.; Ratcliffe, C. I.; Pietri, L.; Wu, X. H.; Leek, D. M.; Moudrakovski, I.; Lin, Q.; Yang, B.; Yu, K. CdS Magic-Sized Nanocrystals Exhibiting Bright Band Gap Photoemission via Thermodynamically Driven Formation. *Acs Nano* **2009**, *3*, 3832-3838.

29. Yu, W. W.; Qu, L. H.; Guo, W. Z.; Peng, X. G. Experimental determination of the extinction coefficient of CdTe, CdSe, and CdS nanocrystals. *Chemistry of Materials* **2003**, *15*, 2854-2860.

30. Mullin, J. W., *Crystallization*. Butterworth-Heinemann: Oxford [u.a.], 2004.

31. Krishna, M. V. R.; Friesner, R. A. Quantum Confinement Effects In Semiconductor Clusters. *Journal of Chemical Physics* **1991**, *95*, 8309-8322.

32. Pandey, A.; Guyot-Sionnest, P. Intraband spectroscopy and band offsets of colloidal II-VI core/shell structures. *Journal of Chemical Physics* **2007**, *127*, 104710.

33. Efros, A. L.; Rosen, M. Quantum size level structure of narrow-gap semiconductor nanocrystals: Effect of band coupling. *Physical Review B* **1998**, *58*, 7120-7135.

34. Kang, C.-C.; Lai, C.-W.; Peng, H.-C.; Shyue, J.-J.; Chou, P.-T. Surfactant- and temperature-controlled CdS nanowire formation. *Small* **2007**, *3*, 1882-1885.

35. Zhuang, Z. B.; Lu, X. T.; Peng, Q.; Li, Y. D. Direct Synthesis of Water-Soluble Ultrathin CdS Nanorods and Reversible Tuning of the Solubility by Alkalinity. *Journal of the American Chemical Society* **2010**, *132*, 1819-1821.

36. Dandrea, A.; Delsole, R. Excitons In Semiconductor Confined Systems. *Solid State Communications* **1990**, *74*, 1121-1124.

37. Yoffe, A. D. Low-Dimensional Systems - Quantum-Size Effects And Electronic-Properties Of Semiconductor Microcrystallites (Zero-Dimensional Systems) And Some Quasi-2-Dimensional Systems. *Advances in Physics* **1993**, *42*, 173-266.

38. Yu, Z. H.; Li, J. B.; O'Connor, D. B.; Wang, L. W.; Barbara, P. F. Large resonant stokes shift in CdS nanocrystals. *Journal of Physical Chemistry B* **2003**, *107*, 5670-5674.

39. Yang, B. Q.; Schneeloch, J. E.; Pan, Z. W.; Furis, M.; Achermann, M. Radiative lifetimes and orbital symmetry of electronic energy levels of CdS nanocrystals: Size dependence. *Physical Review B* **2010**, *81*, 073401.

40. Lakowicz, J. R., *Principles of fluorescence spectroscopy*. Springer: New York, 2006.

41. Parson, W. W., *Modern optical spectroscopy : with examples from biophysics and biochemistry*. Springer: Berlin; New York, 2007.

42. Boens, N.; Qin, W.; Basaric, N.; Hofkens, J.; Ameloot, M.; Pouget, J.; Lefevre, J.-P.; Valeur, B.; Gratton, E.; vandeVen, M.; Silva, N. D., Jr.; Engelborghs, Y.; Willaert, K.; Sillen, A.; Rumbles, G.; Phillips, D.; Visser, A. J. W. G.; van Hoek, A.; Lakowicz, J. R.;

Malak, H.; Gryczynski, I.; Szabo, A. G.; Krajcarski, D. T.; Tamai, N.; Miura, A. Fluorescence lifetime standards for time and frequency domain fluorescence spectroscopy. *Analytical Chemistry* **2007**, *79*, 2137-2149.

43. van Driel, A. F.; Allan, G.; Delerue, C.; Lodahl, P.; Vos, W. L.; Vanmaekelbergh, D. Frequency-dependent spontaneous emission rate from CdSe and CdTe nanocrystals: Influence of dark states. *Physical Review Letters* **2005**, *95*, 236804.

44. Donega, C. D.; Bode, M.; Meijerink, A. Size- and temperature-dependence of exciton lifetimes in CdSe quantum dots. *Physical Review B* **2006**, *74*, 085320.

45. Henry, C. H.; Nassau, K. Lifetimes Of Bound Excitons In CdS. *Physical Review B* **1970**, *1*, 1628-1634.

46. Nirmal, M.; Norris, D. J.; Kuno, M.; Bawendi, M. G.; Efros, A. L.; Rosen, M. Observation Of The Dark Exciton In CdSe Quantum Dots. *Physical Review Letters* **1995**, *75*, 3728-3731.

47. Efros, A. L.; Rosen, M.; Kuno, M.; Nirmal, M.; Norris, D. J.; Bawendi, M. Band-edge exciton in quantum dots of semiconductors with a degenerate valence band: Dark and bright exciton states. *Physical Review B* **1996**, *54*, 4843-4856.

48. Norris, D. J.; Efros, A. L.; Rosen, M.; Bawendi, M. G. Size dependence of exciton fine structure in CdSe quantum dots. *Physical Review B* **1996**, *53*, 16347-16354.

49. Fomenko, V.; Nesbitt, D. J. Solution control of radiative and nonradiative lifetimes: A novel contribution to quantum dot blinking suppression. *Nano Letters* **2008**, *8*, 287-293.

50. Hannah, D. C.; Dunn, N. J.; Ithurria, S.; Talapin, D. V.; Chen, L. X.; Pelton, M.; Schatz, G. C.; Schaller, R. D. Observation of Size-Dependent Thermalization in CdSe Nanocrystals Using Time-Resolved Photoluminescence Spectroscopy. *Physical Review Letters* **2011**, *107*, 177403.

51. Deveaud, B.; Clerot, F.; Roy, N.; Satzke, K.; Sermage, B.; Katzer, D. S. Enhanced Radiative Recombination Of Free-Excitons In Gaas Quantum-Wells. *Physical Review Letters* **1991**, *67*, 2355-2358.

52. Deveaud, B.; Clerot, F.; Roy, N.; Sermage, B.; Katzer, D. S. Enhanced Radiative Recombination Of Free-Excitons In GaAs Quantum-Wells. *Surface Science* **1992**, *263*, 491-495.

53. Deveaud, B.; Clerot, F.; Sermage, B.; Dumas, C.; Katzer, D. S. In *Optical phenomena in semiconductor structures of reduced dimensions*, Nato Advanced Research Workshop on Frontiers of Optical Phenomena in Semicondutor Structures of Reduced Dimensions, Dordrecht; Boston, 1993; Lockwood, D. J.; Pinczuk, A.; North Atlantic Treaty Organization. Scientific Affairs, D., Eds. Kluwer Academic: Dordrecht; Boston, 1993; pp 129-144.

54. Dahan, M.; Laurence, T.; Pinaud, F.; Chemla, D. S.; Alivisatos, A. P.; Sauer, M.; Weiss, S. Time-gated biological imaging by use of colloidal quantum dots. *Optics Letters* **2001**, *26*, 825-827.

55. Berezin, M. Y.; Achilefu, S. Fluorescence Lifetime Measurements and Biological Imaging. *Chemical Reviews* **2010**, *110*, 2641-2684.

56. Alivisatos, P. The use of nanocrystals in biological detection. *Nature Biotechnology* **2004**, *22*, 47-52.

Chapter 5 Conclusion

Through systematic mechanism study on the colloidal CdS quantum dots formation process in non-coordinating solvents, ODE was identified as the reducing agents for the transformation of S from elemental sulfur to CdS. Based upon the insight learned from the molecular mechanism investigation, non-injection and low temperature preparation recipes were developed for the CdS quantum dots synthesis. Colloidal CdSe quantum disks were taken as the model system to thorough characterize its structure. It turned out that the CdSe quantum disks were grown with polar axes along the thickness direction, with both basal planes composed by the Cd ions layers, which were coordinated with corresponding carboxylate ligands. The structure thermal stability was determined by the inorganic CdSe and organic carboxylate ligands interface, the longer the hydrocarbon chain, the higher the thermal stability was observed. Four different thickness colloidal CdS quantum disks covering the traditional quantum confinement region were prepared with uniform thickness. Its thickness dependent Cd/S molar ratio, lattice dilation were discovered together with shorter photoluminescence lifetime than CdS quantum dots. The quantum confinement for colloidal CdS nanocrystals was observed as the one, two, and three dimensional quantum confinement for CdS quantum disks, rods, and dots, respectively, in the order of increase of quantum confinement on the excitons.

Appendices

Reprinted (adapted) with permission from (Li, Z.; Ji, Y.; Xie, R.; Grisham, S. Y.; Peng, X. Correlation of CdS Nanocrystal Formation with Elemental Sulfur Activation and Its Implication in Synthetic Development. *Journal of the American Chemical Society* **2011**, *133*, 17248-17256.). Copyright (2011) American Chemical Society.

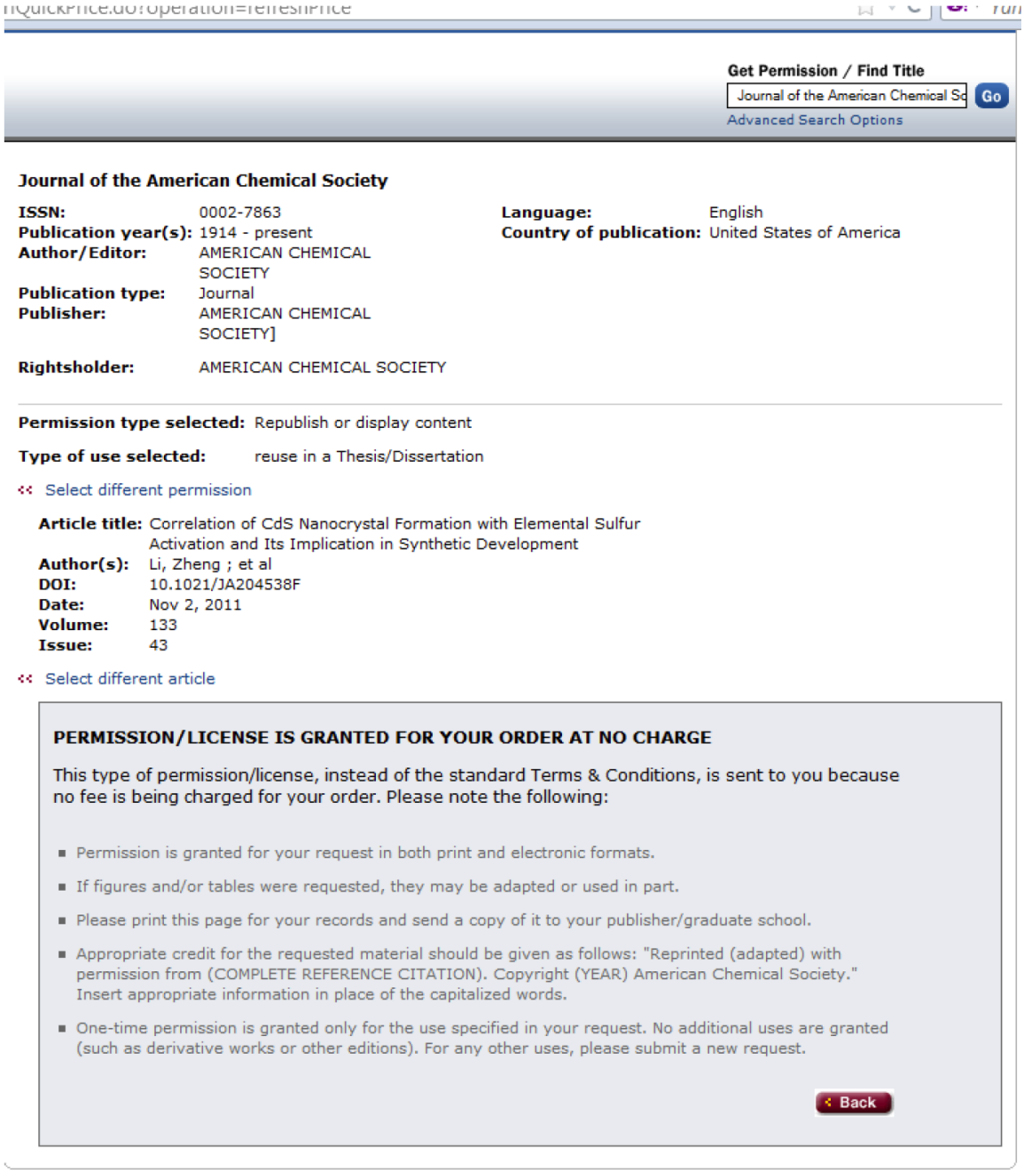

Reprinted (adapted) with permission from (Li, Z.; Peng, X. Size/Shape-Controlled Synthesis of Colloidal CdSe Quantum Disks: Ligand and Temperature Effects. *Journal of the American Chemical Society* **2011**, *133*, 6578-6586.). Copyright (2011) American Chemical Society.

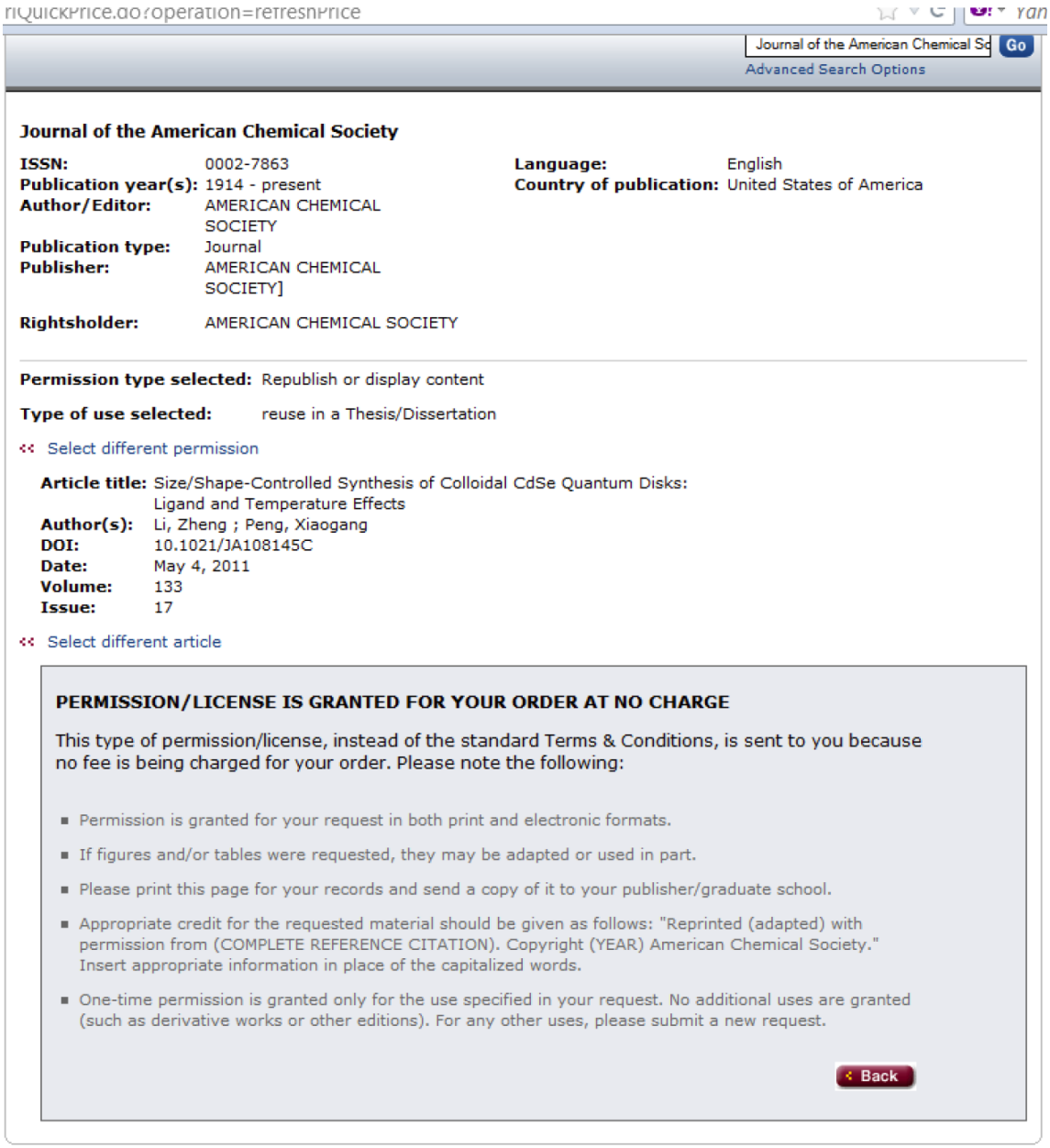

Copyright Permission Request Letter for Authors of articles in *Nano Research*

To: Copyright Permission Department

Nano Research

Tsinghua University Press

Date: 05/07/12

Copyright Permission Request

In my article tentatively entitled: Uniform Thickness and Colloidal-Stable CdS Quantum Disks with Tunable Thickness: Synthesis and Properties

that is to be submitted to the journal Nano Research

published by Tsinghua University Press & Springer, I would greatly appreciate your permission to incorporate the material set forth below with world rights in all languages, in this and any future editions, revisions, adaptations or translations, and in any other form including, without limitation, mechanical & electronic storage on any carrier:

Paper: Uniform Thickness and Colloidal-Stable CdS Quantum Disks with Tunable Thickness: Synthesis and Properties Nano Res. in press

Author(s): Zheng Li, Haiyan Qin, Dorel Guzun, Mourad Benamara, Gregory Salamo, and Xiaogang Peng

Material for which permission is requested:
Reuse the entire article for my Ph. D. dissertation

Signed: Zheng Li

Name:
Zheng Li
Department of Chemistry and Biochemistry
University of Arkansas
Fayetteville, AR 72701
USA

.....

We hereby grant permission for use of the material as specified above.

By: Yan Shuan

Title: _____